2014

ELECTRONIC AND CHEMICAL PROPERTIES OF SURFACE AND INTERFACIAL ZONES

Benjamin Thomas Young
University of Rhode Island, aegisdanneskjold@hotmail.com

ELECTRONIC AND CHEMICAL PROPERTIES OF SURFACE AND INTERFACIAL ZONES

BY

BENJAMIN THOMAS YOUNG

A DISSERTATION SUBMITTED IN PARTIAL FULFILLMENT OF THE REQUIREMENTS FOR THE DEGREE OF

DOCTOR OF PHILOSOPHY

IN

PHYSICS

UNIVERSITY OF RHODE ISLAND

2014

DOCTOR OF PHILOSOPHY DISSERTATION

OF

BENJAMIN THOMAS YOUNG

APPROVED:

Thesis Committee:

Major Professor David Heskett

M. Peter Nightingale

Godi Fischer

Nasser Zawia
DEAN OF THE GRADUATE SCHOOL

UNIVERSITY OF RHODE ISLAND
2014

ABSTRACT

Basic research is needed to further elucidate physical phenomena at surfaces as materials science applications progress to ever-shrinking length scales. Ion bombardment, or sputtering, is a ubiquitous technique used in surface preparation for both basic research and applied projects, but our understanding is incomplete concerning the nature of the process as it relates to surface modification. Investigations are presented in which electron spectroscopy and diffraction experiments and computer simulation inform a predictive model for the disorder sputtering imparts to atomically clean crystalline surfaces in pursuit of correcting this deficiency at a fundamental level. The results of Low Energy Electron Diffraction (LEED) and Inverse Photoemission Spectroscopy (IPES) studies indicate that atoms of a crystalline nickel sample have sufficient surface mobility at room temperature to self-anneal, partially healing the surface of damage inflicted by sputtering. When the sample is bombarded and held at low temperatures for analysis, the results of LEED and IPES experiments indicate the self-annealing effect is eliminated or drastically reduced.

A complex application of surface characterization with electron spectroscopy exists in the Surface Electrolyte Interphase (SEI) of lithium-ion batteries (LIBs), a protective film that grows on the electrodes of the LIB during charge/discharge cycling. Silicon is a promising anodic material for next generation LIBs because it can store more energy per unit mass than current standard materials, though steps must be taken to mitigate the effects of its large volumetric fluctuations during the cycling process, which limits performance and can destroy the battery. Investigations using

Hard X-ray Photoelectron Spectroscopy (HAXPES) into two promising tactics for accommodating the silicon volume fluctuation are presented. HAXPES experiments permit characterization of the SEI at depths unavailable to conventional techniques and reveal unique information about the chemical compositions there.

The results of HAXPES experiments performed on binder-free silicon nanoparticle anodes of batteries cycled with various electrolyte additives are presented and trends are identified to explain electrochemical cycling data which favor the electrolyte additive fluoroethylene carbonate (FEC). Anode material binders were excluded from these systems to motivate understanding of the effect each electrolyte formulation has on SEI growth and composition. The results suggest the SEI developed for FEC is thinner and of a more homogeneous nature than that of ethylene carbonate (EC). Furthermore, the FEC-derived layer is more resistant to cracking, which will be necessary to successful deployment of Si-based anodes going forward.

Anode material binders improve battery performance and lifetime by helping to maintain conductivity in the electrode as the battery is cycled. Results of HAXPES measurements on four systems which were prepared and cycled, differing only by the type of binder material used in the anode, are presented and trends identified to explain electrochemical cycling data which favor the binder polyacrylic acid (PAA).

ACKNOWLEDGMENTS

I'd like to thank my major professor, Dr. David Heskett, for his patience and for allowing me the freedom to find my own way with enough guidance to ensure I didn't get lost while I searched for it. I've learned as much about science and explaining it from watching how he tackles problems as I have from books and assignments, and I'll be forever grateful for his willingness to get in the trenches with me when I was fighting a detector or just trying to make better cornbread.

My committee, Drs. Nightingale, Fischer, McCorkle, and Lucht, have graciously provided thoughtful comments and I sincerely appreciate their mentorship.

The revolving cast of graduate students and post-docs in physics and chemistry has provided the friendship and comic relief necessary to sustain sanity throughout these past several years, and I'd like to thank Mauricio Escobar and Josh Liberty foremost among them.

Steve Pellegrino and Dave Notarianni are the yin and yang of the physics department and I doubt this document would exist without them. I don't think I've ever told Steve an idea he didn't like or Dave one he did. Together their friendship has nurtured my best ideas and saved me from my worst ones. Linda Connell keeps the whole program together and I cannot thank her enough for everything she does.

I'd also like to thank the Graduate Student Association, Graduate Assistants United, and the folks responsible for the Enhancement of Graduate Research Award program. Without their funding, most of my conference presentations and a good bit of this work wouldn't have happened.

Finally, and most importantly, my family deserves the lion's share of my gratitude. My parents, Tom and Sherry, are the kindest and most generous people I know and I don't have words to thank them for teaching me how to work hard or for their unwavering support in this endeavor. My sister, Janel, provides a constant reminder of how well I ought to have turned out with such fine parents and has been letting me win at Scrabble for some time, I think, just to keep my spirits up. Last on the list is my beautiful wife, Kat, who has yet to let me win at anything, but after four years still seems to want me around. For this I am most humbly grateful.

PREFACE

This dissertation has been prepared in manuscript format. The body comprises three papers written for submission to peer-reviewed journals as chapters and appendices in support of these papers follow.

The first chapter is an investigation of ion bombardment-induced modifications to the atomically clean Ni(110) surface prepared by noble gas ion bombardment and thermal annealing. This paper will be submitted to *Surface Science* for publication.

The second and third chapters are Hard X-Ray Photoelectron Spectroscopy (HAXPES) investigations of Solid Electrolyte Interphase (SEI) layers on lithium-ion battery (LIB) anodes.

The second chapter study compares the SEI layer that develops on silicon nanoparticle anodes in the absence of a substrate binder with various electrolyte material formulations, and contains an investigation of synchrotron radiation effects on the SEI. This paper will be submitted to the *Journal of the American Chemical Society* for publication.

The third chapter investigation also uses the HAXPES technique, but concerns the role of substrate binder material on SEI formation. For this study, SEIs on four anodes differing only in the type of binder used were characterized after similar preparation. This paper will be submitted to the *Journal of the American Chemical Society* for publication as well.

TABLE OF CONTENTS

LIST OF TABLES

LIST OF FIGURES

MANUSCRIPT-I

To be submitted to Surface Science

Ion Bombardment of Ni(110) studied with Inverse Photoemission Spectroscopy, Low Energy Electron Diffraction, and Simulations

Benjamin Young, James Warner, and David Heskett

Department of Physics, University of Rhode Island, Kingston, RI 02881, USA

Corresponding Author: Dr. David Heskett

Department of Physics

University of Rhode Island

East Hall, 2 Lippitt Rd.

Kingston, RI 02881, USA

Phone: 1-401-874-2076

Email: dheskett@uri.edu

CHAPTER 1

Ion Bombardment of Ni(110) studied with Inverse Photoemission Spectroscopy, Low Energy Electron Diffraction, and Simulations

Abstract

Inverse Photoemission Spectroscopy (IPES) performed on clean Ni(110) reveals an unoccupied electronic surface state with energy ~2 eV above the Fermi level for emission near the $\bar{Y}$ point of the Surface Brillouin Zone. Ion bombardment, or sputtering, of the sample creates vacancies which reduce the intensity of the peak in IPES spectra. Sharp, intense diffraction spots in Low Energy Electron Diffraction (LEED) patterns taken of the clean surface give way to dimmer ones after sputtering. Quantization of these patterns permits analysis of the spots' intensity profiles and changes to them after sputtering-induced disorder. Results of these measurements are compared to Monte Carlo simulations of the sputtering process to ascertain the approximate size of clean patches on the sample necessary to sustain the IPES and LEED features. At 170 K, the IPES surface state peak appears closely associated with the population of surface atomic sites contained in clean circular patches of about 50 atoms. The LEED measurements are less sensitive to surface order and appear more closely associated with smaller clean patches. Both measurements performed at 300 K indicate significant self-annealing of the sputtering damage.

1-1 Introduction

Surface electronic states on metals have been of interest since their observation by Gartland and Slagsvold [1] almost 40 years ago due to their roles in determining electronic and chemical properties of the surface and how they differ from bulk

properties [2] [3] [4] [5] [6]. Also of interest, for fundamental understanding as well as for development of technologies on controlled systems which more closely approximate real-life surfaces, investigations into defects and adsorbed species at surfaces have been studied extensively [7] [8] [9] [10] [11] [12].

In a similar vein, Morgenstern and coworkers [13] showed surface state depopulation through the disappearance of its characteristic signal in a Scanning Tunneling Microscopy (STM) /Spectroscopy (STS) study of Ag(111) for terraces less than 3.2 nm wide. Pons *et al.* [14] studied the effect of surface state confinement to monatomic step wells on the surface of Ni(111). In that work, the authors characterized differences in STM data due to the surface state expressed in triangular patches created by indenting the surface with the triangular STM tip (12.5 nm on a side). More recently, Ruggiero *et al.* [15] used STM to discover that Cu_2N islands grown on Cu(100) support two surface states for large islands. One state disappeared on islands of less than ~50 atoms and the other persisted down to islands of 12 atom size.

While the size of nanostructures clearly plays a role in the intensity of surface states, temperature is also a factor. The above studies [13-15] were conducted below 50 K. In Reflection Anisotropy Spectroscopy (RAS) investigations of clean Cu(110) under low energy noble gas ion bombardment, Martin *et al.* [16] witnessed significantly reduced intensity of the signal for the ~2 eV surface state at the $\bar{Y}$ point for increasing sample temperatures, but Bremer *et al.* [17] observed no changes in its intensity for sputtering at room temperature. Heskett *et al.* [12] reported, through Inverse Photoemission Spectroscopy (IPES) measurements, that although the same

room-temperature behavior was observed for sputtering by 1 keV Ne+, the intensity of the surface state decreased monatonically for increasing sputtering damage at 170 K. Furthermore, through simulations of the sputtering process, they predicted that the existence of a well-defined surface state signal in the IPES spectra would require unsputtered square surface patches of about 150 atoms.

Sputtering in itself is a topic of considerable importance. In addition to being the first step in many surface characterization technique preparations, sputtering can induce nanopatterning of surfaces and is a powerful tool for creating novel materials [18] [19] [20]. Additionally, low energy sputtering may be considered as an inverted layer-by-layer growth (see [17] and references therein) due to the belief that low energy sputtering damage consists mainly of point-defect vacancies. This idea motivates the present study, where we present Monte Carlo based simulations of the low-energy sputtering process to explain the results of Low Energy Electron Diffraction (LEED) and Inverse Photoemission investigations of ion-bombarded Ni(110) to further elucidate the process of sputtering at low doses and to understand how sputtering modifies electronic and structural properties of the clean surface.

1-2 Experimental

All experiments were conducted in an ultra-high vacuum chamber with a base pressure ~7 x 10^{-11} Torr. The chamber is equipped with a home-built angle-resolved inverse photoemission spectrometer and Physical Electronics' Low-Energy Electron Diffraction (LEED) and ion source apparatus.

The clean Ni(110) surface was prepared by sputtering incident at 70° relative to the sample normal with 500 eV Ar+ ions for 30 min. at an Ar pressure of 5 x 10^{-5} Torr

and an emission current of 20 mA, followed by annealing to 650 K for 5 min. The sample holder is constructed from tantalum foil which is folded around tungsten wires that are coupled to copper posts fed through a liquid nitrogen dewar. Sample heating is accomplished by passing a high current through the wires that suspend the sample holder and is monitored by a type-K thermocouple spot-welded to the sample holder.

Ion bombardment of the sample for IPES and LEED measurements was performed by back-filling the chamber with high-purity argon to various pressures in the 10^{-7} or 10^{-6} Torr range, followed by sputtering with 500 eV ions at 70° off-normal incidence and 20 mA emission current. The ion current developed across the sample during sputtering was recorded for use in the sputtering simulations.

1-2.1 LEED Measurements

LEED measurements were performed immediately following the sputtering event, initiated as soon as the sputter gas had been evacuated and the chamber pressure recovered to below 2×10^{-10} Torr. For all measurements in this study, 120 eV beam energy was used with an emission current of 1 mA, and the phosphor screen voltage was fixed at 5 keV. LEED images were acquired with a home-built CCD camera apparatus affixed to the viewport directly opposite the LEED screen.

The set of LEED images taken after each sputtering event consisted of uniformly dark and light images, in addition to that of the diffraction pattern, to correct for bad pixels in the CCD array in subsequent image analysis [21]. Analysis software written in-house was used to analyze the images and develop spot intensity profiles. Taking rough locations (within 15 pixels or so) of the diffraction spots as input from the user, the software is capable of correcting the spot center pixel values and tracking the

slight variations of the centers through the whole progression of images. Once the centers are located, the software calculates data pairs of the average intensity value of each subsequent set of nearest neighbor pixels with the radius of the nearest neighbor set. The intensity of a given spot is then computed as the midpoint Reimann sum, above the background level, of the average pixel intensity vs. radius from the center pixel.

1-2.2 IPES Measurements

Immediately following collection of the LEED images, Inverse Photoemission Spectroscopy (IPES) measurements were performed. The IPES instrument is operated in isochromat mode and comprises an electron gun of the Erdman-Zipf design [22] to provide electrons over a range of incident energies and a Geiger-Müller Tube to detect photons emitted from the crystal. The detector is filled with helium to 18 Torr (uncorrected pressure read by an N_2-calibrated Convectron gauge), before opening a valve to iodine crystals which are allowed to equilibrate. The iodine crystal reservoir is evacuated and then frozen by liquid nitrogen under rough vacuum to purge the volume of atmosphere when the iodine has eventually all sublimated and needs refilling. The entrance window of the detector is a 2.5 mm-thick SrF_2 disc with a diameter of 1". This arrangement permits detection of photons with 9.5 eV with a bandpass of approximately 0.5 eV as the difference between the photoionization threshold of iodine and the energy cutoff for transmission through the end window [23].

The detector signal is conditioned by a fast-pulse counting circuit, delay line amplifier, and single channel analyzer before being recorded as count rate vs. the

energy of electrons incident on the sample from the electron gun. For all spectra taken in this study, the end window of the detector was positioned by a linear manipulator to within 2 cm of the sample surface at 45° relative to the sample normal. The electron gun was aimed 45° off the sample normal direction. The electron energies are scanned in steps of 100 meV and held for 250 ms before proceeding to the next energy step. The spectra collected for this study are sums of 50 scans, normalized to the average current developed across the sample at each energy step.

Spectra of the clean sample showed no obvious changes in feature intensities or locations over a period of a few hours when taken back to back.

1-2.3 Simulations

A model of the sputtering process was developed by approximating a clean 1000x1000 atom surface as a null-array of dimension 1000 and using Monte Carlo methods to simulate sputtering damage. We obtained an analytic expression for the ion flux from fits to the sample current data collected during sputtering, an estimation of the ratio of nickel sample area to the total current collection area (sample, holder, posts) by image analysis, and the area of the surface unit cell. From this we obtained an average number of collisions per surface atom during an event by integrating over the time range of the event. We assumed each collision with the surface removed, on average, one atom due to the relatively low energy and off-normal incidence used here. This is supported by the conclusions of Vasylyev and coworkers in their study of Ar ion bombardment on low index nickel surfaces [24], where it was suggested that low-dose sputtering on this system likely produces vacancy point defects. We note, however, that other authors have reported various higher estimates for the yield [25]

[26] [27] [28].

For each collision in the simulation, 0-2 atoms were removed from the simulated crystal with equal probability. If 1 atom was chosen, only the primary atom was removed. If two atoms were removed, an adjacent atom to the primary location was also removed with probability based on the geometry of the Ni(110) surface unit cell, which is rectangular with dimensions a x a / $\sqrt{2}$, where a is the lattice parameter and $a_{Ni} = 3.52\text{Å}$ [29]. One was then added to elements in the array representing the atoms selected for sputtering. The simulated crystal was then analyzed to determine the number of atomic sites in the crystal contained in clean patches (array element values still zero) of radius r, where r was varied. The analysis was run over each subsequent sputtering increment to develop curves corresponding to each value of r to define $f(\theta)^r$, the relative population of surface atoms in patches of clean atomic radius r, as a function of θ (equivalent monolayers removed). We calculated comparable θ values for the IPES and LEED results using the development here to motivate later comparison.

1-3 Results

1-3.1 LEED Measurements

Images taken of characteristic LEED diffraction patterns during a progression of sputtering at {0 (clean), 1, 3, 5, 9, 11, 15} minutes of cumulative bombardment by 500 eV Ar^+ ions at 170K are displayed in Figure 1-1 to Figure 1-7. All spots were analyzed according to the procedure described in Section 1-2, though the results for the (0,1) spot have been discarded due to interference from the wires/posts of the sample holder. In general, unless the analysis algorithm encounters the sample holder

or edge of the LEED screen while profiling a spot out to a radius of 30 pixels from the spot center, it will be included in the analysis and its intensity at each sputtering increment averaged with other symmetric spots ((±1, ±1) for example) to correct for errors in sample alignment. The spot intensity profile for the (1,-1) spot (highlighted in Figure 1-1) is displayed in Figure 1-8 as the averaged pixel intensity relative to the radius, in pixels, away from the spot center. Individual traces correspond to the intensity profile of that spot after each increment of sputtering. Total intensity of each spot at each sputtering increment was then calculated and normalized to the clean spot intensity for comparison to IPES and Monte Carlo results in Figure 1-12.

1-3.2 IPES Measurements

Characteristic spectra from the IPES measurements are displayed in Figure 1-9. Data collected for the experiment performed when the sample was cooled with liquid nitrogen are shown in (a) and for room temperature in (b). The count rate is plotted on the y-axis as intensity and the scale of the electron kinetic energy on the x-axis has been shifted to align 0 eV with the half-rise location of the Fermi edge energy, E_F. The traces correspond to IPES spectra taken after the cleaning procedure and then after each subsequent sputtering event, and are offset vertically for display purposes. The intensity of the surface state feature decreases monatonically with cumulative sputtering damage and appears to (nearly) reach a steady state by 0.4 ML removal of the surface (calculated in the procedure of Section 1-2.3). The total intensity of the surface state feature was calculated, relative to a linear background for each spectrum defined by the intensity values at the same energy locations on either side of the surface state peak on each spectrum. We observed no broadening of the surface state

peak under ion bombardment, which we also noted to be the case within the resolution limit of our analyzer in an earlier study on sputtering of Cu(110) [12]. The intensity values were then normalized relative to the clean spectrum peak intensity for display with the other results in Figure 1-12.

1-3.3 Simulations

Selected results of the sputtering model on small areas of the larger simulated crystal are shown in Figure 1-10. The sections shown are 150 sites wide by 50 sites high. The sites where sputtering has removed a surface atom are shown as greyscale disturbances on the otherwise white background representing areas untouched by the bombardment process. Black represents the site(s) in each simulated crystal where the largest number of atoms has been removed from a single site (usually 2 or less). Because the second layer atoms of a face-centered cubic (110) surface are not directly beneath those of the first layer, the analysis considers only the top layer. Curves corresponding to $f(\theta)^r$, the relative population of surface atoms in clean patches of atomic radius r, as a function of θ (equivalent monolayer removed) are displayed in Figure 1-11. One dashed trace is displayed per value of *r*, and integer *r* values are highlighted with slightly thicker, solid lines for clarity. For all values of *r* the intensity function $f(\theta)^r$ decreases with apparent exponential behavior in θ and the decrease is faster for successively higher values of *r*.

1-4 Discussion

A summary of the results from techniques applied in this study is displayed in Figure 1-12 for the experiment conducted at 170 K. The IPES surface state peak intensity appears to decrease along with the prevalence of untouched circular patches

of radius 4 atoms. From this we estimate that the minimum circular patch size necessary to sustain the surface state in these measurements is approximately 50 atoms. This agrees very well with the work of Ruggiero *et al*., who reported that a surface state observed for nanoscale Cu_2N islands on Cu(100) disappears on islands with fewer than ~50 atoms [15]. Investigations of surface states on terraces and in confinement regions have produced comparable or higher estimates for necessary areas [14] [30] [31]. It should be noted that these experiments were conducted at temperatures much lower than we are able to achieve in our current setup.

In our previous study [12], we found no obvious change in the intensity of the IPES surface state peak observed on Cu(110) for sputtering at room temperature, but performed at 170 K, the sputtering process did reduce its intensity to near zero. For the present work, we were able to decrease the intensity of the Ni(110) surface state by room temperature sputtering, as displayed in Figure 1-9b, indicating the thermal self-annealing at room temperature is less effective for Ni(110) than was true for Cu(110). Analysis of the intensity decrease relative to the amount of sputtering damage using the yield estimates described above indicate that the surface state feature in the IPES spectra requires approximately 10 times the sputtering dose to achieve comparable results as when the experiment is performed at 170 K, and the estimated radius of the clean patch size necessary to sustain the surface state peak is about 2 atoms smaller at room temperature. As the model does not account for the self-annealing effect, we expect it to underestimate the necessary patch size for experiments performed at temperatures where self-annealing occurs faster than data collection can be accomplished. This is obviously true for the room temperature measurement, though

it is unclear whether 170 K is a sufficiently low temperature to eliminate the effect. Thus, we believe the estimate that the IPES surface state feature requires clean patches of ~50 atoms to represent a lower bound on the true minimum patch size.

Analysis of the spot intensity profiles from the LEED measurements follows a similar trend as the IPES results. The LEED intensities behave similarly to the simulated curves for patches of atomic radius 2-3 at 170 K and similar to those of radius 1-1.5 at 300 K, though comparison with the simulated results yields less trustworthy quantitative information for LEED than for IPES. Because the LEED measurement takes information from deeper than IPES [32], and because the simulation concerns only the top layer of the surface, it is not surprising that the LEED spots' intensity reduction is tied to clean patches of smaller size than the IPES surface state and appears to more quickly approach an asymptotic intensity level (~40% relative to clean) as displayed in Figure 1-12.

1-5 Conclusions

Argon ion bombardment of Ni(110) has been investigated at room temperature and at 170 K by IPES, LEED, and computer simulations. Bombardment-associated effects on the intensity of the unoccupied surface electronic state near the $\bar{Y}$ point of the Surface Brillouin Zone in IPES spectra, as well as on the intensity profiles of diffraction spots in LEED patterns have been discussed. Monatonic reduction of the intensities of the features in both IPES and LEED results are compared to the simulations of sputtering to determine 50 atoms as a lower bound estimate on the size of clean surface patches necessary to sustain the surface state in IPES spectra. Both the LEED and IPES measurements exhibit thermal self-annealing effects at room

temperature which are reduced at 170 K.

1-6 Acknowledgements

We would like to thank the University of Rhode Island Graduate School and administrators of the EGRA program for partial support of this research.

1-7 References

[1] P. Gartland and B. Slagsvold, "Transitions conserving parallel momentum in photoemission from the (111) face of copper," *Physical Review B,* vol. 21, p. 4047, 1975.

[2] A. Goldmann, V. Dose and G. Borstel, "Empty electronic states at the (100), (110), and (111) surfaces of nickel, copper, and silver," *Physical Review B,* vol. 32, no. 4, pp. 1971-1980, 1985.

[3] A. Goldmann, M. Donath, W. Altmann and V. Dose, "Momentum-resolved inverse photoemission study of nickel surfaces," *Physical Review B,* vol. 32, no. 2, pp. 837-850, 1985.

[4] O. Zeybek, A. Davarpanah and S. Barrett, "Electronic surface states of Cu(110) surface," *Surface Science,* vol. 600, pp. 5176-5181, 2006.

[5] N. Biswas, J. Gurganus and V. Misra, "Work function tuning of nickel silicide by co-sputtering nickel and silicon," *Applied Physics Letters,* vol. 87, p. 171908, 2005.

[6] J. Li, W. Schneider, R. Berndt, O. Bryant and S. Crampin, "Surface-State Lifetime Measured by Scanning Tunneling Microscopy," *Physical Review Letters,* vol. 81, no. 20, pp. 4464-4467, 1998.

[7] T. Allmers, M. Donath, J. Braun, J. Minar and H. Ebert, "d- and sp- like surface states on fcc Co(001) with distinct sensitivity to surface roughness," *Physical Review B,* vol. 84, p. 245426, 2011.

[8] E. Boschung, T. Pillo, J. Hayoz, L. Patthey, P. Aebi and L. Schlapbach, "Hydrogen-induced changes in the surface states/resonances of Ni(100)," *Journal of Electron Spectroscopy and Related Phenomena,* Vols. 101-103, pp. 349-353, 1999.

[9] S. Yu, B. Bahrim, B. Makarenko and J. Rabalais, "Local effect of Na adsorption on Cu(111)," *Surface Science,* vol. 606, pp. 1700-1704, 2012.

[10] D. Tang and D. Heskett, "Unoccupied electronic structure of Na/Ni(111)," *Physical Review B,* vol. 47, no. 16, pp. 695-699, 1993.

[11] C. Su, D. Tang and D. Heskett, "Two-dimensional unoccupied electronic band structure of clean Cu(110) and (1x2) Na/Cu(110)," *Surface Science,* vol. 310, pp. 45-51, 1994.

[12] D. Heskett, D. DePietro, G. Sabatino and M. Tammaro, "Ion bombardment-induced changes in the electronic structure of Cu(110) investigated with inverse photoemission and computer simulations," *Surface Science,* vol. 513, pp. 405-411, 2002.

[13] K. Morgenstern, K. Braun and K. Rieder, "Surface-State Depopulation on Small Ag(111) Terraces," *Physical Review Letters,* vol. 89, no. 22, p. 226801, 2002.

[14] A. Bendounan, H. Cercellier, Y. Fagot-Revurat, B. Kierren, V. Yurov and D. Malterre, "Confinement of Shockley states in ultra thin films of Ag on Cu(111)," *Thin Solid Films,* vol. 428, no. 1-2, pp. 119-122, 2003.

[15] O. Rodríguez de la Fuente, M. González-Barrio, V. Navarro, B. Pabón, I. Palacio and A. Mascareque, "Surface defects and their influence on surface properties," *Journal of Physics: Condensed Matter,* vol. 25, no. 48, p. 484008, 2013.

[16] W. Chan and E. Chason, "Making waves: Kinetic processes controlling surface evolution during low energy ion sputtering," *AIP: Journal of Applied Physics,* vol. 101, p. 121301, 2007.

[17] X. Ou, R. Kögler, X. Wei, A. Mücklich, X. Wang, W. Skorupa and S. Facsko, "Fabrication of horizontal silicon nanowire arrays on insulator by ion irradiation," *AIP Advances,* vol. 1, p. 042174, 2011.

[18] A. Biermanns, A. Hanisch, J. Grenzer, T. Metzger and U. Pietsch, "Tuning the shape and damage in ion-beam induced ripples on silicon," *Physica Status Solidi (a),* vol. 208, no. 11, pp. 2608-2611, 2011.

[19] R. Roucka, J. Jiruse and T. Sikola, "Spot intensity processing in LEED images," *Vacuum,* vol. 65, pp. 121-126, 2002.

[20] P. Erdman and E. Zipf, "Low Voltage, High Current Electron Gun," *Review of*

Scientific Instruments, vol. 53, pp. 225-227, 1982.

[21] M. Budke, V. Renken, H. Liebl, G. Rangelov and M. Donath, "Inverse photoemission with energy resolution better than 200 meV," *Review of Scientific Instruments,* vol. 78, p. 083903, 2007.

[22] M. Vasylyev, A. Blaschuk, N. Mashovets and N. Vilkova, "LEED study of Ni(100) and (111) surface damage caused by Ar+ ion bombardment with low energy and small doses," *Vacuum,* vol. 57, pp. 71-80, 2000.

[23] P. Lane, G. Isted and R. Cole, "Effect of surface defects and adsorbates on the optical anisotropy of Cu(110)," *Physical Review B,* vol. 82, p. 075416, 2010.

[24] T. Michely and G. Comsa, "Temperature dependence of the sputtering morphology of Pt(111)," *Surface Science,* vol. 256, no. 3, pp. 217-226, 1991.

[25] T. Michely and G. Comsa, "The scanning tunneling microscope as a means for the investigation of ion bombardment effects on metal surfaces," *Nuclear Instruments and Methods in Physics Research Section B: Beam Interactions with Materials and Atoms,* vol. 82, no. 2, pp. 207-219, 1993.

[26] Q. Wei, K. Li, J. Lian and L. Wang, "Angular dependence of sputtering yield of amorphous and polycrystalline materials," *Journal of Physics D: Applied Physics,* vol. 41, p. 172002, 2008.

[27] N. Ashcroft and N. Mermin, Solid State Physics, Philadelphia: W.B. Saunders College, 1976.

[28] C. Ruggiero, M. Badal, T. Choi, D. Gohlke, D. Stroud and J. Gupta, "Emergence of surface states in nanoscale Cu_2N islands," *Physical Review B,* vol. 83, p. 245430, 2011.

[29] S. Pons, P. Mallet, L. Magaud and J. Veuillen, "Investigation of the Ni(111) Shockley-like surface state using confinement to artificial nanostructures," *Europhysics Letters,* vol. 61, no. 3, pp. 375-381, 2003.

[30] J. Bellina and H. Farnsworth, "Ion Bombardment Induced Surface Damage in Tungsten and Molybdenum Single Crystals," *Journal of Vacuum Science and Technology,* vol. 9, no. 2, pp. 616-619, 1972.

Figures

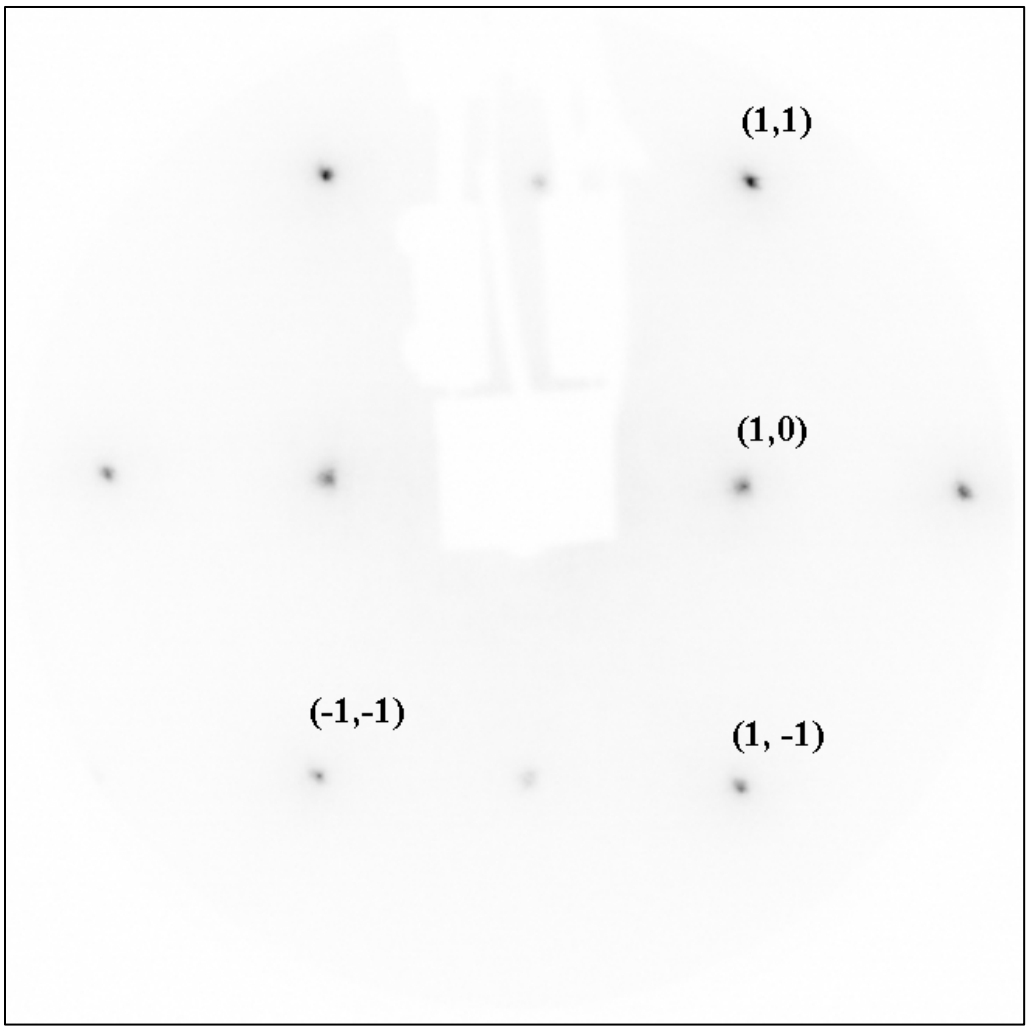

Figure 1-1: LEED pattern observed for Ni(110) after 0 min. of sputtering by 500 eV Ar^+ at $p=2x10^{-7}$ Torr. The sample temperature was held at ~170 K throughout. Labels indicate the dot indexing convention.

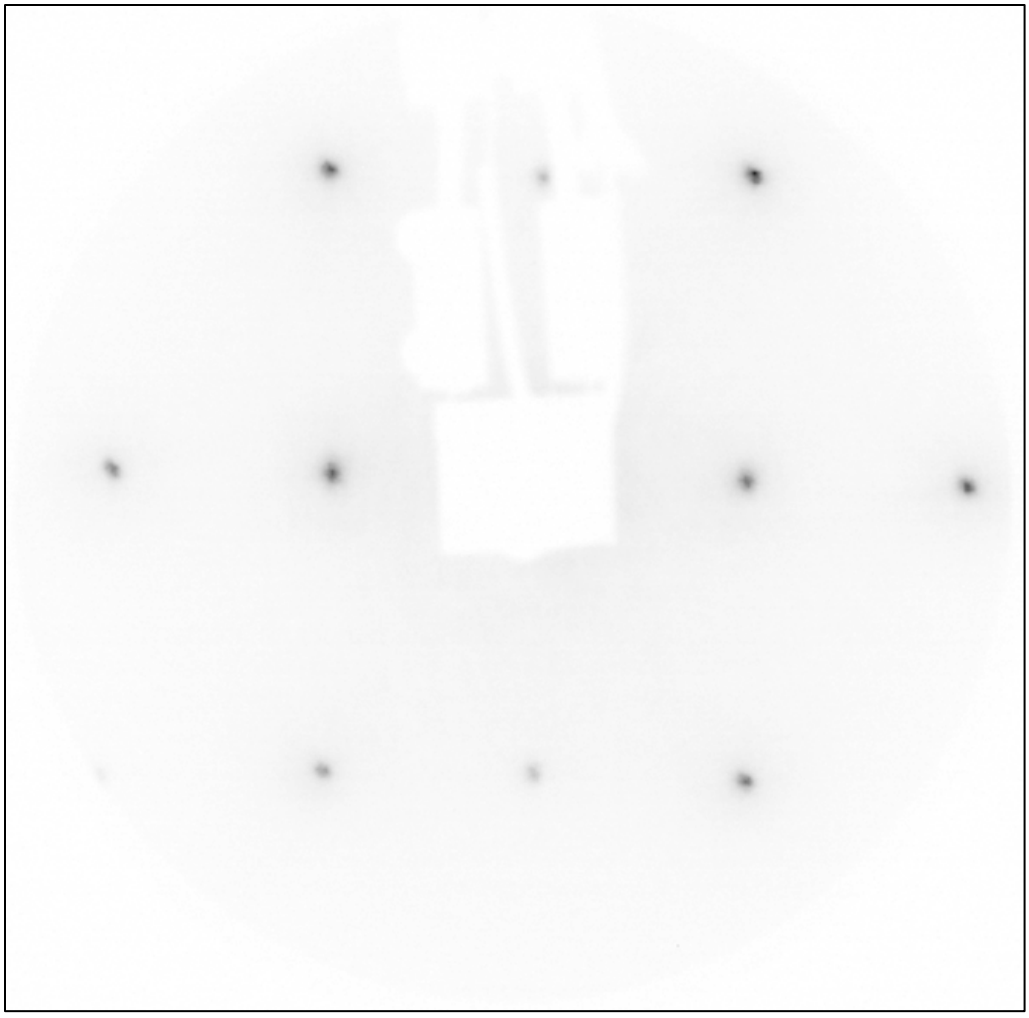

Figure 1-2: LEED pattern observed for Ni(110) after 1 min. of sputtering by500 eV Ar^+ at $p=2x10^{-7}$ Torr. The sample temperature was held at ~170 K throughout.

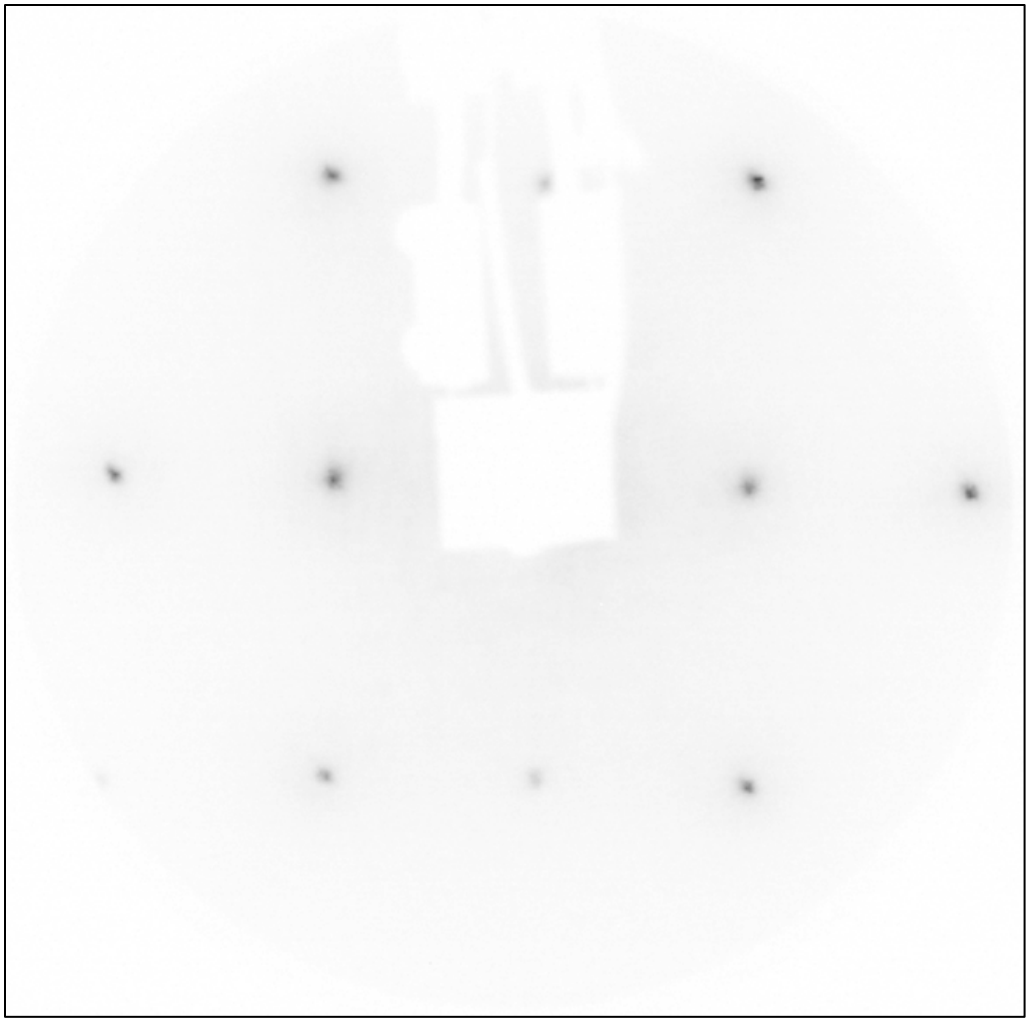

Figure 1-3: LEED pattern observed for Ni(110) after 3 min. of sputtering by 500 eV Ar^+ at $p=2x10^{-7}$ Torr. The sample temperature was held at ~170 K throughout.

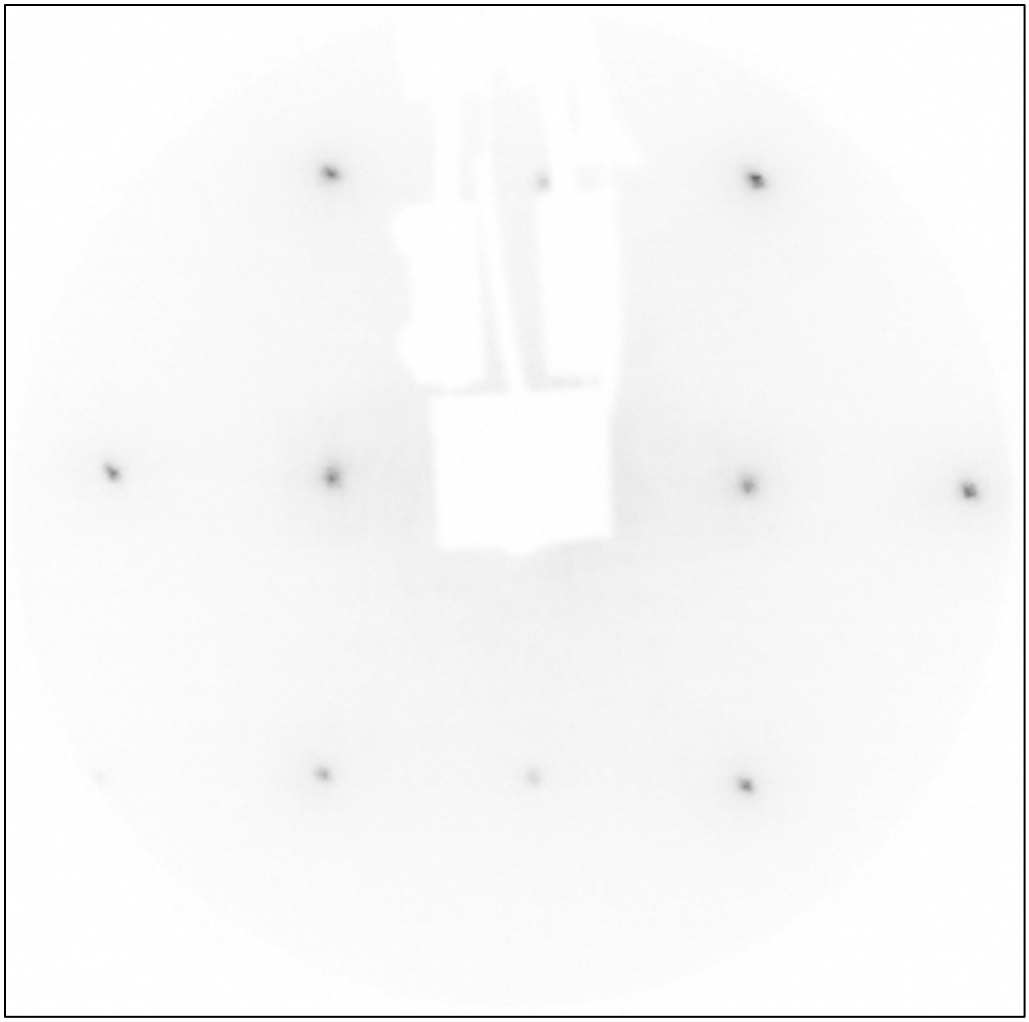

Figure 1-4: LEED pattern observed for Ni(110) after 5 min. of sputtering by 500 eV Ar^+ at p=2x10^{-7} Torr. The sample temperature was held at ~170 K throughout.

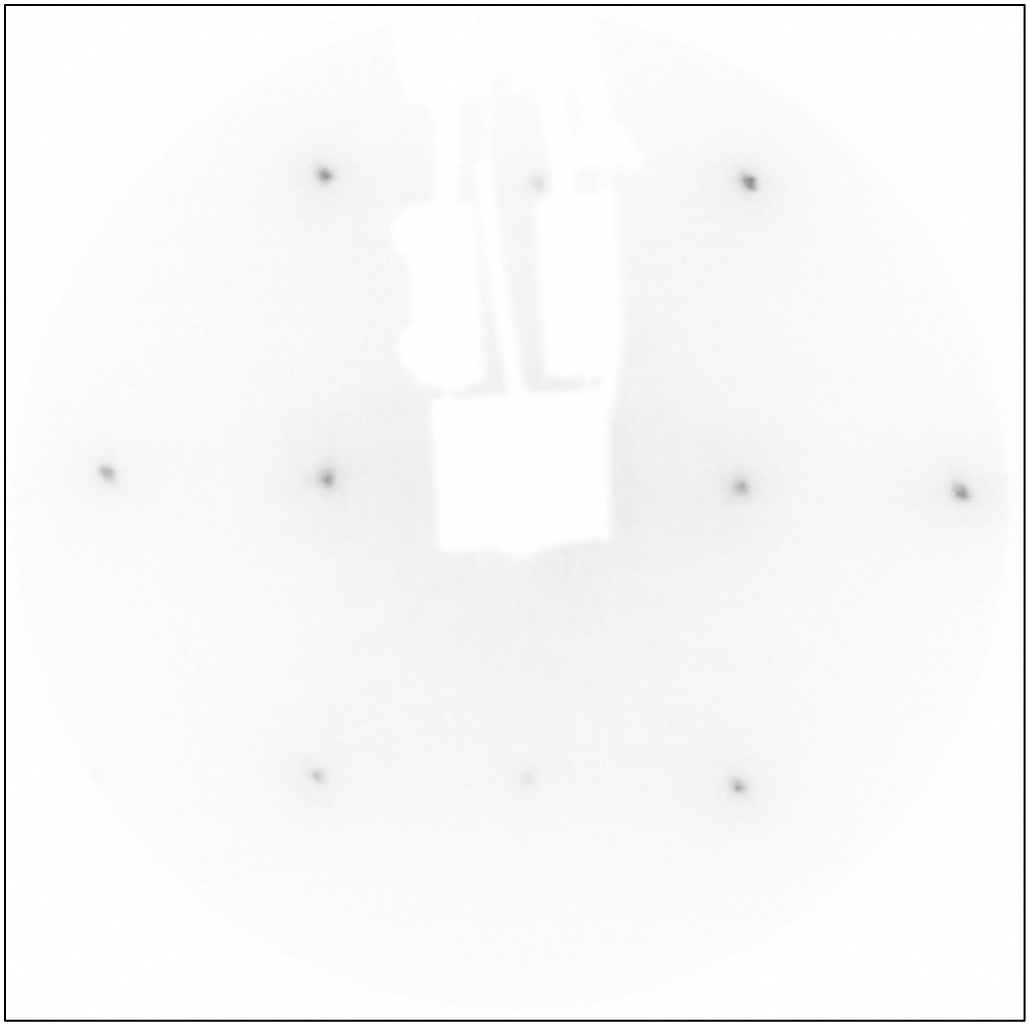

Figure 1-5: LEED pattern observed for Ni(110) after 9 min. of sputtering by 500 eV Ar^+ at $p=2x10^{-7}$ Torr. The sample temperature was held at ~170 K throughout.

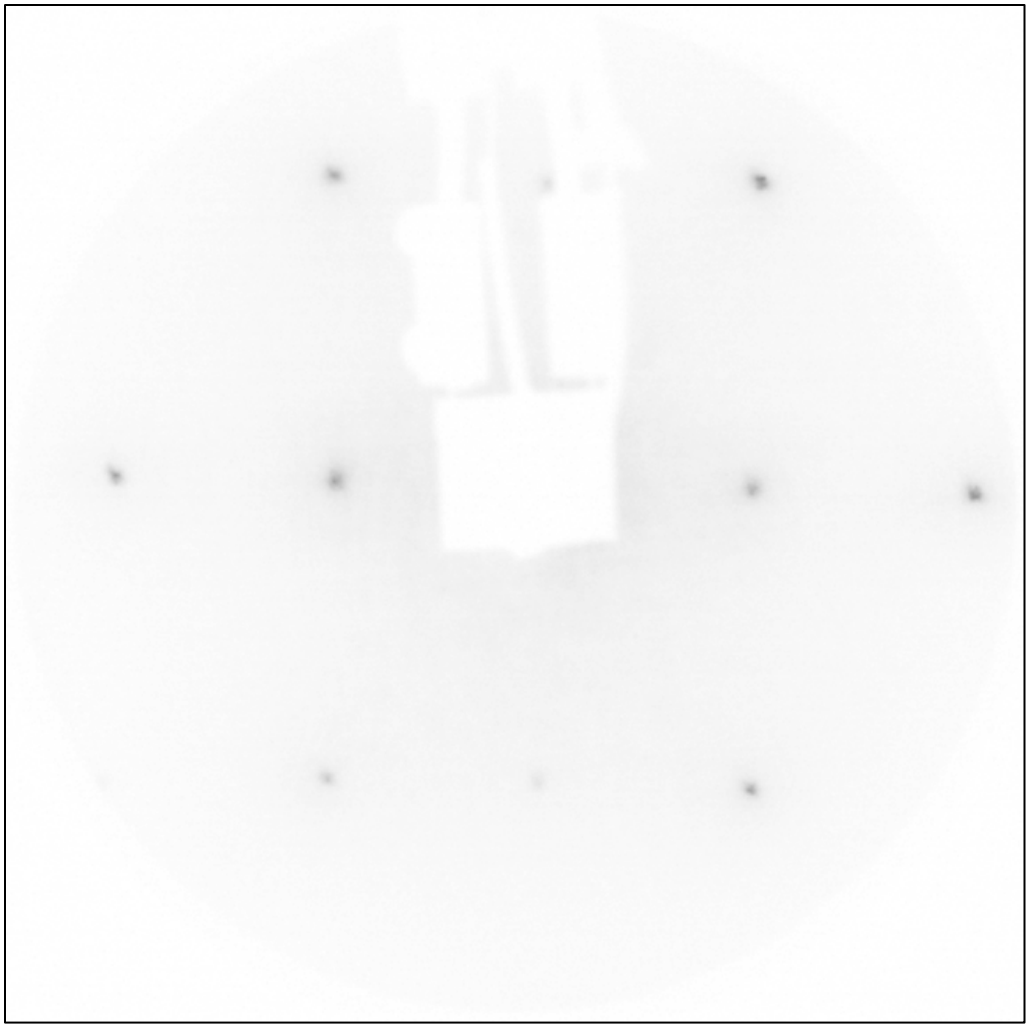

Figure 1-6: LEED pattern observed for Ni(110) after 11 min. of sputtering by 500 eV Ar^+ at $p=2x10^{-7}$ Torr. The sample temperature was held at ~170 K throughout.

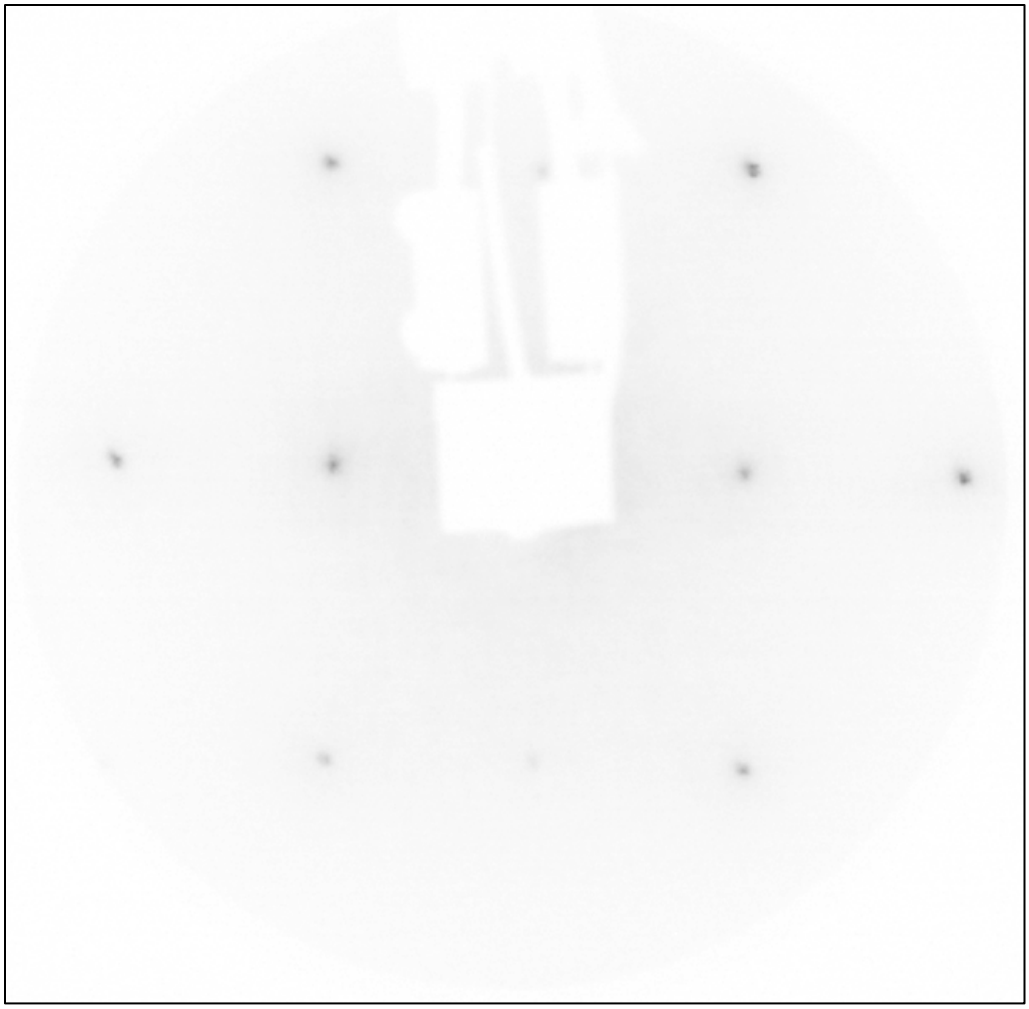

Figure 1-7: LEED pattern observed for Ni(110) after 15 min. of sputtering by 500 eV Ar^+ at p=2x10^{-7} Torr. The sample temperature was held at ~170 K throughout.

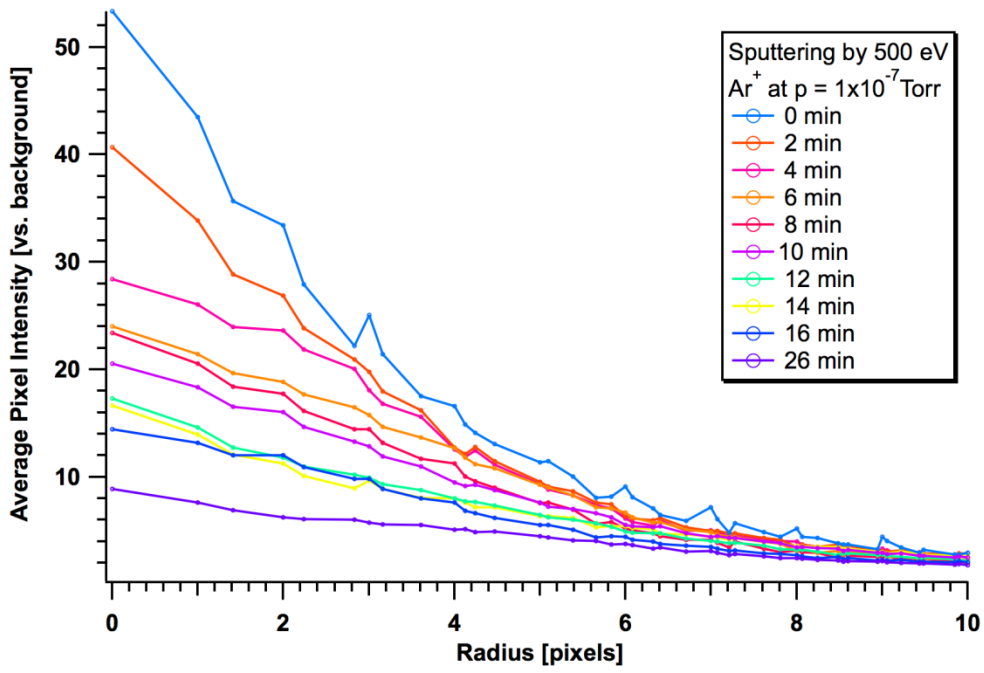

Figure 1-8: Spot intensity profiles for the (1,-1) LEED spot for the clean (light blue, top) sample through cumulative sputtering of 15 minutes by 500 eV Ar^+ at $p=1x10^{-7}$ Torr.

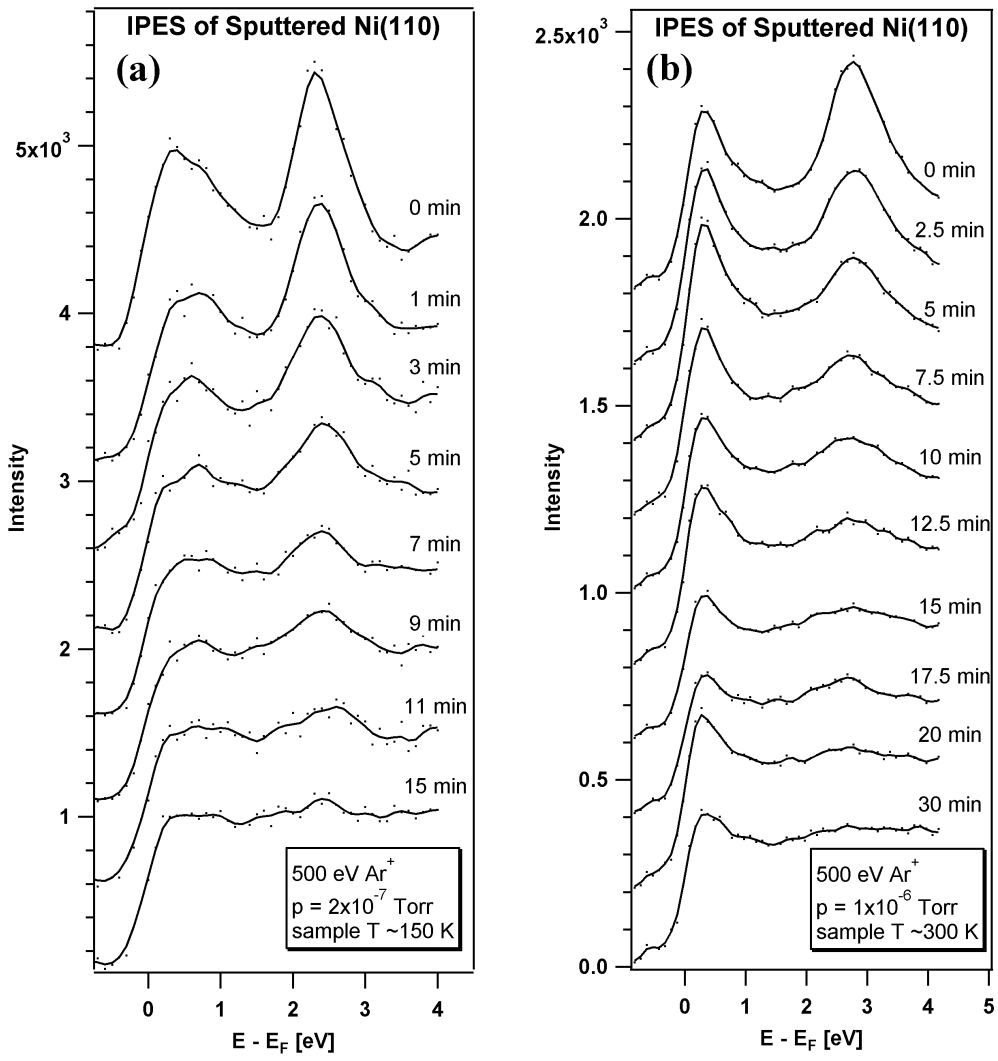

Figure 1-9: Inverse Photoemission spectra of the Ni(110) surface sputtered by 500 eV in an Ar atmosphere for various sputtering times at 70° degree incidence from the sample normal. The sample was held at ~170 K for sputtering and measurement, and the spectra were recorded for a geometry corresponding to emission from the $\bar{Y}$ point. The sample was held at (a) T~170 K and sputtering performed at $p=2x10^{-7}$ or (b) T~300 K and sputtering performed at , $p=1x10^{-6}$ Torr.

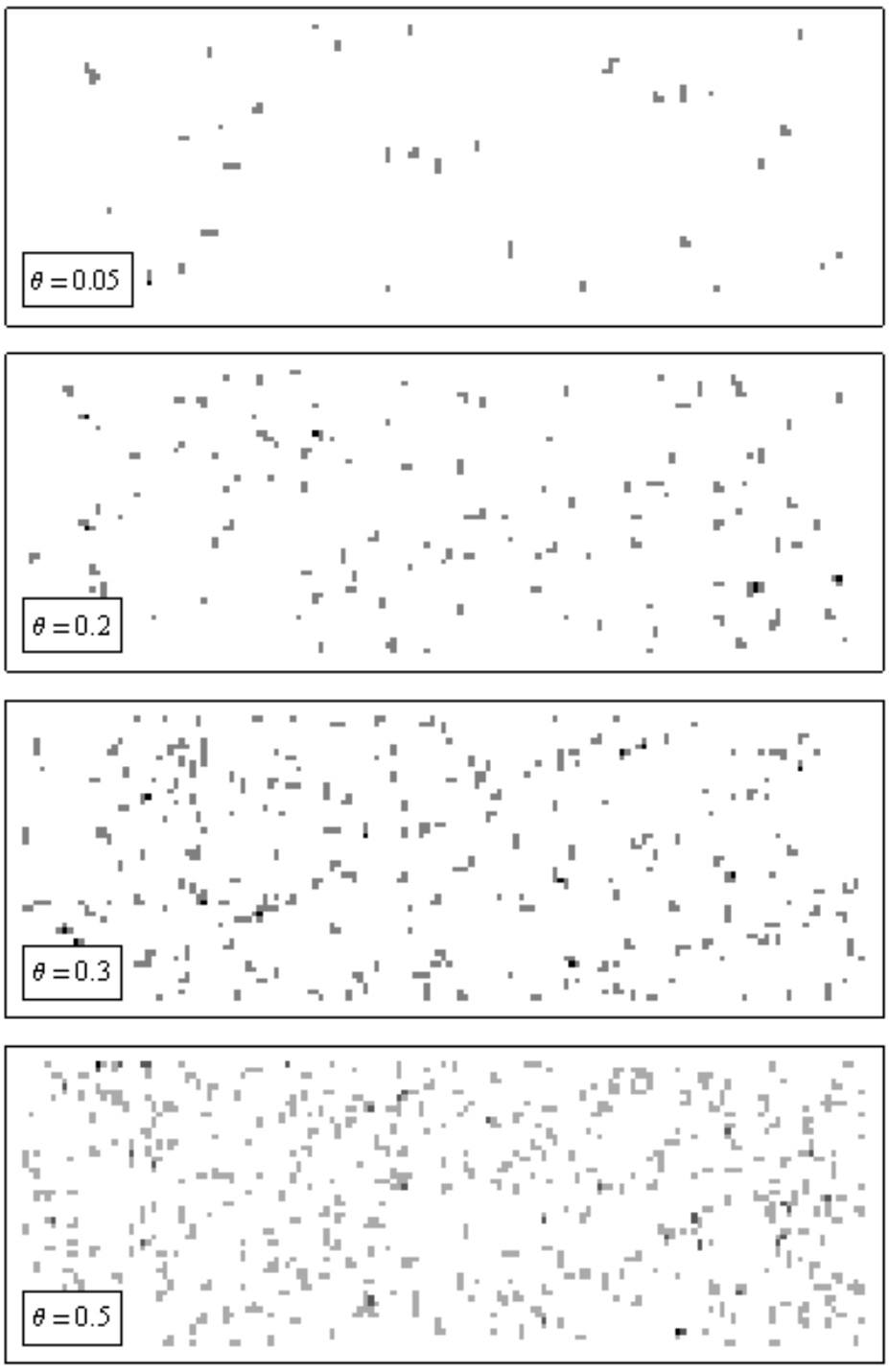

Figure 1-10: Simulated sputtered crystal representations for θ= {0.05, 0.2, 0.3, 0.4} ML removed. White areas represent patches of unsputtered atoms and sites where atoms have been removed are darker.

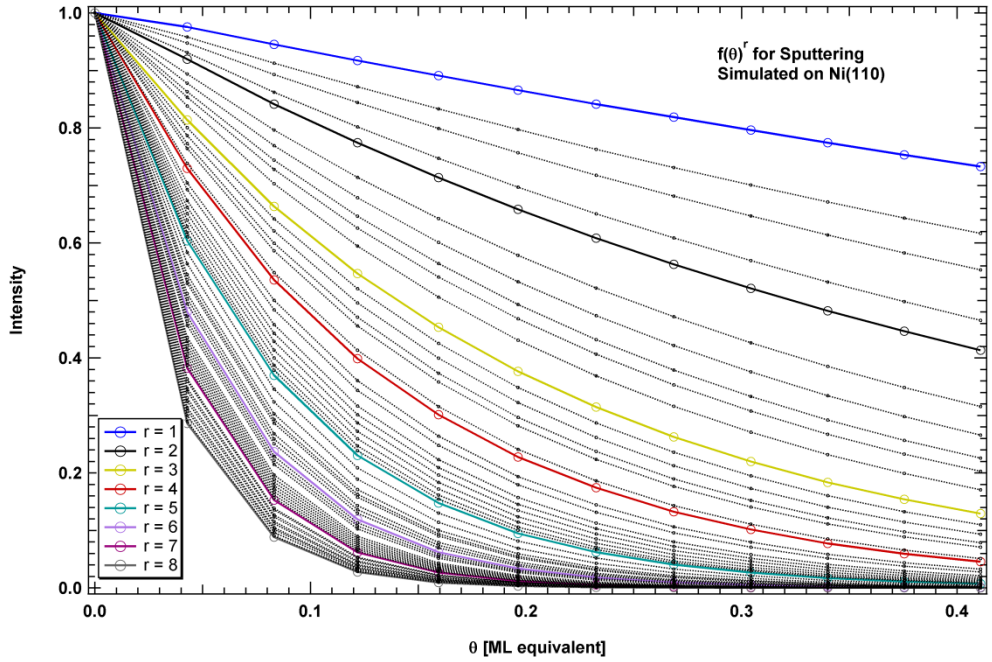

Figure 1-11: Results of the sputtering model simulation displaying $f(\theta)^r$ intensity for various values of r relative to θ. Traces corresponding to r values of 1 (top) through 8 atoms are in bold. Traces corresponding to intermediate r values are dashed.

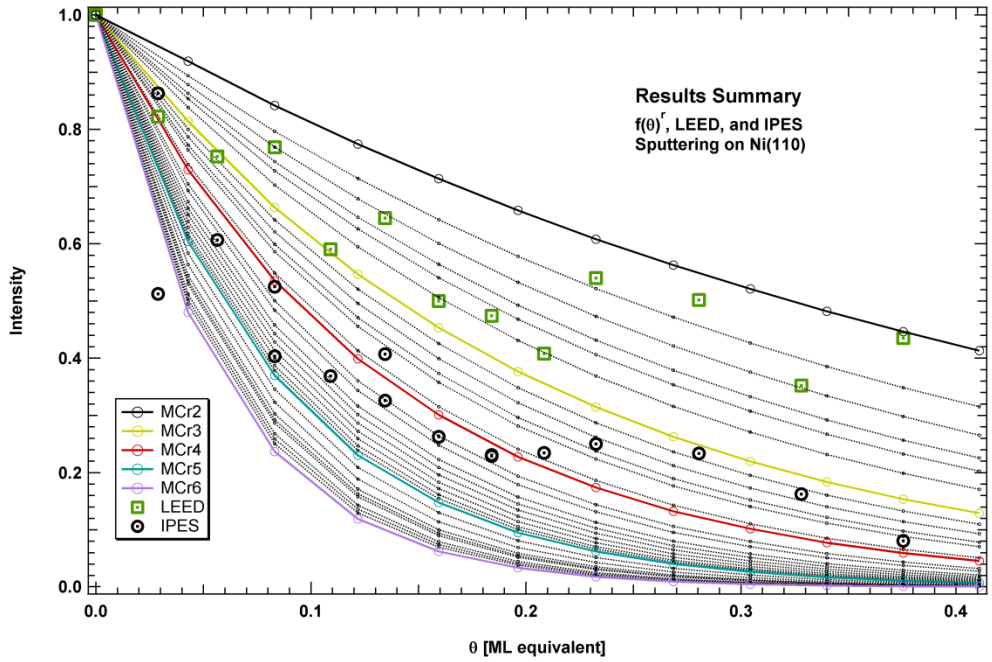

Figure 1-12: LEED (green squares) and IPES (black circles) overlaid on the simulation results. Simulation results corresponding to clean patch radii of N atoms are labeled "MCrN." The LEED and IPES intensites have been normalized to those of the clean sample.

MANUSCRIPT-II

To be submitted to Journal of the American Chemical Society

Hard X-Ray Photoelectron Spectroscopy (HAXPES) Investigation of the Silicon Solid Electrolyte Interphase (SEI) in Lithium-Ion Batteries

Benjamin T. Young[1], David R. Heskett[1], Mengyun Nie[2], Cao Cuong Nguyen[2], Brett L. Lucht[2], Joseph C. Woicik[3]

1) *Department of Physics, University of Rhode Island, Kingston RI*
2) *Department of Chemistry, University of Rhode Island, Kingston RI*
3) *National Institute of Standards and Technology, Gaithersburg MD*

Corresponding Author: Dr. David Heskett

Department of Physics

University of Rhode Island

East Hall, 2 Lippitt Rd.

Kingston, RI 02881, USA

Phone: 1-401-874-2076

Email: dheskett@uri.edu

CHAPTER 2

Hard X-Ray Photoelectron Spectroscopy (HAXPES) Investigation of the Silicon Solid Electrolyte Interphase (SEI) in Lithium-Ion Batteries

Abstract

Binder-Free silicon (BF-Si) nanoparticle anodes from lithium-ion coin cells with electrolyte salt 1.2M $LiPF_6$ in ethylene carbonate (EC), fluoroethylene carbonate (FEC), or a combination of the two have been analyzed by Hard X-Ray Photoelectron Spectroscopy in order to investigate the composition and structure of the surface electrolyte interphase (SEI) that forms during cycling. Our analysis of the silicon spectra support our previous conclusions that the $LiPF_6$/FEC electrolyte generates an SEI layer that is thinner than generated by $LiPF_6$/EC and that the morphological changes to the substrate silicon are greater for batteries with the EC additive. Additionally, the C 1s and F 1s spectra suggest that FEC inclusion in the electrolyte material generates an SEI which is fairly homogeneous in composition at different depths from one to five cycles, while the $LiPF_6$/EC SEI is significantly modified at different depths. We have found the composition of the SEI with the mixed electrolyte formulation to more closely resemble that of the pure EC, but with the greater homogeneity in depth and cycle count. Electrochemical cycling results reveal that the FEC and mixed electrolyte similarly outperform those using pure EC as the electrolyte solvent. Finally, the results of a study on the effects of sample irradiation during HAXPES experiments are presented. These effects can be explained by photon-catalyzed reactions and desorption of oxygen-containing species from the surface of the SEI.

2-1 Introduction

The scaling of secondary batteries for demanding applications necessitates a move away from the industry standard graphite anode construction. With a theoretical specific capacity of 3580 mAh/g in the fully lithiated state, silicon offers an attractive upgrade of almost an order of magnitude over graphite (372 mAh/g) [1]. However, in conjunction with the vast increase in its ability to hold lithium ions, the silicon experiences a volume increase nearly thirty times greater than graphite upon full lithiation [2]. During charge/discharge cycling, silicon volume fluctuations subject the electrode to large mechanical stresses. Associated effects may include pulverization of the electrode material, breaking of electrical contact within the battery, and repeated cracking of the Solid Electrolyte Interphase (SEI) [2] [3].

Two main avenues that are being pursued to overcome this challenge involve novel anode structures and variations of the electrolyte material [4] [5] [6]. As in the graphite anode batteries, the SEI should be as thin as possible in order to minimize hindrance of lithium ion conduction, yet thick enough to protect the electrodes from further decomposition of the electrolyte material. The SEI must also remain stable under the expansion and contraction of the substrate electrode. In addition to modifying the anode material itself, another popular tactic to improve these batteries is adding sacrificial ingredients to the electrolyte. The silicon SEI is reportedly similar to the one grown on graphite, and its properties depend in part on the composition of the electrolyte material [7] [8] [9] [10] [11] [12] [13].

In those studies it was also shown that the SEI grown on silicon anodes is not able to withstand the volume fluctuation associated with cycling. The silicon anode SEI

cracks, revealing new active material for reaction with the electrolyte during each cycle and decreasing capacity retention. If a stable SEI does not form, the layer may continue to grow until the battery fails completely. Researchers are presently investigating various combinations of electrolyte salt, solvent, and additive combinations in concert with novel electrode fabrication techniques to understand their roles in formation of the SEI passivation layer. The attainment of a stable, predictable SEI will be necessary in order to harness the great capacity increase silicon can offer.

The use of binders in the electrode fabrication helps with adhesion of the material to itself and to the current collector, but the binder components are similar to the components of the SEI. Thus, they complicate analysis of the SEI layer in *ex situ* surface investigations. Here we study anodes using binder free silicon (BF-Si) nanoparticles to simplify the analysis. Anodes were extracted from coin cells cycled with two common electrolyte additives, ethylene carbonate (EC) and fluoroethylene carbonate (FEC), to discern the roles these additives play in SEI formation and maturation without the complication of a binder.

A previous study on silicon nanoparticle anodes cycled with $LiPF_6$/EC based electrolytes found differences in the SEI layer at the electrolyte interface versus at the silicon interface [11]. While the layer near the electrolyte material was dominated by lithium alkyl carbonates, deeper down near the substrate silicon it was dominated by Li_xSiO_y from the conversion of the surface oxide layer of the silicon. Inclusion of FEC in the electrolyte material has been investigated with significant improvement in capacity retention [14]. When the concentration of FEC in the electrolyte material is

low, the SEI bears strong resemblance to that which occurs for the pure EC-based electrolyte; however, higher FEC concentration results in increases of LiF and polymeric species in the surface layer [15] [16] [17] [18]. While better performance has been attained through the addition of FEC, the silicon SEI requires further study to develop understanding of how FEC leads to better performance.

This study utilizes Hard X-ray Photoelectron Spectroscopy (HAXPES) to obtain new information on the SEI developed with EC or FEC as solvents. We compare the results to our previous study on these systems [7] which used XPS, FTIR, TEM, and NMR to characterize the SEI, and extend it to include a mix of EC/FEC. High photon energies available from synchrotron sources can access more tightly bound core electrons and impart more energy to less tightly bound ones, which enables characterization of the SEI layer at both shallower and deeper levels in the film than are possible with traditional XPS studies. This has enabled us to provide depth dependent information about SEI development.

2-2 Experimental

2-2.1 Preparation of Binder-Free Silicon Electrodes and Coin Cell Fabrication

BF-Si electrodes were prepared by electrophoretic deposition (EPD) similar to BF-Si [7] and BF-graphite [12] [13] studies previously reported. The EPD bath was prepared by dissolving silicon nanoparticles (~50 nm) in acetonitrile (anhydrous). This method produces electrodes without polymer binders or conductive carbon, being exclusively composed of silicon nanoparticles. The BF-Si electrodes were coated on copper foil with a surface density of ~0.37 mg/cm^2 and vacuum-dried for 24 h at 120

°C. Half cells (CR2032) were fabricated with BF-Si electrodes, a polypropylene separator, and lithium foil in a high purity Ar-filled glove box with H_2O content <0.1 ppm. Three different electrolytes were used: 1.2 M $LiPF_6$ in EC, 1.2 M $LiPF_6$ in FEC, and 1.2 M LiPF6 in a mix of EC:FEC at a ratio of 85:15. Each coin cell contained 30 μL of electrolyte. Following formation cycling, the test cells were cycled 1 or 5 times then disassembled for *ex situ* analysis.

2-2.2 HAXPES Experiments

All HAXPES experiments were conducted at the X-24A end station of the NIST beamline at the National Synchrotron Light Source, Brookhaven National Laboratory (Upton, NY) [19]. Synchrotron radiation from a bending magnet is delivered to a constant offset, double Si(111) crystal monochromator via a Ni-coated graphite spherical collimating mirror and vertical and horizontal apertures. Once monochromatized, the beam is focused by a Ni-coated quartz toroidal mirror. The beam spot size is determined just upstream from the analysis chamber by vertical and horizontal apertures. Oriented perpendicular to the beam in the experimental chamber is the entrance aperture of a 200mm hemispherical analyzer configured to analyze a 0.5 mm spot on the sample positioned in front of it in the analysis chamber. Samples were oriented at grazing incidence to the photon beam, with a takeoff angle toward the analyzer of 3° or 5° relative to the sample normal. This orientation allowed for detection of photoelectrons with the greatest possible mean escape depth. Nominal photon energies and resolutions were determined by measuring the Ag 3d signal from a silver standard foil attached to our sample bar. Total resolution for the analyzer and beamline, established as the half-width of the Fermi edge at the top of the valence

band maximum, was measured to be 0.45 and 0.55 eV for excitation energies 2.2 and 4 keV, respectively.

To minimize exposure of the samples to atmosphere, we took the following precautions: anodes from batteries described above were affixed with conductive carbon dots to a custom stainless steel bar capable of holding 32, 1cm x 1cm electrodes in an argon glove box at URI. The bar was sealed in a custom vessel in the glove box before removing and transporting it to Brookhaven National Lab where it was placed in a glove bag, sealed around the fast turnaround load lock port of the preparatory chamber at X-24A. A positive pressure of nitrogen was flown through the chamber and attached bag while the bar was removed from its container, installed on the chamber's 3-axis manipulator, and the load lock closed. After stopping the gas flow, the preparatory chamber was evacuated for 12 h by turbomolecular pumping before lowering the samples into the experimental chamber. Experimental chamber pressure was less than $5x10^{-9}$ Torr. The sample bar was electrically connected through the manipulator to a common ground with the analyzer, but no further attempt was made to correct for charging of the samples during measurements.

To minimize beam effects on the samples, a minimum number of spectra were collected in standardized order at a unique spot on each sample and a new spot was analyzed at each excitation energy. For this investigation we used photon energies of 2.2 and 4 keV. We collected spectra of Si 1s, F 1s, O 1s, C 1s, Si 2s, P 2p, Si 2p, and Li 1s electrons at both photon energies, and at 4 keV we also took spectra of the P 1s electron. All spectra were recorded with a dwell time of 100 ms and energy step of

100 meV, with the analyzer in transmission mode, and all used analyzer pass energy of 500 eV except the Si 1s electron at 2.2 keV (pass energy 200 eV).

Spectra were analyzed with Wavemetrics' IGOR Pro software. All spectra were scaled by the number of scans taken to obtain comparable intensities between them before subtraction of a Shirley background [20]. Fits to the experimental data were performed using Voigt shapes, the parameters of which were defined by the shape of the Ag standard peaks at each photon energy. Relative atomic concentrations for each element, I_i, were calculated using the formula,

$$I_i = \frac{A_i}{T(KE)_i\,\sigma(h\nu)_i\,\lambda(KE)_i} \Big/ \sum_j \frac{A_j}{T(KE)_j\,\sigma(h\nu)_j\,\lambda(KE)_j},$$

where A corresponds to the background-subtracted spectrum area, T is the relative transmission function of the X-24A analyzer [21], σ is the Scofield photoionization cross section [22], λ is the inelastic mean free path of electrons in the material [23], and the summation index j runs over all distinct elements present in the analysis. Where there were two or more available electrons per element, we chose the one used in similar calculations for the Al-Kα XPS experiments performed at URI. The kinetic energy scale used for data collection was converted to binding energy for display by referencing a fit to the hydrocarbon contamination peak at 285 eV in the C 1s spectrum for each sample.

2-3 **Results**

2-3.1 Electrochemical Cycling

First (Figure 2-13) and fifth (Figure 2-14) cycle charge/discharge profiles are shown as plots of potential vs. capacity. The curves for cells with EC + 15% FEC are nearly indistinct from those with pure FEC in the first cycle and show slightly better

performance for the fifth cycle. For all profiles, the cells containing FEC outperform the cells with just EC, both in total capacity and capacity retention. A detailed analysis of the cycling for EC and FEC systems has been previously reported [7].

2-3.2 HAXPES Measurements

Fluorine spectra are reported in Figure 2-15, shown as plots of signal intensity vs. binding energy. The plots are arranged in columns corresponding to the photon energy and in rows corresponding to the electrolyte formulation (EC top, ECw15%FEC middle, FEC bottom). Two spectra are displayed on each plot representing the data from the one and five cycle anodes. All spectra exhibit a broad peak at 685 eV, attributed to the LiF bond, as well as a shoulder at higher binding energy which indicates the presence of the $LiPF_6$ salt. For the HAXPES EC spectra (top row, right two plots in the figure) the relative atomic concentrations reported in Table 2-1 indicate approximately 13-16% of the observed signal comes from fluorine, significantly lower than what was observed in the more surface sensitive XPS experiment using 1487 eV photons. The HAXPES concentrations agree more closely with the XPS results for the FEC samples, where the concentrations are between 20 and 28% (Table 2-3). Fluorine concentrations for the mixed solvent electrolyte were by far the smallest, as reported in Table 2-2.

The spectra for the C 1s core levels are presented in Figure 2-16. The peak at binding energy 285 eV represents universal hydrocarbon contamination. Proceeding to higher binding energies, we have first the signal from C-O bonded species at 286.5 eV, then C=O species at 288.5 eV, and finally lithium (alkyl) carbonates at 289.5-290 eV. This final signature is significantly higher in intensity for all HAXPES spectra

relative to the XPS results, and the intensity is higher for electrolyte formulations containing EC for the first cycle. For pure EC, there is a more pronounced intensity drop between one and five cycles than for the mixed solvent. For both samples containing EC, the intensity of this peak increases with increasing excitation energy. A similar trend, though less pronounced, is displayed in the signal for the C-O bond. For the pure FEC solvent samples, the carbon spectra are not markedly different by excitation energy or cycle count. The atomic concentrations for all samples indicate a trend of less relative carbon at higher excitation energy.

Lithium spectra are presented in Figure 2-17. The individual spectra for the Li 1s electron displayed in the figure are all single peaks which are convolutions of lithium-containing species. Indicated in the figure at 55.7 and 55.2 eV are lines corresponding to the binding energies of LiF and lithium carbonate, respectively. The top row spectra corresponding to the pure EC solvent appear to be centered between the indicators for the two identified species or shifted to lower binding energy, indicating more Li_2CO_3 presence. This is different for the FEC spectra on the bottom row, where the peak is clearly shifted toward the LiF indicator at higher binding energy. The spectra for the mix in the middle row more closely resemble the spectra for the pure EC solvent above them, except in the case of the fifth cycle anode with 4 keV excitation, than those of pure FEC below. Atomic concentrations for lithium are generally not reported in XPS studies of battery electrodes because the signal-to-noise ratios are unsatisfactory and the small cross section for the 1s electron magnifies this problem. To maintain comparable information with the XPS data, we have omitted the lithium signal in Tables 2-1 through 2-3, though the HAXPES signal-to-noise ratio

is vastly improved over XPS. Our analysis indicates lithium-containing species are responsible for 30-34% of the observed signal in all samples when included in the calculations.

Oxygen concentrations are reported in Tables 2-1 through 2-3, and the spectra are displayed in Figure 2-18. All expected species have similar binding energies in the O 1s spectrum. As a result, all O 1s spectra exhibited a broad peak with little variation. The atomic concentrations indicate for all samples at depths below the previously reported XPS results that the relative signal intensity of oxygen-containing species increases for greater excitation energy, and in general, decreases between one and five cycles.

Figure 2-19 is an array of silicon spectra including both the 1s and 2p core levels. For any given excitation energy, since the binding energy of the 1s electron is higher by about 1740 eV than that of the 2p, the signal from that electron comes from a much shallower average depth in the sample. The left column displays 1s spectra taken with 2.2 keV photons, a more surface sensitive measurement than our XPS data for the Si 2p signal displayed in the next column. The rightmost column represents information for the Si 2p electron at 4 keV and is our most bulk-sensitive measurement for silicon. The spectra in the top column for the fresh anodes exemplify the depth profiling available. In the most surface sensitive measurement, the peak corresponding to the native oxide layer encapsulating the Si nanoparticles is more intense than the elemental silicon peak to its right. Moving to the right, the intensity ratio changes until we arrive at the deepest information at far right, where the oxide signal is dwarfed by the much more intense elemental peak. As expected for the cycled

anodes, the peaks attributed to elemental silicon (1s: 1839 eV and Si 2p: 99.8 and 99.2 eV) are not obviously present. Their signatures are overwhelmed by the relative intensity of a very close peak (1-1.5 eV left) due to lithium silicate, Li_xSiO_y, which Philippe and coworkers suggested to be due to Li_4SiO_4 [11]. Another new species appears 2.5 eV to the high binging energy side of the elemental silicon, corresponding to lithium silicide (Li_xSi). Most silicon spectra display some differential charging which shifts the peaks of oxygen-containing species by approximately 2 eV to higher binding energy.

2-4 Discussion

The fluorine spectra from samples containing FEC do not show an obvious shoulder indicative of $LiPF_6$ salt as is seen in the pure EC samples. However, the intensity of the LiF peak at 685 eV coupled with the overall relative intensity of the fluorine signal in Table 2-1 through 2-3 indicate there is a greater LiF contribution for cells with FEC in the electrolyte which probably obscures the salt shoulder in these spectra. There are no large differences between the one and five cycle spectra for electrolyte formulations containing FEC and no obvious changes are observed between spectra taken at different photon energies, indicating that the SEI is relatively homogeneous and does not change significantly between one and five cycles. The spectra from the pure EC formulation exhibit different behavior. The ratio of $LiPF_6$ salt to LiF decreases from one to five cycles at both 2.2 and 4 keV, indicating that the SEI developed with the EC solvent is modified beyond the first cycle. The five-cycle spectra indicate that less unreacted salt, relative to LiF, is incorporated in the SEI as it grows. Comparing the five-cycle EC spectra taken at 2.2 and 4 keV reveals that there

is a slightly larger relative $LiPF_6$ and slightly larger total signal intensity (Table 2-1) deeper in the sample, showing inhomogeneity not observed for either formulation containing FEC. The mixed solvent generates fluorine spectra that indicate an intermediate SEI composition between that of the pure EC and FEC formulations. The atomic concentrations for fluorine in the mixed samples (Table 2-2) are relatively low but this can be explained by noting the significant increases to the oxygen and carbon concentrations relative to the pure samples.

For Li 1s spectra from both one and five-cycle pure EC samples, the ratio of total Li:F intensities is roughly 3:1 for spectra taken at 4 keV excitation energy. Nearer the surface, at 2.2 keV, the ratio is higher at about 4:1. For both one and five-cycle FEC-based samples this ratio is slightly above 2:1 for both photon energies with little variation, indicating the FEC-based SEI is more homogeneous relative to depth and cycle count than that of the pure EC formulation. If the addition of FEC to the electrolyte sacrificially provides fluorine for SEI formation, which the higher concentrations in Table 2-1 vs. Table 2-3 suggest, this may help to explain the relative performance gains of batteries that include the FEC solvent.

Further insight may be gained by inspecting the carbon results. The higher ratio of Li:F in the EC sample may be explained by the dramatically larger peak at 290 eV in the carbon spectra, attributed to Li_2CO_3 or lithium alkyl carbonates. This peak is not clearly distinguished from the background in the XPS spectra (1487 eV), but it rises relative to the hydrocarbon peak for 2.2 and 4 keV spectra. While the relative concentration of that species increases deeper into the sample, looking at the atomic concentrations in Table 2-1 reveals that the total carbon intensity decreases. While

there are less carbonaceous species at deeper levels, more of what's there can be attributed to lithium (alkyl) carbonates.

For the FEC samples, we see again a peak in the carbon spectrum at 290 eV binding energy which increases in intensity for the deeper measurements at 2.2 and 4 keV as in the EC samples' spectra. The difference, however, is that the spectra taken for the FEC SEI at 2.2 and 4 keV excitation are very similar and the 290 eV peak remains less than half the intensity of the hydrocarbon peak. This is in line with the steady Li:F ratio for the FEC samples and indicates a more homogeneous SEI layer developed for the FEC solvent. The only notable inhomogeneity is the reduction of a peak at 286.5 eV, which we have assigned as the C-O bond, between one and five cycles. Spectra for the mixed electrolyte have a stronger intensity at 290 eV but the lowest intensities of all samples at 286.5 eV. The signature of lithium alkyl carbonates is a pair of peaks, nearly equal in intensity, at these two energies while the lithium carbonate appears with much more intensity at 290 eV. Assuming the signal at these two energies is some combination of these, the difference between the 286.5 and 290 eV peaks may be understood as lithium carbonate. That the intensity at 286.5 eV is so weak in the mixed electrolyte spectra indicates the 290 eV peak is mostly lithium carbonate. This peak decreases in intensity relative to the other species from one to five cycles, as in both pure solvent formulations, but it remains with higher intensity after five cycles for the mix. While the ratios of individual species in the mix spectra more closely resemble those for EC, the homogeneous character of the SEI in depth and cycle count is more comparable to that of the FEC samples.

We can obtain some information about the relative thickness of the SEI for each electrolyte formulation by observing the silicon spectra in Figure 2-19. Upon cycling, we expect lithium to react with the silicon to produce lithium silicide, Li_xSi (97.5 eV in Si 2p, 1837 eV in Si 1s), and with the oxide to produce lithium silicate, Li_xSiO_y (100-101 eV in Si 2p, 1840-1841 eV in Si 1s). The relative intensities of these peaks in the various silicon spectra provide some depth information. The most surface sensitive spectra in Figure 2-19 (Si 1s at 2.2 keV) do not exhibit any Li_xSi for any spectrum. Contrast this with the spectra for the Si 2p at 4 keV for all three formulations where this peak is clearly resolved in all cases. It is the dominant feature of the pure FEC one cycle spectrum, but Li_xSiO_y is the dominant peak in all spectra for formulations containing EC. The signal comes from the same depth, on average, for each spectrum in the column, so the intensity of the Li_xSi peak, relative to the other species, is inversely related to the SEI thickness. This relative intensity increase of the Li_xSi peak from the spectra corresponding to electrolyte formulations using pure EC, to EC with 15% FEC, to pure FEC indicates that inclusion of FEC in the electrolyte material helps to generate a thinner SEI.

The similarity of the EC spectra between one and five cycles supports the TEM results in our previous paper which showed that the SEI formed for the pure EC formulation is thicker than for pure FEC and incorporates the silicon nanoparticle substrate as it grows [7]. In that work we observed that the Si nanoparticles remained intact and distinguishable beneath the SEI layer for FEC battery cycling in excess of what obscured the substrate material in EC batteries. This indicated that the nanoparticles are not incorporated in the SEI as extensively in the FEC formulation.

That conclusion is supported here as well. In the spectra of the right two columns of Figure 2-19, the intensity ratios of oxygen-containing species (SiO_2, Li_xSiO_y) to the deeper Li_xSi in the FEC spectra increase from one to five cycles. This is consistent with an SEI that grows on top of the substrate material. Similar changes to the mixed electrolyte spectra from one to five cycles are less dramatic, and there is almost no discernible change for the samples cycled in the pure EC electrolyte formulation. This indicates that the SEI for samples with FEC in the formulation grows with less incorporation of the substrate material.

2-5 Radiation Effects

Radiation-induced changes to the samples under investigation are generally to be avoided in photoemission experiments for obvious reasons. Other authors have identified this in passing [11] [10], noting preventative measures like minimizing scan numbers and decreasing photon flux, but to our knowledge, there has been no record of the extent to which exposure to X-rays in our range modifies the complex SEI system or the underlying structure. We report here on the effects of 4 keV synchrotron radiation on the BF-Si nanoparticle anode from a battery cycled 20 times with FEC as the electrolyte solvent.

Figure 2-20 shows spectra of the 1s electrons of carbon, phosphorus, silicon, and oxygen taken at 25 minute intervals while the sample was constantly exposed to the photon beam at grazing incidence. The most striking features are observed in the C 1s (upper left) and O 1s (lower left) spectra. In the carbon spectrum, there is a very clear reduction in the peaks we have assigned to species with C-O (286.5 eV), O=C-O (288.5 eV), and C-F (291 eV) bonds. In the oxygen spectra, the major feature is the

reduced intensity of the shoulder on the high binding energy side of the broad peak. We assign this shoulder to the C-O bond (binding energy 534.5 eV) consistent with the concomitant change in the carbon spectra. These changes can be explained by desorption of oxygen-containing species from the surface layer. That the Li_2CO_3 intensity is not obviously changed in the carbon and oxygen spectra support the conclusion that lithium carbonate is preferentially formed deeper in the layer as suggested by Edstrom, et al. [24] and/or is less sensitive to beam exposure. In Figure 2-21, the integrated intensity of each spectrum is plotted against exposure time and the curves are normalized to the initial observed intensity for each element. The carbon and oxygen traces both decrease in a linear, nearly identical fashion over time, consistent with desorption.

In contrast, the phosphorus trace in Figure 2-21 does not indicate significant changes in total intensity. Inspecting the phosphorus progression in the top right pane of Figure 2-20 reveals that the relatively constant total signal may be a result of intensity redistribution indicating recombination. The P 1s spectra show a reduction in intensity of the higher binding energy peak attributed to the electrolyte salt $LiPF_6$ (2151.5 eV), and a slight increase in the broad peak at lower binding energy assigned to phosphates. These results could be explained by radiation-induced decomposition of the $LiPF_6$ salt, as phosphates are an expected product of its decomposition [25].

The total intensity for silicon species in Figure 2-21 rises for the first 2.5h and is afterward relatively constant. This result is mirrored in the spectra displayed in Figure 2-20, where all silicon peaks appear to gain some intensity over time with nothing decreasing. Desorption indicated in the carbon and oxygen spectra may impact the

thickness of the SEI to such an extent that more silicon is visible to the technique, which could explain the apparent intensity increases of all identified species.

2-6 Conclusions

The SEI layers from coin cells with BF-Si nanoparticle anodes cycled with 1.2M LiPF6 electrolyte salt in EC, FEC, and a combination of the two as solvents has been investigated. Electrochemical cycling data show only small differences between the performance of pure FEC and EC+15%FEC as solvent material. Cells containing FEC cycled better than those with only EC in all tests. This suggests the FEC additive plays a strong role in modifying the battery chemistry, even in amounts as small as the 15% concentration.

Both pure solvent SEIs have comparable, high fluorine concentration on the surface, but that of FEC maintains higher concentration deeper in the layer while the EC concentrations are lower there. This indicates inhomogeneity at different depths of the SEI developed when pure EC is used as the solvent. Changes to the fluorine and carbon spectra from one to five cycles indicate the SEI is modified beyond the first cycle for EC solvent. The pure FEC solvent C 1s spectra, on the other hand, suggest little change to the SEI between one and five cycles, and are nearly indistinct for changes in photon energy, indicating a much more homogeneous SEI developed with FEC solvent.

Silicon spectra indicate that the SEI formed for electrolytes containing EC solvent is thicker after one and five cycles. The relative intensities of the Li_xSi peaks in the 4 keV spectra indicate that the FEC solvent produces a thinner SEI. The mixed

electrolyte formulation produces an SEI of intermediate thickness between the pure FEC formulation and that of the pure EC, which was thickest.

Our study of beam effects reveals that there is modification to the system due to irradiation involving both photo-catalyzed reactions and desorption.

2-7 Acknowledgements

Use of the National Synchrotron Light Source, Brookhaven National Laboratory, was supported by the U.S. Department of Energy, Office of Science, Office of Basic Energy Sciences, under Contract No. DE-AC02-98CH10886. We gratefully acknowledge funding from Department of Energy, Office of Basic Energy Sciences, EPSCoR Implementation award (DE-SC0007074). Additional support was provided by the National Institute of Standards and Technology.

2-8 References

[1] M. N. Obrovac and I. Christensen, "Structural Changes in Silicon Anodes During Lithium Insertion/Extraction," *Electrochemical Solid State Letters,* vol. 7, pp. A93-A96, 2004.

[2] M. J. Chon, V. A. Sethuraman, A. McCormick, V. Srinivasan and P. R. Guduru, "Real-Time Measurement of Stress and Damage Evolution During Initial Lithiation of Crystalline Silicon," *Physical Review Letters,* vol. 107, p. 045503, 2011.

[3] R. Benedek and M. M. Thackeray, "Lithium Reactions with Intermetallic-Compound Electrodes," *Journal of Power Sources,* vol. 110, pp. 406-411, 2002.

[4] Y. R. Ren, J. N. Ding, N. Y. Yuan, S. Y. Jia, M. Z. Qu and Z. L. Yu, "Preparation and Characterization of Silicon Monoxide/Graphite/Carbon Nanotubes Composite as Anode for Lithium-Ion Batteries," *J. Solid State Electrochem.,* vol. 16, pp. 1453-1460, 2012.

[5] H. Wu and Y. Cui, "Designing Nanostructured Si Anodes for High Energy Lithium Ion Batteries," *Nano Today,* vol. 7, pp. 414-429, 2012.

[6] H. C. Shin and M. Liu, "Copper Foam Structures with Highly Porous Nanostructured Walls," *Chem. Mater.,* vol. 16, pp. 5460-5464, 2004.

[7] M. Nie, D. P. Abraham, Y. Chen, A. Bose and B. L. Lucht, "Silicon Solid Electrolyte Interphase (SEI) of Lithium Ion Battery Characterized by Microscopy and Spectroscopy," *J. Phys. Chem. C,* vol. 117, pp. 13403-13412, 2013.

[8] S. Y. Li, X. L. Xu, X. M. Shi, B. C. Li, Y. Y. Zhao, H. M. Zhang, Y. L. Li, W. Zhao, X. L. Cui and L. P. Mao, "Composition Analysis of the Solid Electrolyte Interphase Film on Carbon Electrode of Lithium-Ion Battery Based on Lithium Difluoro (Oxalate) Borate and Sulfolane," *J. Power Sources,* vol. 217, pp. 503-508, 2012.

[9] K. Xu, "Nonaqueous Liquid Electrolytes for Lithium-Based Rechargeable Batteries," *Chem. Rev.,* vol. 104, pp. 4303-4318, 2004.

[10] B. Philippe, R. Dedryvère, M. Gorgoi, H. Rensmo, D. Gonbeau and K. Edström, "Role of the LiPF6 Salt for the Long-Term Stability of Silicon Electrodes in Li-Ion Batteries − a Photoelectron Spectroscopy Study," *Chem. Mater.,* vol. 25, pp.

394-404, 2013.

[11] B. Philippe, R. Dedryvère, J. Allouche, F. Lindgren, M. Gorgoi, H. Rensmo, D. Gonbeau and K. Edström, "Nanosilicon Electrodes for Lithium-Ion Batteries: Interfacial Mechanisms Studied by Hard and Soft X-Ray Photoelectron Spectroscopy," *Chem. Mater.,* vol. 24, pp. 1107-1115, 2012.

[12] S. H. Kang, D. P. Abraham, A. Xiao and B. L. Lucht, "Investigating the Solid Electrolyte Interphase Using Binder-Free Graphite Electrodes," *J. Power Sources,* vol. 175, pp. 526-532, 2008.

[13] A. Xiao, L. Yang, B. L. Lucht, S. H. Kang and D. P. Abraham, "Examining the Solid Electrolyte Interphase on Binder-Free Graphite Electrodes," *J. Electrochem. Soc.,* vol. 156, pp. A318-A327, 2009.

[14] R. Elazari, G. Salitra, G. Gershinsky, A. Garsuch, A. Panchenko and D. Aurbach, "Li Ion Cells Comprising Lithiated Columnar Silicon Film Anodes, TiS_2 Cathodes and Fluoroethyene Carbonate (FEC) as a Critically Important Component," *J. Electrochem. Soc.,* vol. 159, pp. A1440-A1445, 2012.

[15] N. S. Choi, K. H. Yew, K. Y. Lee, M. Sung, H. Kim and S. S. Kim, "Effect of Fluoroethylene Carbonate Additive on Interfacial Properties of Silicon Thin-Film Electrode," *J. Power Sources,* vol. 161, pp. 1254-1259, 2006.

[16] S. Dalavi, P. Guduru and B. L. Lucht, "Performance Enhancing Electrolyte Additives for Lithium Ion Batteries with Silicon Anodes," *J. Electrochem. Soc.,* vol. 159, pp. A642-A646, 2012.

[17] V. Etacheri, O. Haik, Y. Goffer, G. A. Roberts, I. C. Stefan, R. Fasching and D. Aurbach, "Effect of Fluoroethylene Carbonate (FEC) on the Performance and Surface Chemistry of Si-Nanowire Li-Ion Battery Anodes," *Langmuir,* vol. 2011, pp. 965-976, 2011.

[18] H. Nakai, T. Kubota, A. Kita and A. Kawashima, "Investigation of the Solid Electrolyte Interphase Formed by Fluoroethylene Carbonate on Si Electrodes," *J. Electrochem. Soc.,* vol. 158, pp. A798-A801, 2011.

[19] C. Weiland, A. K. Rumaiz, P. Lysaght, B. Karlin, J. C. Woicik and D. Fischer, "NIST high throughput variable kinetic energy hard X-ray photoelectron spectroscopy facility," *J. Electron Spectrosc. Relat. Phenom.,* vol. 190, pp. 193-200, 2013.

[20] D. A. Shirley, "High Resolution X-Ray Photoemission Spectrum of the Valence Bands of Gold," *Phys. Rev. B.,* vol. 5, pp. 4709-4714, 1972.

[21] C. Weiland, R. Browning, B. A. Karlin, D. A. Fischer and J. C. Woicik, "Note: Alignment/focus dependent core-line sensitivity for quantitative chemical analysis in hard x-ray photoelectron spectroscopy using a hemispherical electron analyzer," *Rev. Sci. Instrum.,* vol. 84, p. 036106, 2013.

[22] J. H. Scofield, "Theoretical Photoionization Cross Sections From 1 to 1500 keV," Lawrence Livermore Laboratory, Livermore, 1973.

[23] L. R. Painter, E. T. Arakawa, M. W. Williams and J. C. Ashley, "Optical Properties of Polyethylene: Measurement and Applications," *Radiation Reseach,* vol. 83, no. 1, pp. 1-18, 1980.

[24] K. Edström, M. Herstedt and D. P. Abraham, "A new look at the solid electrolyte interphase on graphite anodes in Li-ion batteries," *J Power Sources,* vol. 153, no. 2, pp. 380-384, 2006.

[25] C. L. Campion, W. Li and B. L. Lucht, "Thermal Decomposition of $LiPF_6$- Based Electrolytes for Lithium-Ion Batteries," *J. Electrochem. Soc.,* vol. 152, no. 12, pp. A2327-A2334, 2005.

2-9 Figures

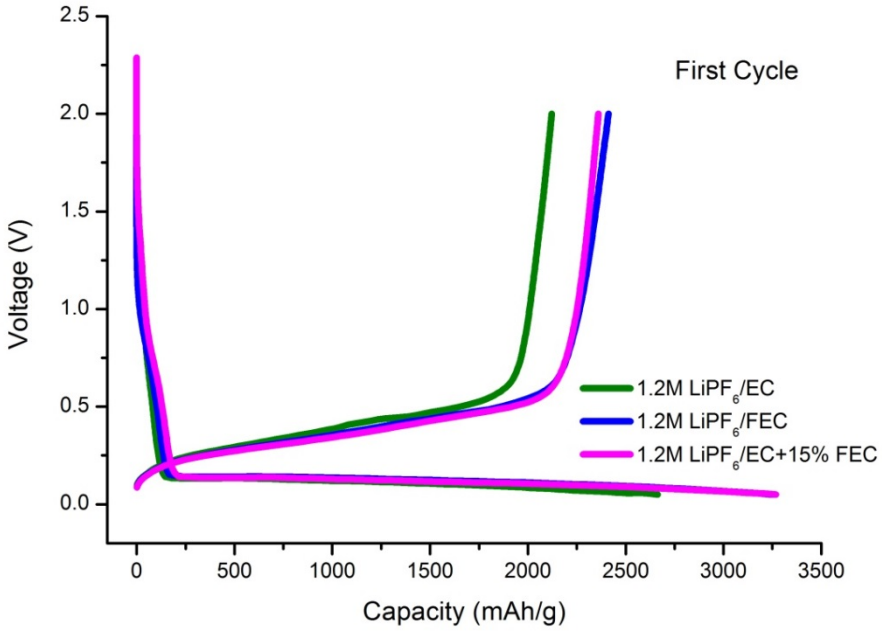

Figure 2-13: First cycle charge/discharge profiles for coin cells with electrolyte 1.2M$LiPF_6$ and EC (green), FEC (blue), or EC+15% FEC (magenta)

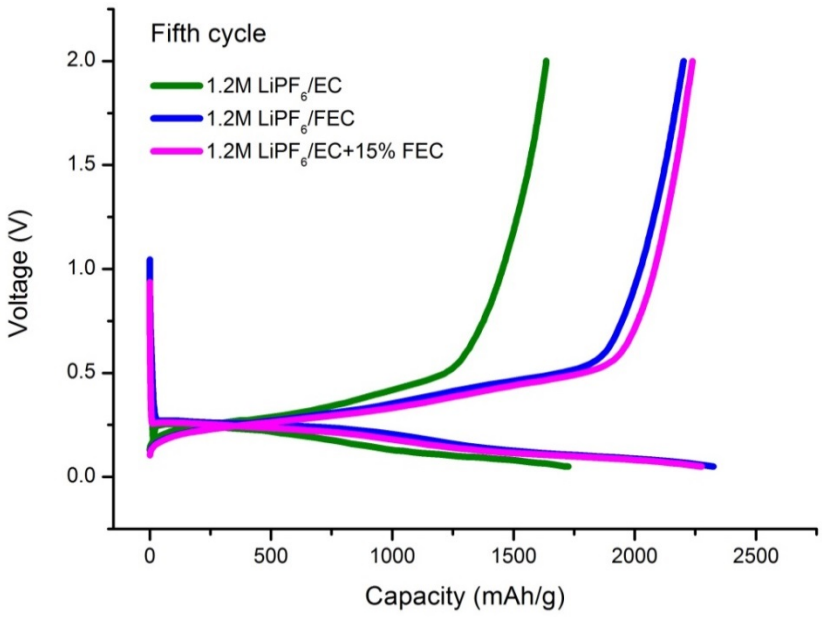

Figure 2-14: Fifth cycle charge/discharge profiles for coin cells with electrolyte 1.2M$LiPF_6$ and EC (green), FEC (blue), or EC+15% FEC (magenta)

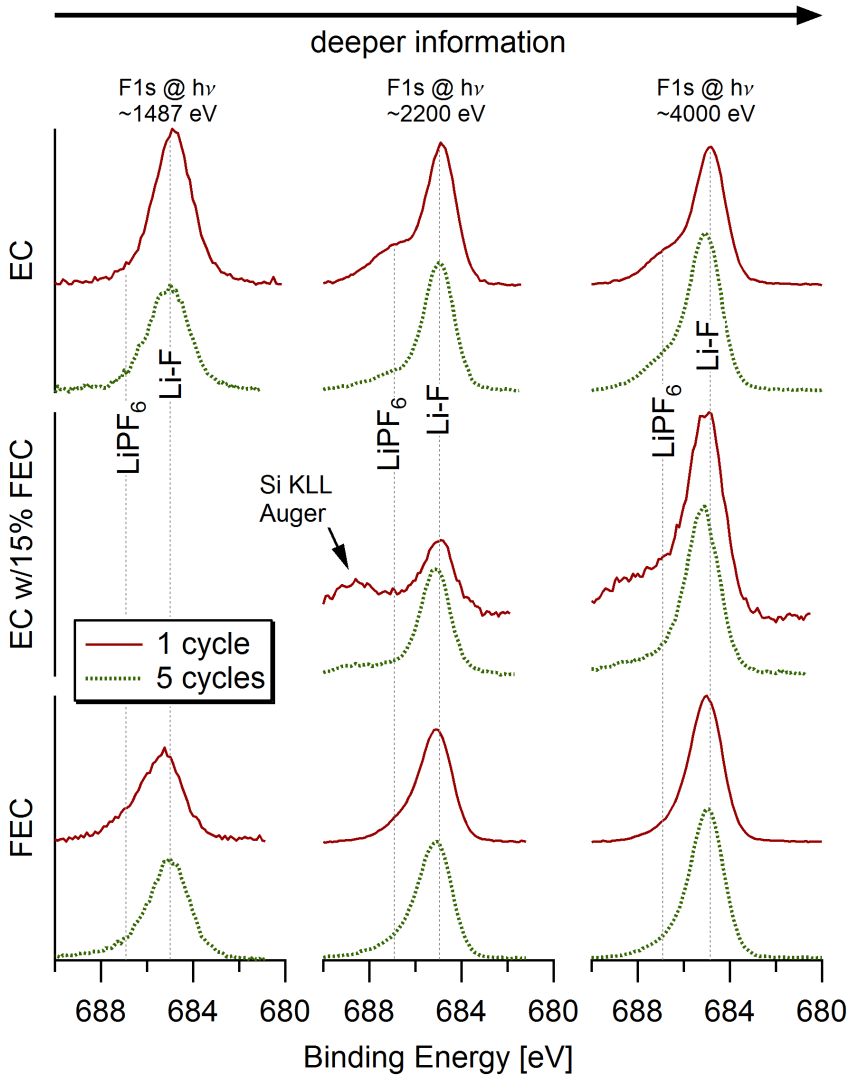

Figure 2-15: Fluorine 1s spectra for the first (red) and fifth (green) cycle BF-Si anodes from coin cells fabricated with electrolyte solvent EC (first row), EC+15%FEC (2nd row), and FEC (3rd row). A silicon KLL Auger transition is visible in the spectrum for the one cycle mixed electrolyte sample at 2.2 keV because a slightly different photon energy was used.

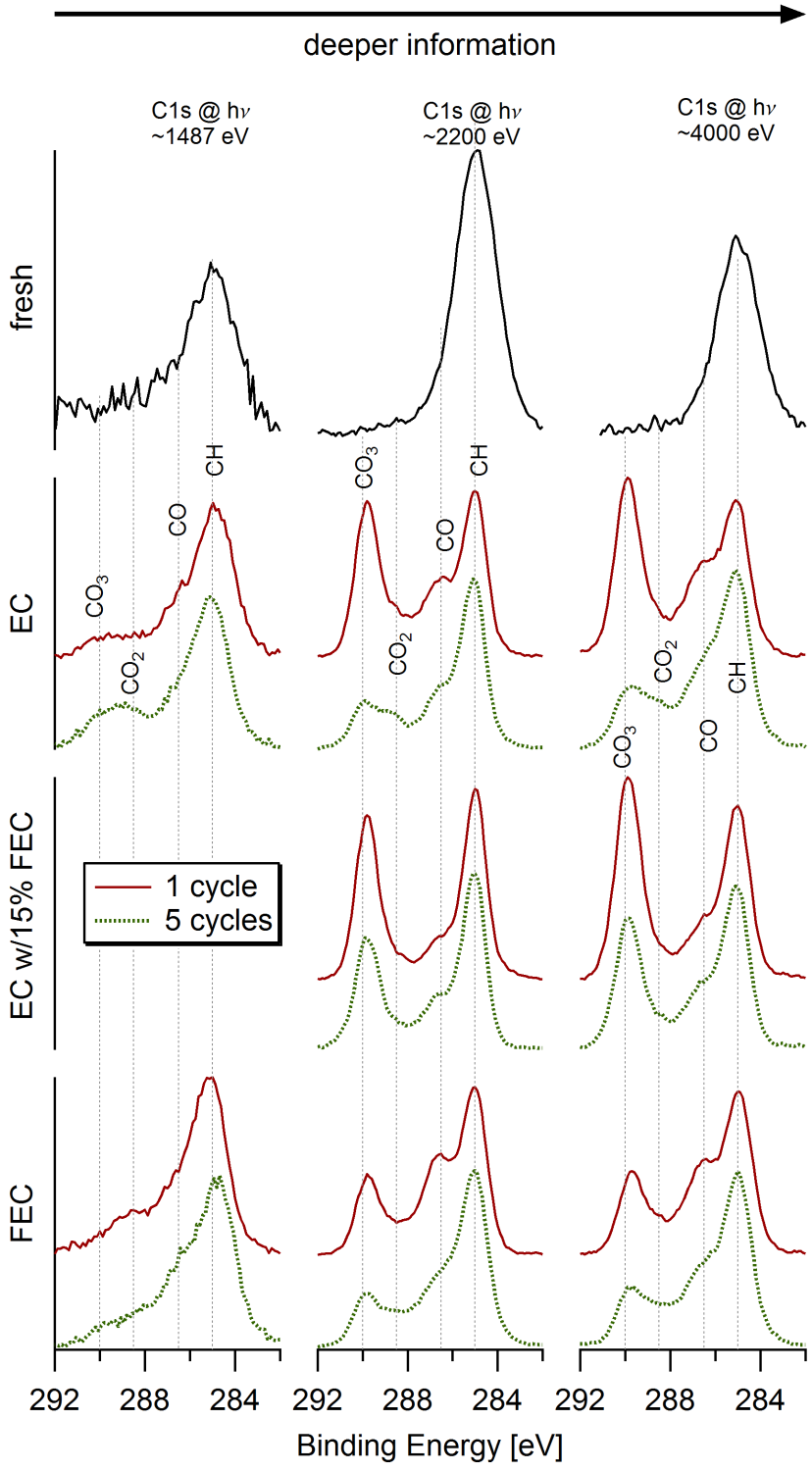

Figure 2-16: Carbon 1s spectra of pristine BF-Si anodes (top row) and for first (red) and second (green) cycle BF-Si anodes from coin cells fabricated with electrolyte solvent EC (2nd row), EC+15% FEC (3rd row), and FEC (bottom row).

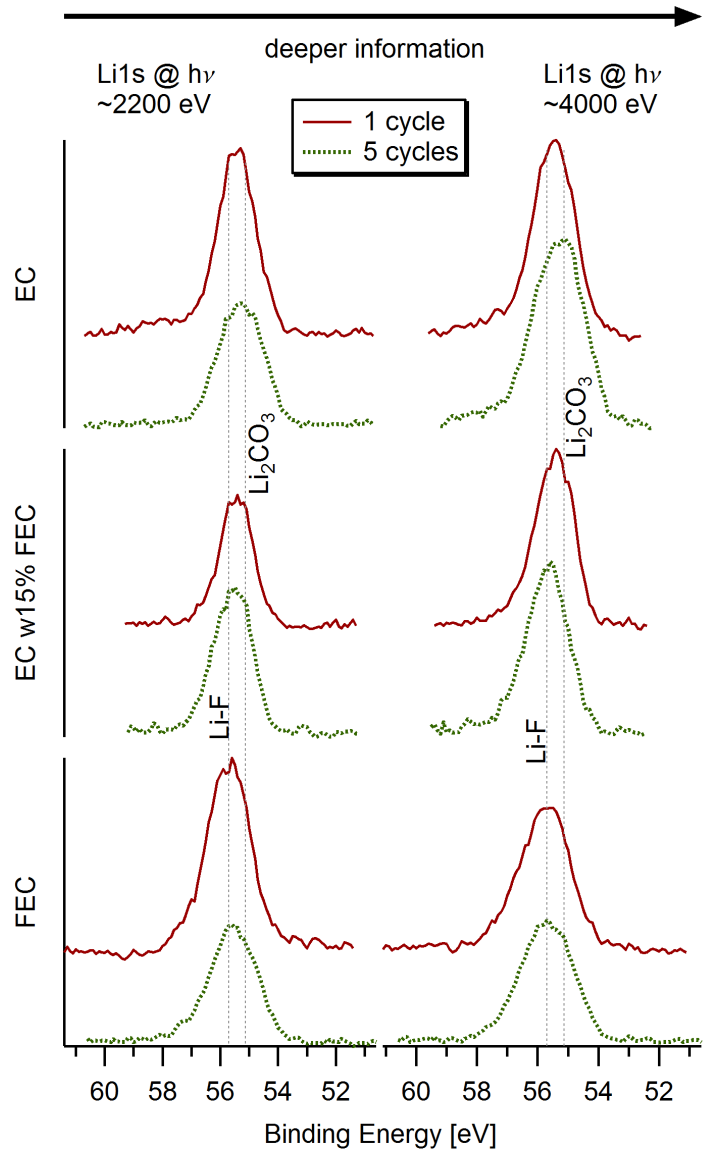

Figure 2-17: Lithium 1s spectra for the first (red) and fifth (green) cycle BF-Si anodes from coin cells fabricated with electrolyte solvent EC (first row), EC+15%FEC (2nd row), and FEC (3rd row).

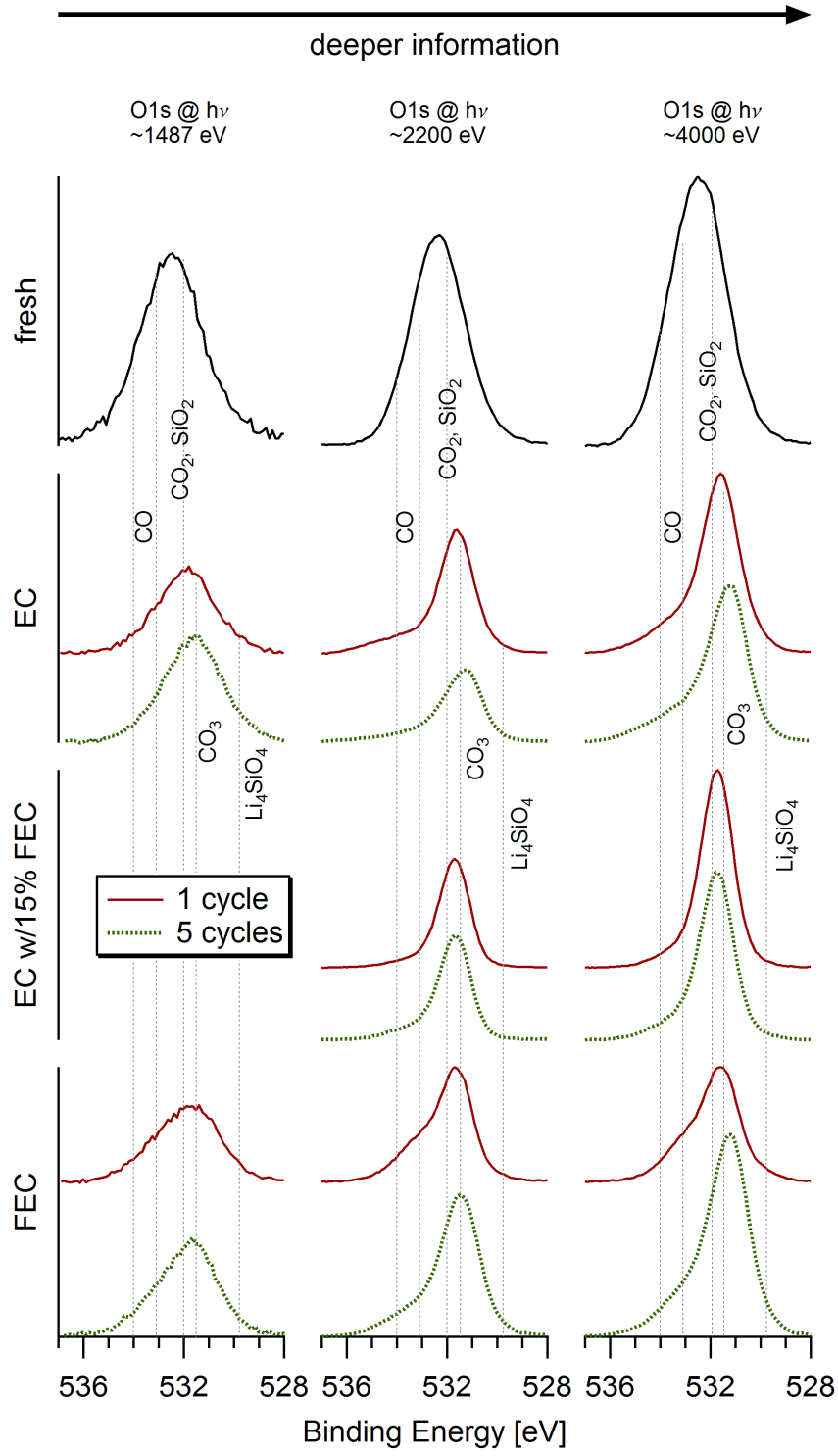

Figure 2-18: Oxygen 1s spectra of pristine BF-Si anodes (top row) and for first (red) and second (green) cycle BF-Si anodes from coin cells fabricated with electrolyte solvent EC (2nd row), EC+15% FEC (3rd row), and FEC (bottom row).

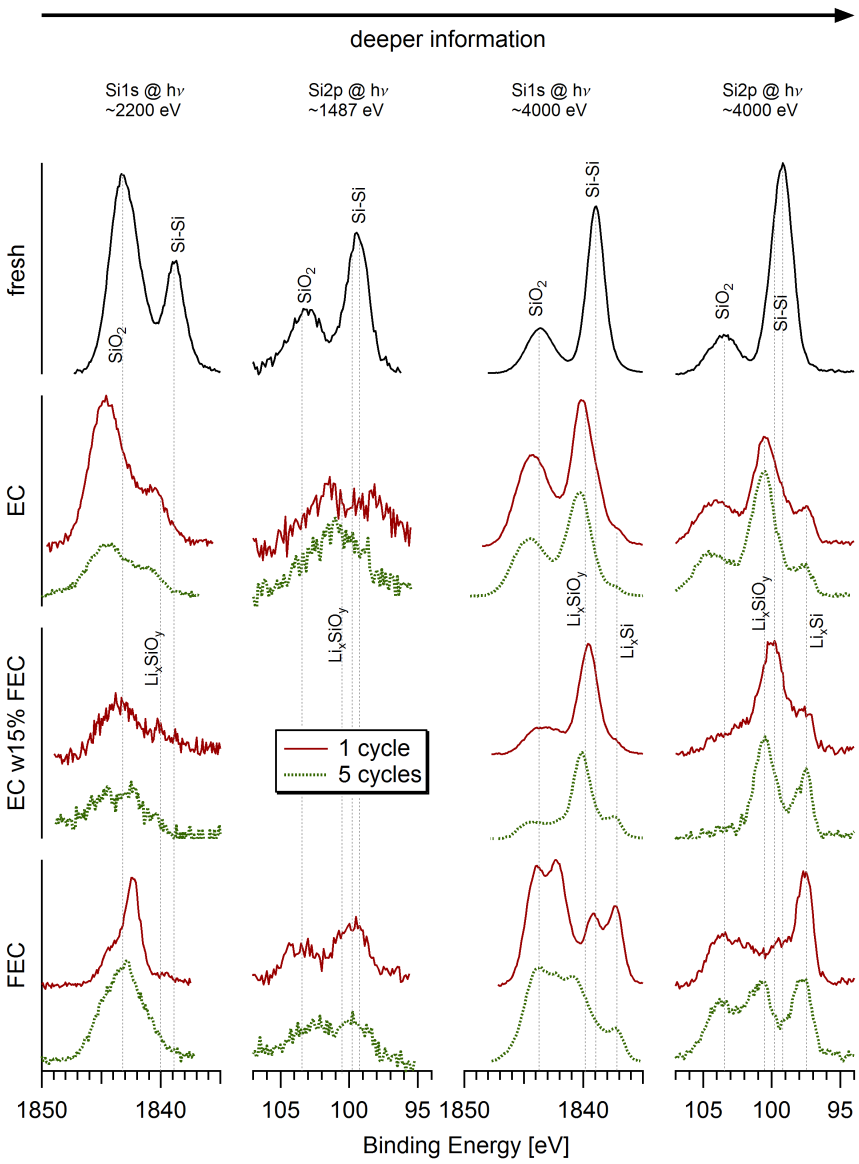

Figure 2-19: Silicon spectra of pristine BF-Si anodes (top row) and for first (red) and second (green) cycle anodes from coin cells fabricated with electrolyte solvent EC (2nd row), EC+15% FEC (3rd row), and FEC (bottom row).

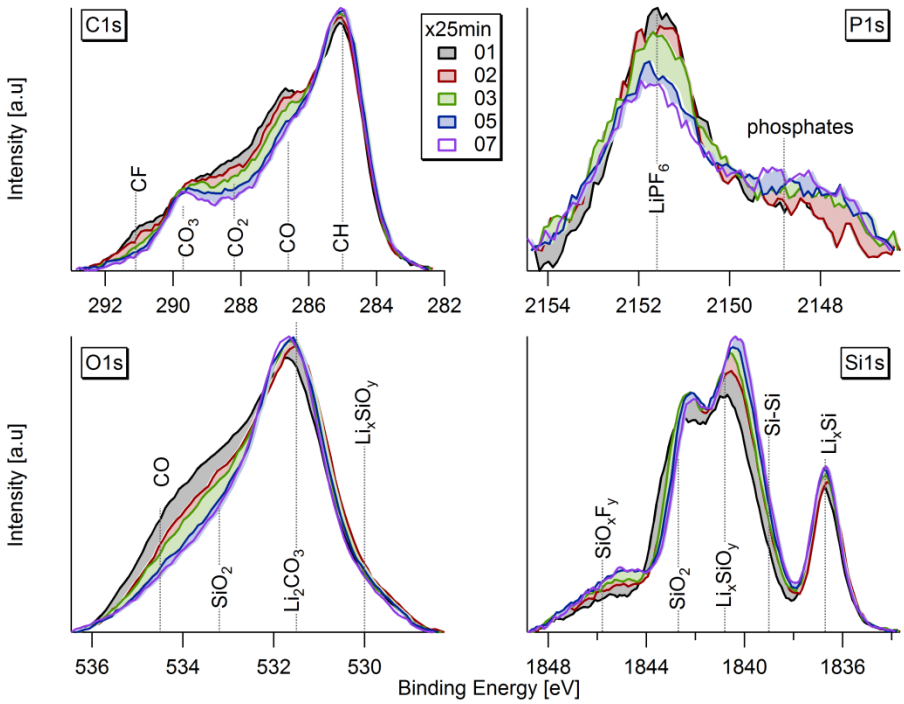

Figure 2-20: Individual 1s electron spectra for C, P, Si, O for BF-Si nanoparticle anode cycled 20 times with FEC solvent, collected in increments of 25 min.

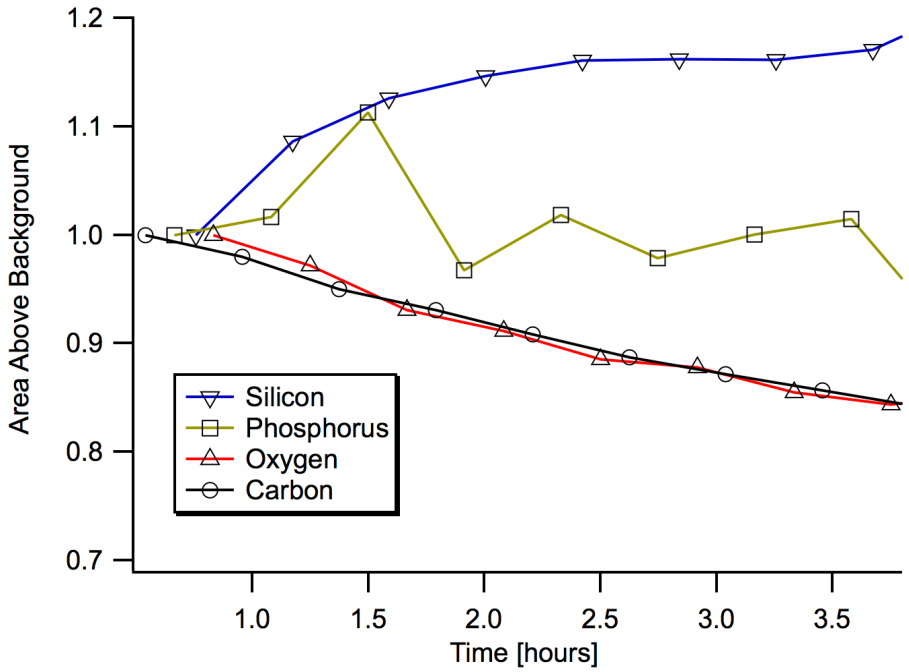

Figure 2-21: Total signal intensity vs. beam exposure time for the 1s electrons of Si, P, O, C, normalized to the initial intensity, from BF-Si nanoparticle battery anode cycled 20 times in FEC solvent.

2-10 Tables

Table 2-1: Atomic concentrations for EC samples

hv=1487 eV	Si	F	O	C
fresh	35.3%		45.7%	19.0%
EC-1c	8.3%	26.7%	33.4%	31.6%
EC-5c	4.6%	23.4%	35.9%	36.1%

hv=2200 eV	Si	F	O	C
fresh	42.13%		34.19%	23.68%
EC-1c	9.94%	13.02%	46.84%	30.20%
EC-5c	6.47%	13.56%	46.20%	33.77%

hv=4000 eV	Si	F	O	C
fresh	45.65%		38.21%	16.14%
EC-1c	7.39%	13.34%	52.78%	26.49%
EC-5c	7.60%	16.64%	50.39%	25.37%

Table 2-2: Atomic concentrations for EC+15%FEC samples

hv=2200 eV	Si	F	O	C
fresh	51.93%		28.20%	19.87%
EC+FEC-1c	3.19%	2.66%	54.12%	40.03%
EC+FEC-5c	1.95%	7.80%	44.68%	45.57%

hv=4000 eV	Si	F	O	C
fresh	55.42%		29.70%	14.88%
EC+FEC-1c	4.78%	3.16%	56.70%	35.35%
EC+FEC-5c	3.83%	8.56%	49.84%	37.78%

Table 2-3: Atomic concentrations for FEC samples

hv=1487 eV	Si	F	O	C
fresh	35.3%		45.7%	19.0%
FEC-1c	15.2%	23.4%	28.7%	32.7%
FEC-5c	6.5%	28.3%	29.7%	35.5%

hv=2200 eV	Si	F	O	C
fresh	42.13%		34.19%	23.68%
FEC-1c	4.91%	21.78%	37.29%	36.02%
FEC-5c	3.84%	20.17%	39.69%	36.30%

hv=4000 eV	Si	F	O	C
fresh	45.65%		38.21%	16.14%
FEC-1c	4.89%	25.47%	38.00%	31.64%
FEC-5c	3.83%	21.96%	42.83%	31.38%

MANUSCRIPT-III

To be submitted to Journal of the American Chemical Society

Role of Substrate Binders in Solid Electrolyte Interphase (SEI) Formation in Lithium Ion Batteries Studied With Hard X-Ray Photoelectron Spectroscopy (HAXPES)

Benjamin T. Young[1], David R. Heskett[1], Cao Cuong Nguyen[2], Anton Lobach[1], Brett L. Lucht[2], Joseph C. Woicik[3]

1) *Department of Physics, University of Rhode Island, Kingston RI*
2) *Department of Chemistry, University of Rhode Island, Kingston RI*
3) *National Institute of Standards and Technology, Gaithersburg MD*

Corresponding Author: Dr. David Heskett

Department of Physics

University of Rhode Island

East Hall, 2 Lippitt Rd.

Kingston, RI 02881, USA

Phone: 1-401-874-2076

Email: dheskett@uri.edu

CHAPTER 3

Role of Substrate Binders in Solid Electrolyte Interphase (SEI) Formation in Lithium Ion Batteries Studied With Hard X-Ray Photoelectron Spectroscopy (HAXPES)

Abstract

Half-cell lithium ion batteries (LIBs) featuring anodes of silicon, conductive carbon, and binder material were constructed with electrolyte containing 1.2M $LiPF_6$ salt dissolved in equal volumes of ethylene carbonate (EC) and diethyl carbonate (DEC). Binders used include polyvinylidene fluoride (PVDF), polyacrylic acid (PAA), sodium carboxymethyl cellulose (CMC), and a mixture of equal masses of PAA and CMC. Hard X-Ray Photoelectron Spectroscopy (HAXPES) was performed on these anodes when fresh, soaked for 24h in electrolyte, cycled 0.5 V, and cycled one full time to study how substrate binders affect the formation of the solid electrolyte interphase (SEI). Batteries cycled 5, 10, and 20 times were also analyzed to discern what changes to the SEI occur after initial formation. Our analysis of the SEIs from these batteries indicates little reaction between the binder and electrolyte upon soaking alone, and is mostly observed as creation of species with a C-O bond in the PVDF and CMC batteries. Upon cycling to 0.5 V, batteries with all binder compositions show changes in the spectra consistent with generation of Li_2CO_3 and LiF, as well as Na_2CO_3 for batteries containing CMC binder. After one full cycle, significant changes are observed in the silicon spectra for all batteries. A thick SEI develops and continues to grow for further cycling. Our estimates of the film thickness indicate that PAA develops the thinnest SEI layer, followed by CMC+PAA,

CMC, and PVDF in order of increasing layer thickness. Apart from the thickness, the SEI layers from batteries with all binders were largely similar in composition and appear to grow in a homogeneous manner.

3-1 Introduction

The desire to replace carbonaceous anodes in lithium ion batteries is being driven by the need for greater energy density in demanding applications such as electric vehicles. Silicon is a leading candidate because with a theoretical specific capacity of 3580 mAh/g, silicon can potentially store nearly ten times the amount of energy as the same mass of graphite [1]. The main impediment to successful deployment of silicon anodes is that holding and releasing so much more lithium results in volume fluctuations about thirty times greater than what graphite anodes experience during cycling. The volume fluctuations can destroy substrate material integrity and crack the SEI, rendering it ineffective as a passivation layer. Capacity fade and eventual battery failure result from the associated breaking of electrical contact within the anode and loss of lithium as new SEI material grows to protect newly exposed active material [2] [3].

Novel anode construction and electrolyte materials are two widely researched avenues to accommodate the silicon volume fluctuations either by mitigating the stresses within the anode or generating more effective SEI layers [4] [5] [6]. The silicon SEI composition is reportedly similar to the one grown on graphite, and its properties depend largely on the electrolyte material used [7] [8] [9] [10] [11] [12] [13]. In those studies it was also shown that the SEI grown on silicon anodes is not able to withstand the volume fluctuations associated with cycling. Clearly, attainment

of a stable, predictable SEI will be necessary in order to harness the great capacity increase silicon can offer; however, this task can be more easily achieved if the volume fluctuations or their effects can be lessened.

Increasing the surface area to volume ratio of the substrate material reduces the internal stress and strain placed on it during cycling, extending the battery lifetime into the hundreds of cycles range for particle sizes on the order of 100 nm [14] [15]. Furthermore, the use of binder material in electrode fabrication helps with adhesion of the material to itself and to the current collector, and can help to moderate the volume expansion of the substrate material with less damage to the SEI. Polyvinylidene Fluoride (PVDF) is a standard binder used in batteries with graphite and alloy anodes, but is not optimal in Si-based batteries presumably because its poor elastomeric properties fail to accommodate the volume change [16], and it only binds to silicon particles by weak van der Waals forces [17].

More variables than elastomeric properties contribute to a binder's effectiveness as sodium carboxymethyl cellulose (CMC), a brittle, stiff polymeric derivative of cellulose, has shown better cycling performance than PVDF in Si-based anodes [18]. Lestriez and coworkers have attributed increased efficiency of CMC to its extended conformation in solution which facilitates formation of a more homogeneous electrode, and have suggested enhanced cross-linking of CMC chains to explain performance gains of electrodes prepared at low pH [19]. CMC is also water-soluble, making it ideal for fabrication costs and environmental considerations.

Magasinski *et al.* have proposed that rigid structure and lack of interaction with the electrolyte solvent will be requirements for successful Si-based anode binders in a

recent study comparing PVDF, CMC, and polyacrylic acid (PAA) [17]. Like CMC, PAA as a binder enhances battery performance over PVDF. Unlike CMC, however, PAA has the benefit of being soluble in environmentally friendly organic solvents that can limit the amount of oxide developed on the Si particles during fabrication. In addition, its higher concentration of carboxylic groups allows effective control over the spacing between them by copolymerization with other monomers. Thus, PAA offers some ability to tune mechanical properties that are fixed with CMC.

This study utilizes Hard X-ray Photoelectron Spectroscopy (HAXPES) to obtain new information on the role these binders play in development and evolution of the SEI under similar conditions and preparation. High photon energies available from synchrotron radiation gives access to more tightly bound core electrons and imparts more energy to less tightly bound ones than traditional XPS studies. This enables characterization of the SEI layer at both shallower and deeper levels in the film than have previously been possible, and we are able to provide depth dependent information about SEI development and maturation.

3-2 Experimental

3-2.1 Preparation of Electrodes and Coin Cell Fabrication

The electrodes used in this study were prepared by mixing binder material (25% wt.) with silicon nanoparticles (~50 nm diameter, 50% wt.) and conductive carbon (25% wt.), then coating a slurry of this mixture with water on a copper foil current collector. The anodes were then vacuum-dried for 24 h at 120 °C. Half cells (CR2032) were fabricated with the anodes, a polypropylene separator, and lithium foil in a high purity Ar-filled glove box with H_2O content <0.1 ppm. Each coin cell

contained 30 μL of electrolyte composed of 1.2 M $LiPF_6$ salt in ethylene carbonate (EC) and diethyl carbonate (DEC) (1:1 v/v). Four types of anodes were fabricated, differing only by the type of binder material. They are PVDF, CMC, PAA, and a mixture of equal masses of PAA and CMC. Electrochemical cycling data was collected through 20 cycles, and batteries that had been cycled 1, 5, 10, and 20 times, as well as ones cycled to 0.5V, were disassembled for *ex situ* analysis. Also prepared for *ex situ* analysis were fresh anodes and anodes soaked for 24h in electrolyte.

3-2.2 HAXPES Experiments

All HAXPES experiments were conducted at the X-24A end station of the NIST beamline at the National Synchrotron Light Source, Brookhaven National Laboratory (Upton, NY) [20]. Synchrotron radiation from a bending magnet is delivered to a constant offset, double Si(111) crystal monochromator via a Ni-coated graphite spherical collimating mirror and vertical and horizontal apertures. Once monochromatized, the beam is focused by a Ni-coated quartz toroidal mirror. The beam spot size is determined just upstream from the analysis chamber by vertical and horizontal apertures. Oriented perpendicular to the beam in the experimental chamber is the entrance aperture of a 200mm hemispherical analyzer configured to analyze a 0.5 mm spot on the sample positioned in front of it in the analysis chamber. Samples were oriented at grazing incidence to the photon beam, with a takeoff angle toward the analyzer of 3° or 5° relative to the sample normal to maximize the photoelectron mean escape depth. Nominal photon energies and resolutions were determined by measuring the Ag 3d signal from a silver standard foil attached to the sample bar. Total resolution for the analyzer and beamline, established as the half-width of the

Fermi edge at the top of the valence band maximum, was measured to be 0.45 and 0.55 eV for excitation energies 2.2 and 4 keV, respectively.

To minimize exposure of the samples to atmosphere, we took the following precautions: anodes from batteries described above were affixed with conductive carbon dots to a custom stainless steel bar capable of holding 66, 1cm x 1cm electrodes in an argon glove box at URI. The bar was sealed in a custom vessel in the glove box before removing and transporting it to Brookhaven National Lab where it was placed in a glove bag that was sealed around the fast turnaround load lock port of the preparatory chamber at X-24A. A positive pressure of nitrogen was flown through the chamber and attached bag while the bar was removed from its container, installed on the chamber's 3-axis manipulator, and the load lock closed. After stopping the gas flow, the preparatory chamber was evacuated for 12 h by turbomolecular pumping before lowering the samples into the experimental chamber. Experimental chamber pressure was less than $5x10^{-9}$ Torr. The sample bar was electrically connected through the manipulator to a common ground with the analyzer, but no further attempt was made to correct for charging of the samples during measurements.

To minimize beam effects on the samples, a minimum number of spectra were collected in standardized order at a unique spot on each sample and a new spot was analyzed for each excitation energy. For this investigation we used photon energies of 2.2 and 5 keV. We collected spectra of Si 1s, F 1s, O 1s, C 1s, Si 2s, P 2p, Si 2p, and Li 1s electrons at both photon energies, and at 5 keV we also took spectra of the P 1s electron. All spectra were recorded with a dwell time of 100 ms and energy step of 100 meV, with the analyzer in transmission mode using a 0.3 mm wide entrance slit,

and with an analyzer pass energy of 500 eV except the Si 1s electron at 2.2 keV (pass energy 200 eV).

Spectra were analyzed with Wavemetrics' IGOR Pro software. All spectra were scaled by the number of scans taken to obtain comparable intensities between them before subtraction of a Shirley background [21]. Fits to the experimental data were performed using Voigt shapes, the parameters of which were constrained by the shape of the Ag standard peaks at each photon energy. Normalized signal intensities for each spectrum, I_i, were calculated using the formula:

$$I_i = \frac{A_i}{T(KE)_i \, \sigma(h\nu)_i \, \lambda(KE)_i} \quad (1)$$

where A corresponds to the background-subtracted spectrum area, T is the relative transmission function of the X-24A analyzer [22] as a function of the photoelectron kinetic energy, σ is the Scofield photoionization cross section [23] as a function of the photon energy, and λ is the inelastic mean free path of electrons in the material [24] as a function of photoelectron kinetic energy. After the intensities were normalized, we calculated atomic concentrations, C_i, using the formula:

$$C_i = \frac{I_i}{\sum_j I_j} \quad (2)$$

where the summation index, j, runs over all distinct elements in the sample. For elements where two or more cores were measured, we calculated concentrations using the ones available to Al-Kα XPS experiments performed at URI.

The SEI thickness may be approximated by assuming the SEI is a uniform layer of depth *d* which attenuates the signal from the anode, similar to the procedure outlined recently by Malmgren *et al.* [25] using the equation:

$$\frac{C_i}{C_f} = \frac{\int_d^\infty e^{-x/\lambda_p \, Sin\theta} dx}{\int_0^\infty e^{-x/\lambda_f \, Sin\theta} dx} = \frac{\lambda_p}{\lambda_f} e^{-d/\lambda_p \, Sin\theta} \quad (3)$$

This model assumes the sample below some depth *d* is homogeneously composed of *i* (Na or Si in this study). The variable C is defined in equation (2), and the ratio of the concentration C_i in a given sample to the concentration C_f in the fresh sample equates to an exponential which is readily solved for *d*. The mean free path of polyethylene was used for λ_p [24] and that of Na or Si was used for λ_f [26]. The angle between the analyzer line of sight and the sample normal defines θ. For analysis of the Si spectra, the concentration was restricted to include only the area of the elemental Si contribution to the spectra, as obtained through fits to the experimental data.

The kinetic energy scale used for data collection was converted to binding energy for display by referencing a fit to the C 1s spectrum in each set of spectra. For fresh samples, 284 eV was used as the binding energy reference for the amorphous graphite peak. This peak shifts after cycling begins, so we chose to reference binding energies from the more intense hydrocarbon contamination peak at binding energy 285 eV for all other samples. We also referenced to the C-O species' peak at binding energy 286.5 eV.

3-3 Results

3-3.1 Electrochemical Cycling

Electrochemical cycling results are displayed in Figure 3-22 and Figure 3-23 as plots of discharge capacity and efficiency, respectively, vs. cycle count. The PVDF battery is vastly outperformed by the others in the study, losing approximately 2/3 of its initial discharge capacity within ten charge/discharge cycles. For this reason, 20-cycle batteries using the PVDF binder were not pursued for *ex situ* analysis.

Performance for the CMC, PAA, and CMC with PAA (hereafter denoted as CMCPAA) batteries showed similar performance for both discharge capacity and efficiency. PAA batteries fared the best with CMCPAA performing almost identically except for a slightly faster capacity fade between 10 and 15 cycles. Batteries with CMC binder performed only slightly less well, showing additional capacity fade equal to about 250 mAh/g over the PAA and CMCPAA batteries which were very similar by 20 cycles. In terms of cycling efficiency, curves for all but the PVDF batteries flatten out by 20 cycles and differences are likely trivial within sample-to-sample variation.

3-3.2 HAXPES measurements

Phosphorus spectra from HAXPES measurements are displayed in Figure 3-24 and Figure 3-25 as plots of intensity vs. binding energy. Figure 3-24 shows SEI formation spectra for anodes that were soaked in the electrolyte, cycled to 0.5 V, and after one full cycle as stacked plots. Figure 3-25 shows cycling spectra for anodes that were cycled 1, 5, 10, and 20 times, except for the PVDF batteries which were not pursued beyond ten cycles because of extensive capacity fade by 10 cycles. The spectra are arranged in a grid by rows corresponding to binders and by columns with deeper information proceeding left to right. The P 1s core is available for measurement at 5 keV photon energy and provides information at an intermediate depth between the more surface sensitive measurement of the P 2p core at 2.2 keV and the deep P 2p measurement at 5 keV. Additionally, the increased cross section for the P 1s photoionization event provides much better signal-to-noise for the P 1s measurements relative to those of the P 2p at both photon energies.

The dominant feature of the phosphorus spectra is a peak at binding energy 134 eV in the P 2p and 2148 eV in the P 1s which we assign as phosphates. This peak is the only clear signal in the P 2p spectra of both Figure 3-24 and Figure 3-25 due to the low atomic concentration and associated poor signal-to-noise ratio. For the more surface sensitive P 1s column of cycling spectra in Figure 3-25, a weak peak attributed to unreacted $LiPF_6$ electrolyte salt at binding energy 2151.5 eV is visible for the 10-cycle batteries with all binders. For the batteries cycled 20 times, this peak increases in intensity relative to the phosphate peak.

The atomic concentrations calculated via equations (1) and (2) for phosphorus-containing species, relative to other elements present in the samples are reported in Table 3-4 through Table 3-11 and are all less than 2.5%. Such a small contribution from phosphorus likely puts observed variations within the calculation error, but there is a general trend of more relative phosphorus intensity in the SEI for the batteries displayed in Figure 3-24 (≤ 1 cycle) vs in Figure 3-25 (≥1 cycle). Atomic concentrations were calculated using the P 1s signal but did not vary significantly from those using the P 2p signal, so they have been omitted in the tables.

Silicon spectra are displayed for batteries cycled up to one time in Figure 3-26 and for further cycling in Figure 3-27. Information for the 1s and 2p core electrons for both photon energies used in this study are displayed in the figure with the shallowest (1s spectra taken at 2.2 keV) in the far left column and deeper measurements proceeding to the right. Shallower measurements for all fresh anodes exhibit two peaks indicating the presence of the native oxide layer encapsulating the Si nanoparticles (BE 1844 eV in 1s and BE 103.5 eV in 2p) and the more intense

elemental silicon signal (BE 1839 eV in 1s and BE 99.2, 99.8 eV in 2p). The Si 2p electron exhibits spin-orbit splitting, which is resolved for the elemental silicon peak in the 2.2 keV spectra, but not in the 2p spectra taken at 5 keV due to the smaller cross section for the 2p signal there and spectral broadening associated with the beamline optics. Proceeding to the right from all spectra in the left column, the ratio of oxide to elemental silicon peak intensity decreases as the signal displayed in the traces comes from, on average, deeper in the sample.

Differential charging effects are observed for all anode constructions for batteries cycled to 0.5V and one full cycle in Figure 3-26, and for all spectra displayed for further cycling in Figure 3-27. The differential charging of silicon-containing species is identified by apparent shifts of the representative peaks from their expected locations, shown as dashed vertical indicators in the figures, to lower binding energy locations. The effect is not apparent in the fresh or soaked samples, but the peaks begin to shift to lower binding energy with the 0.5V trace in each set of samples for all cores displayed in Figure 3-26. The effect seems stronger in the CMC spectra, with less of a shift seen in the CMCPAA and only a small shift for the PAA. By the one cycle spectra, all samples exhibit similar shifts, and there does not appear to be significant further shifting of the elemental silicon peak in the Figure 3-27 spectra for higher cycle counts.

The oxide peaks in Figure 3-26 spectra are similarly shifted, but for further cycling displayed in Figure 3-27 the behavior changes. Beginning with several fifth cycle spectra, the oxide peak exhibits a further shift to low binding energy while the elemental silicon peak remains relatively immobile. By 20 cycles in the Si 1s spectra

taken at 5 keV, the separations between the two peaks for PAA, CMCPAA, and CMC spectra are about 2 eV less than in the one-cycle spectra.

For the PVDF battery cycling spectra in Figure 3-27, there is a third peak developed in the Si 1s spectra taken at 5 keV that is not visible in the other columns of less well resolved spectra. The new peak, at 1 eV higher binding energy than the elemental silicon peak, is assigned as lithiated oxide species, Li_xSiO_y. Its intensity is slightly larger than the elemental peak in the 5-cycle spectra and the ratio increases for the 10-cycle battery. Between 5 and 10 cycles, the intensity of the oxide peak increases relative to the elemental signal as well.

Atomic concentrations reported in Tables 3-1 to 3-8 for silicon are slightly higher following the first cycle for batteries which contain CMC in the binder, though the progressions with cycle count are generally similar for the PAA, CMCPAA, and CMC batteries. The PVDF battery consistently has lower silicon concentration than the other batteries in the study. Estimates of SEI thickness from equation (3), derived from the Si 1s signal taken at 5 keV, are displayed graphically in the lower pane of Figure 3-38 as the estimated thickness of the SEI layer vs anode analyzed. The thickness of the PVDF battery SEI is estimated to be 43 nm at 10 cycles, while the other batteries studied had SEI layers of about 29 nm (or slightly less) at that point. Even after 20 cycles, the PAA, CMCPAA, and CMC batteries all had SEI thickness equal to 30.5 nm or less.

Spectra for the Na1s core are displayed in Figure 3-28 and Figure 3-29. There is no sodium in the batteries using PAA or PVDF as the binder, so only spectra for CMCPAA and CMC are displayed. The spectra in Figure 3-28 for one full cycle or

less are similar for both batteries and each exhibits a broad, single peak. The fresh spectra peaks are centered on 1072 eV binding energy and are likely convolutions of peaks representing NaOH and/or Na_2O (BE 1072.5 eV) with Na_2CO_3 (BE 1071.5 eV). Upon soaking for 24h in the electrolyte, the spectra for CMCPAA do not obviously change for either photon energy displayed while the peaks in the CMC spectra shift to higher binding energy, indicative of an increased relative concentration of the NaOH and/or Na_2O species. After the 0.5V cycle, the center intensity of all spectra shifts to lower binding energy, indicating increased concentrations of Na_2CO_3 and/or NaF. The center intensity of the peak does not shift for further cycling displayed in Figure 3-29. The intensity of the peak diminishes for higher cycle count and increases for higher photon energy, indicating the sodium in the binder remains localized deep in the sample for both binder formulations.

The atomic concentrations displayed in Tables 3-3 to 3-6 for these batteries should be viewed in the light that the binder in the CMCPAA battery is only half composed of CMC, so it isn't surprising that the fresh, soaked and 0.5V concentrations of Na in CMC are roughly double those of CMCPAA. It is surprising, however, that for 1 or more full cycles, the Na concentrations are roughly equivalent for both binder formulations. Estimates of SEI thickness derived from the Na1s signal observed at 5 keV displayed in Figure 3-38 (upper pane). The CMC estimate from Na1s roughly agrees with that derived from the Si 1s signal in the lower pane, while the estimate for CMCPAA is somewhat lower than its complimentary Si 1s information.

Fluorine spectra are reported in Figure 3-30 and Figure 3-31. The only fresh sample spectra displayed are for the PVDF battery, which has fluorinated binder

material visible as a single peak at BE 688 eV, which we assign as the C-F bond. Interaction with the electrolyte material upon soaking causes this peak to shift slightly, approximately 0.5 eV to higher binding energy for measurements taken at both photon energies. Atomic concentrations in Table 3-7 and Table 3-8 indicate the relative concentration of fluorine-containing species increases by almost 5% for the shallower 2.2 keV spectra and by less than 3% at the deeper 5 keV measurement after soaking. After the 0.5V cycle, a peak at BE 685 eV appears indicating the incorporation of LiF in the SEI. The peak intensity is roughly equivalent to that of the C-F signal at 2.2 keV, but it decreases relative to C-F at 5 keV consistent with the deeper measurement. For one full cycle, the spectra at 2.2 and 5 keV are very similar, though the atomic concentrations indicate a much lower relative concentration of fluorine in the sample. For further cycling in Figure 3-31, the intensity ratio of the broad C-F, P-F feature to that of the LiF peak decreases at both photon energies.

The atomic concentrations corresponding to spectra in Figure 3-9 for the other batteries (PAA, CMCPAA, and CMC) are similarly small and indicate less interaction between the anodes and the electrolyte material during soaking. Cycling generates a peak indicative of LiF at BE 685 eV and a very small signal detected at the higher energy P-F indicator. There is a significant reduction in the fluorine concentration at one cycle, and these concentrations stay relatively consistent for further cycling, except for an anomalously high concentration for the 5-cycle CMC battery. The spectra corresponding to these formulations in Figure 3-31 for cycling beyond the first cycle all consist of two peaks representing LiF and P-F species. There is consistently

less P-F, relative to the intensity of LiF, at the deeper measurement for each set of 2.2 and 5 keV spectra and more P-F, relative to the LiF, for higher cycle numbers.

The evolutions of oxygen-containing species displayed in Figure 3-32 and Figure 3-33 are similar for all anode formulations and all spectra consist of a single peak. SiO_2 with expected BE 532 eV is the dominant intensity contributing to the fresh and soaked spectra for anodes containing PAA, which have their center intensities between the displayed indicators for the C-O bond at BE 534.4 eV and the carbonates indicator at BE 531.7 eV. The fresh and soaked spectra for anodes containing CMC have their center intensities shifted slightly toward the higher binding energy indicator for C-O. Beginning with the 0.5 V cycle, the center intensity for all spectra shift abruptly to the carbonates indicator at BE 531.7 eV and do not shift away from this value for further cycling.

Figure 3-34 and Figure 3-35 show spectra for the C 1s electron. In Figure 3-34, the fresh and soaked spectra all consist of peaks at BE 284 eV representing the amorphous graphite signal, BE 285 eV representing the hydrocarbon contamination peak, and BE 286.5 and 289 eV representing C-O and C=O bonds, respectively. Upon cycling to 0.5 V, the graphite peak shifts to lower binding energy for all formulations and continues to shift further in that direction, to about 283 eV, for the one-cycle spectra. For further cycling in Figure 3-35, the graphite peak remains immobile, but decreases in intensity relative to the other species, consistent with a growing SEI. In each set of 2.2 and 5 keV spectra, this peak is less intense in the shallower 2.2 keV spectrum. Beginning with the first full cycle, a peak of significant intensity rises at BE 289.8 eV from the generation of sodium and/or lithium (alkyl) carbonates. This

peak is more intense, relative to the other peaks in the spectrum, for the deeper measurement in each photon energy pair. There is also a peak indicative of the PVDF binder at BE 291.1 eV in the fresh and soaked spectra for that battery, but its intensity is not clearly resolved for the 0.5 V cycle and beyond. A significant difference between the PVDF and CMC vs. the PAA and CMCPAA SEI layers is the increased intensity of the C-O feature after soaking in the electrolyte for 24h.

Spectra for Li 1s are displayed in Figure 3-36 and Figure 3-37. All lithium-containing species expected to be found in the SEI have similar binding energies, so the spectra all consist of single peaks except for the soaked, which do not exhibit intensity that is discernable from the background. Lithium signal is detected beginning with the 0.5V cycle and indicators on the plots describe expected binding energies of LiF (55.7 eV) and Li_2CO_3 (55.1 eV). The spectra are convolutions of peaks at these locations, and the center intensity of all 0.5 V spectra are shifted toward the high binding energy indicator for LiF. After one full cycle, and for further cycling in Figure 3-37, the center intensity of the peak shifts toward the indicator at 55.1 eV consistent with the generation of lithium (alkyl) carbonates. The atomic concentrations for lithium are generally in the range of 20-30% for cycling.

3-4 Discussion

Phosphorus concentrations for all batteries studied were below 2.5% for formation cycling and decreased to below 1% for five cycles and beyond. This may indicate that the small amount of phosphorus in the early SEI is sequestered near the interface of the SEI and substrate material. The observed signal in the HAXPES spectra for the P 1s measurement at 5 keV comes primarily from species with P-O or P=O bonds,

though all batteries show a small amount of unreacted $LiPF_6$ salt at 10 cycles. By 20 cycles, that peak grows in intensity relative to the P-O/P=O peak which may indicate impending stability of the SEI layer. Unreacted $LiPF_6$ salt being incorporated into the SEI with greater likelihood than further decomposition of the electrolyte material, which is responsible for the phosphate signal at higher binding energy [26], would explain this trend; however, strong conclusions from this observation are not possible because $LiPF_6$ is sensitive to the sample-to-sample washing (note the peak at BE 2152 eV in the P 1s spectrum for soaked CMC in Figure 3-24).

SEI thickness information is available in the silicon spectra by inspecting the relative intensities of peaks in the well-resolved Si 1s spectra taken at 5 keV. The ratio of the intensity of the oxide peak to that of the elemental silicon feature is related to the SEI film thickness and is smallest for PAA, larger for the mixed binder CMCPAA, and largest for CMC at 1, 10, and 20 cycles. At 5 cycles, CMC has the thickest SEI but the CMCPAA SEI is slightly thinner than that of the PAA battery. Except for the first cycle spectrum, where it has intermediate thickness between the PAA and CMCPAA batteries' SEIs, the SEI developed for the PVDF battery is consistently thicker than the other batteries. The addition of a third peak between those of the elemental silicon and its oxide in the PVDF spectra, which we have assigned as Li_xSiO_y, may be connected to the poor performance exhibited by the PVDF battery as displayed in the discharge capacity plot of Figure 3-22. None of the better performing batteries exhibit this lithium silicate species, however all batteries in our previous study concerning silicon nanoparticle anodes without binder material did and all exhibited dramatic capacity fade within 20 cycles [27]. Quantitative estimates

of the SEI thickness from application of equation (3) to the intensity of the elemental Si peak in the 5 keV Si 1s indicate the thickness of the SEI for PAA, CMCPAA, and CMC batteries to be similarly between 25-30 nm for 10 and 20 cycles with the largest thickness increase between the 0.5V cycle and one full cycle (10-15 nm growth).

These results are supported in part by the Na1s spectra and accompanying atomic concentrations in Tables 3-3 to 3-6. By the construction alone, if the SEIs were of similar composition and thickness for the CMC and CMCPAA batteries, we would expect that the sodium concentration to be roughly double that of the CMCPAA battery as it is in the atomic concentrations for less than one full cycle where the SEI is very thin. However, the atomic concentrations are comparable for cycled batteries, implying that the signal from the anode made with only CMC binder may be more thoroughly attenuated by a thicker SEI, which supports the analysis of the silicon spectra. This point is made more clearly in the upper pane of Figure 3-38, where the thickness of the CMCPAA SEI is nearly half that of the CMC battery.

Fluorine spectra indicate that the SEI is modified beyond 10 cycles for all batteries except the PVDF, which we did not analyze beyond 10 cycles. For all the anode constructions, cycling spectra indicate less LiF is incorporated in the SEI, relative to species with a P-F bond, for increasing cycle counts. Furthermore, there is consistently more LiF represented in the deeper measurement of each 2.2 and 5 keV set of spectra. This may suggest the LiF component of the SEI is deposited in greater amounts early on and found in greater concentrations nearer the interface of the SEI and the substrate than the surface.

The carbon spectra are similar for all batteries analyzed beyond one full cycle. A significant intensity of carbonate species, represented by a peak at 289.8 eV in the spectra, rises upon the first full cycle for all batteries and is more intense, relative to the other peaks, deeper in the sample. This behavior is seen consistently when comparing the 2.2 and 5 keV spectra for a given sample. Apart from the spectra corresponding to the PVDF battery, which have a higher concentration of carbonate and less C-O species than the PAA, CMCPAA, and CMC batteries, there is no obvious dependence of the C 1s spectra on the type of binder used in the anode fabrication.

The similarity of the oxygen spectra indicates oxygen-containing species are somewhat evenly distributed throughout the SEI. Atomic concentrations reported in Tables 3-1 to 3-8 are generally consistent as well, as are those for carbon.

3-5 Conclusions

Coin cell lithium-ion batteries using PAA, CMCPAA, CMC, and PVDF as binder material in anodes composed of silicon nanoparticles, carbon black, and binder in the ratio of 2:1:1 by weight with identical electrolyte formulations have been investigated. Electrochemical cycling data slightly favor the batteries which contain PAA in the binder and batteries containing CMC or PAA vastly outperform the batteries using PVDF.

Anodes from the batteries have been characterized by HAXPES, which provides a number of conclusions about the SEI composition and maturation during cycling. Comparing spectra taken from fresh electrodes that had not been exposed to electrolyte material to those from anodes soaked in the electrolyte for 24h reveals that

the CMC and PVDF binders interact with the electrolyte to form C-O containing species. We observed no other obvious interactions between the anodes and the electrolyte material.

Cycling the batteries to 0.5V generates a number of changes. LiF is deposited in all SEIs studied, presumably from decomposition of the electrolyte, and is visible as the single peak appearing in the F 1s spectra. Its generation is mirrored in the Li 1s spectra as well. The O 1s spectra, dominated by C-O species in the fresh and soaked spectra exhibit carbonates as the dominant feature after the 0.5V cycle. Carbonates become the dominant signal in Na1s spectra for the CMC and CMCPAA anodes as well. Carbonate signal intensity is observed for all batteries in the C 1s spectra, though it is not until the first full cycle that this signal is obvious relative to the other, more intense species. The further increase in carbonate species' intensities is seen after a full cycle, especially in the Li 1s spectra where the intensity of that signal shifts the single peak away from LiF to Li_2CO_3 for all batteries.

Spectra are mostly very similar for additional cycling beyond the first full cycle. A notable difference is the decreasing intensity of the Li_2CO_3 peak in the C 1s spectra relative to the other peak intensities and the slight consistent increase in this peak's intensity between the 2.2 and 5 keV spectra, which supports our previous finding that it is preferentially formed near the substrate active material [27]. The carbon, oxygen, and lithium spectra suggest that the SEI layers for these systems are similarly composed and do not vary much as the SEI grows. Given that these three elements routinely contribute 90-95% of the observed HAXPES signal, we conclude that the

SEIs deposited on the anodes are similar and grow in a rather homogeneous way after a large SEI thickness increase upon the first full cycle.

HAXPES measurements provide relative thickness estimates for the SEI layers and we find the thinnest SEI layer on the PAA anode, followed by layers of increasing thickness on CMCPAA, CMC, and PVDF binder anodes. Quantitative estimates of the SEI thickness based on a simple model indicate the layer for PAA, CMCPAA, and CMC batteries is less than 30 nm by 10 cycles and consistent through 20 cycles, while the PVDF SEI was greater than 40 nm by 10 cycles and still growing at that point.

3-6 Acknowledgements

Use of the National Synchrotron Light Source, Brookhaven National Laboratory, was supported by the U.S. Department of Energy, Office of Science, Office of Basic Energy Sciences, under Contract No. DE-AC02-98CH10886. We gratefully acknowledge funding from Department of Energy, Office of Basic Energy Sciences, EPSCoR Implementation award (DE-SC0007074). Additional support was provided by the National Institute of Standards and Technology.

3-7 References

[1] M. N. Obrovac and I. Christensen, "Structural Changes in Silicon Anodes During Lithium Insertion/Extraction," *Electrochemical Solid State Letters,* vol. 7, pp. A93-A96, 2004.

[2] M. J. Chon, V. A. Sethuraman, A. McCormick, V. Srinivasan and P. R. Guduru, "Real-Time Measurement of Stress and Damage Evolution During Initial Lithiation of Crystalline Silicon," *Physical Review Letters,* vol. 107, p. 045503, 2011.

[3] R. Benedek and M. M. Thackeray, "Lithium Reactions with Intermetallic-Compound Electrodes," *Journal of Power Sources,* vol. 110, pp. 406-411, 2002.

[4] Y. R. Ren, J. N. Ding, N. Y. Yuan, S. Y. Jia, M. Z. Qu and Z. L. Yu, "Preparation and Characterization of Silicon Monoxide/Graphite/Carbon Nanotubes Composite as Anode for Lithium-Ion Batteries," *J. Solid State Electrochem.,* vol. 16, pp. 1453-1460, 2012.

[5] H. Wu and Y. Cui, "Designing Nanostructured Si Anodes for High Energy Lithium Ion Batteries," *Nano Today,* vol. 7, pp. 414-429, 2012.

[6] H. C. Shin and M. Liu, "Copper Foam Structures with Highly Porous Nanostructured Walls," *Chem. Mater.,* vol. 16, pp. 5460-5464, 2004.

[7] M. Nie, D. P. Abraham, Y. Chen, A. Bose and B. L. Lucht, "Silicon Solid Electrolyte Interphase (SEI) of Lithium Ion Battery Characterized by Microscopy and Spectroscopy," *J. Phys. Chem. C,* vol. 117, pp. 13403-13412, 2013.

[8] S. Y. Li, X. L. Xu, X. M. Shi, B. C. Li, Y. Y. Zhao, H. M. Zhang, Y. L. Li, W. Zhao, X. L. Cui and L. P. Mao, "Composition Analysis of the Solid Electrolyte Interphase Film on Carbon Electrode of Lithium-Ion Battery Based on Lithium Difluoro (Oxalate) Borate and Sulfolane," *J. Power Sources,* vol. 217, pp. 503-508, 2012.

[9] K. Xu, "Nonaqueous Liquid Electrolytes for Lithium-Based Rechargeable Batteries," *Chem. Rev.,* vol. 104, pp. 4303-4318, 2004.

[10] B. Philippe, R. Dedryvère, M. Gorgoi, H. Rensmo, D. Gonbeau and K. Edström, "Role of the $LiPF_6$ Salt for the Long-Term Stability of Silicon Electrodes in Li-Ion Batteries − a Photoelectron Spectroscopy Study," *Chem. Mater.,* vol. 25, pp.

394-404, 2013.

[11] B. Philippe, R. Dedryvère, J. Allouche, F. Lindgren, M. Gorgoi, H. Rensmo, D. Gonbeau and K. Edström, "Nanosilicon Electrodes for Lithium-Ion Batteries: Interfacial Mechanisms Studied by Hard and Soft X-Ray Photoelectron Spectroscopy," *Chem. Mater.,* vol. 24, pp. 1107-1115, 2012.

[12] S. H. Kang, D. P. Abraham, A. Xiao and B. L. Lucht, "Investigating the Solid Electrolyte Interphase Using Binder-Free Graphite Electrodes," *J. Power Sources,* vol. 175, pp. 526-532, 2008.

[13] A. Xiao, L. Yang, B. L. Lucht, S. H. Kang and D. P. Abraham, "Examining the Solid Electrolyte Interphase on Binder-Free Graphite Electrodes," *J. Electrochem. Soc.,* vol. 156, pp. A318-A327, 2009.

[14] J. Yang, M. Winter and J. Besenhard, "Small particle size multiphase Li-alloy anodes for lithium-ion batteries," *Solid State Ionics,* vol. 90, pp. 281-287, 1996.

[15] C. Chan, H. Peng, G. Liu, K. Mcilwrath, X. Zhang, R. Huggins and Y. Cui, "High-performance lithium battery anodes using silicon nanowires," *Nature Nanotechnology,* vol. 3, no. 1, pp. 31-35, 2008.

[16] W. Zhang, "A review of the electrochemical performance of alloy anodes for lithium-ion batteries," *Journal of Power Sources,* vol. 196, pp. 13-24, 2011.

[17] A. Magasinski, B. Zdyrko, I. Kovalenko, B. Hertzberg, R. Burtovyy, C. Huebner, T. Fuller, I. Luzinov and G. Yushin, "Toward Efficient Binders for Li-Ion Battery Si-Based Anodes: Polyacrylic Acid," *ACS Applied Materials and Interfaces,* vol. 2, no. 11, pp. 3004-3010, 2010.

[18] N. Ding, J. Xu, Y. Yao, G. Wegner, I. Lieberwirth and C. Chen, "Improvement of cyclability of Si as anode for Li-ion batteries," *Journal of Power Sources,* vol. 192, no. 2, pp. 644-651, 2009.

[19] B. Lestriez, S. Bahri, I. Sandu, L. Roue and D. Guyomard, "On the binding mechanism of CMC in Si negative electrodes for Li-ion batteries," *Electrochemistry Communications,* vol. 9, pp. 2801-2806, 2007.

[20] C. Weiland, A. K. Rumaiz, P. Lysaght, B. Karlin, J. C. Woicik and D. Fischer, "NIST high throughput variable kinetic energy hard X-ray photoelectron spectroscopy facility," *J. Electron Spectrosc. Relat. Phenom.,* vol. 190, pp. 193-

200, 2013.

[21] D. A. Shirley, "High Resolution X-Ray Photoemission Spectrum of the Valence Bands of Gold," *Phys. Rev. B.,* vol. 5, pp. 4709-4714, 1972.

[22] C. Weiland, R. Browning, B. A. Karlin, D. A. Fischer and J. C. Woicik, "Note: Alignment/focus dependent core-line sensitivity for quantitative chemical analysis in hard x-ray photoelectron spectroscopy using a hemispherical electron analyzer," *Rev. Sci. Instrum.,* vol. 84, p. 036106, 2013.

[23] J. H. Scofield, "Theoretical Photoionization Cross Sections From 1 to 1500 keV," Lawrence Livermore Laboratory, Livermore, 1973.

[24] L. R. Painter, E. T. Arakawa, M. W. Williams and J. C. Ashley, "Optical Properties of Polyethylene: Measurement and Applications," *Radiation Reseach,* vol. 83, no. 1, pp. 1-18, 1980.

[25] S. Malmgren, K. Ciosek, M. Hahlin, T. Gustafsson, M. Gorgoi, H. Rensmo and K. Edström, "Comparing anode and cathode electrode/electrolyte interface composition and morphology using soft and hard x-ray photoelectron spectroscopy," *Electrochimica Acta,* vol. 97, pp. 23-32, 2013.

[26] C. L. Campion, W. Li and B. L. Lucht, "Thermal Decomposition of $LiPF_6$- Based Electrolytes for Lithium-Ion Batteries," *J. Electrochem. Soc.,* vol. 152, no. 12, pp. A2327-A2334, 2005.

[27] B. Young, D. Heskett, M. Nie, C. Nguyen, B. Lucht and J. Woicik, "Hard X-Ray Photoelectron Spectroscopy (HAXPES) Investigation of the Silicon Solid Electrolyte Interphase (SEI) in Lithium-Ion Batteries," *to be published.*

3-8 Figures

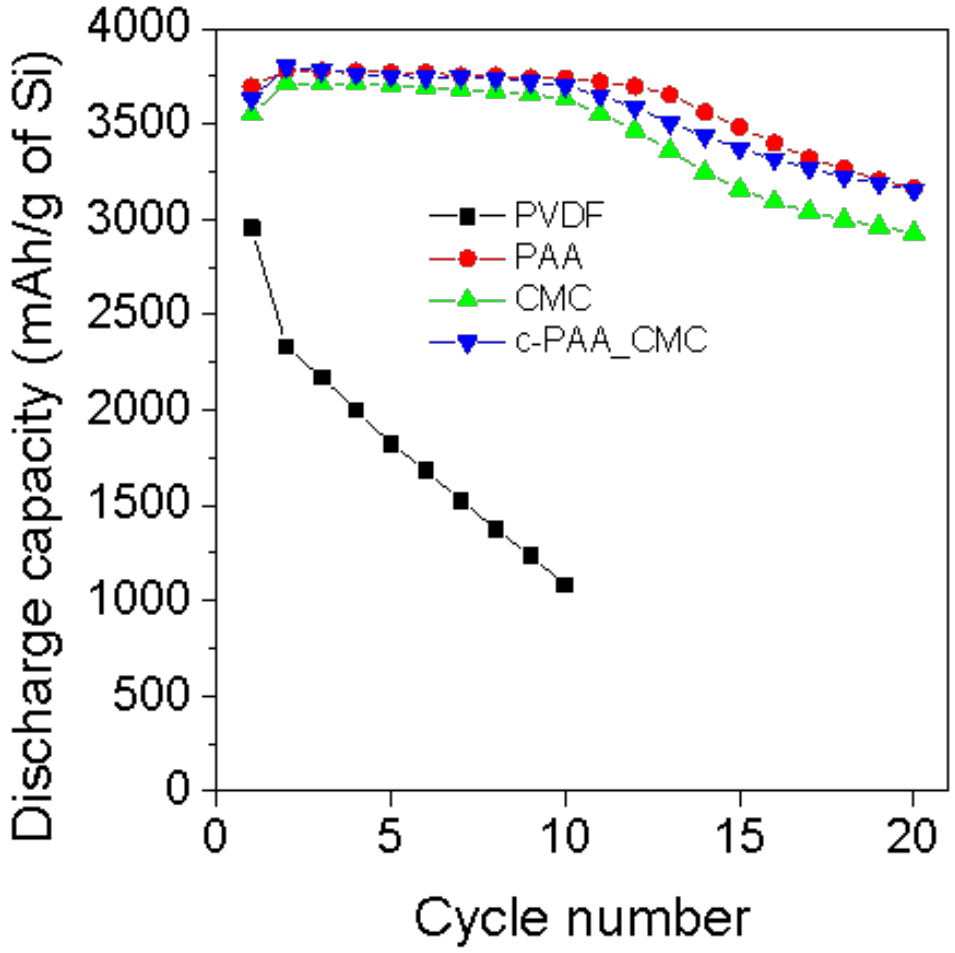

Figure 3-22: Plots of discharge capacity vs. cycle number for batteries with anode binders PVDF (black squares), PAA (red dots), CMC (green triangles), and CMC with PAA (blue triangles).

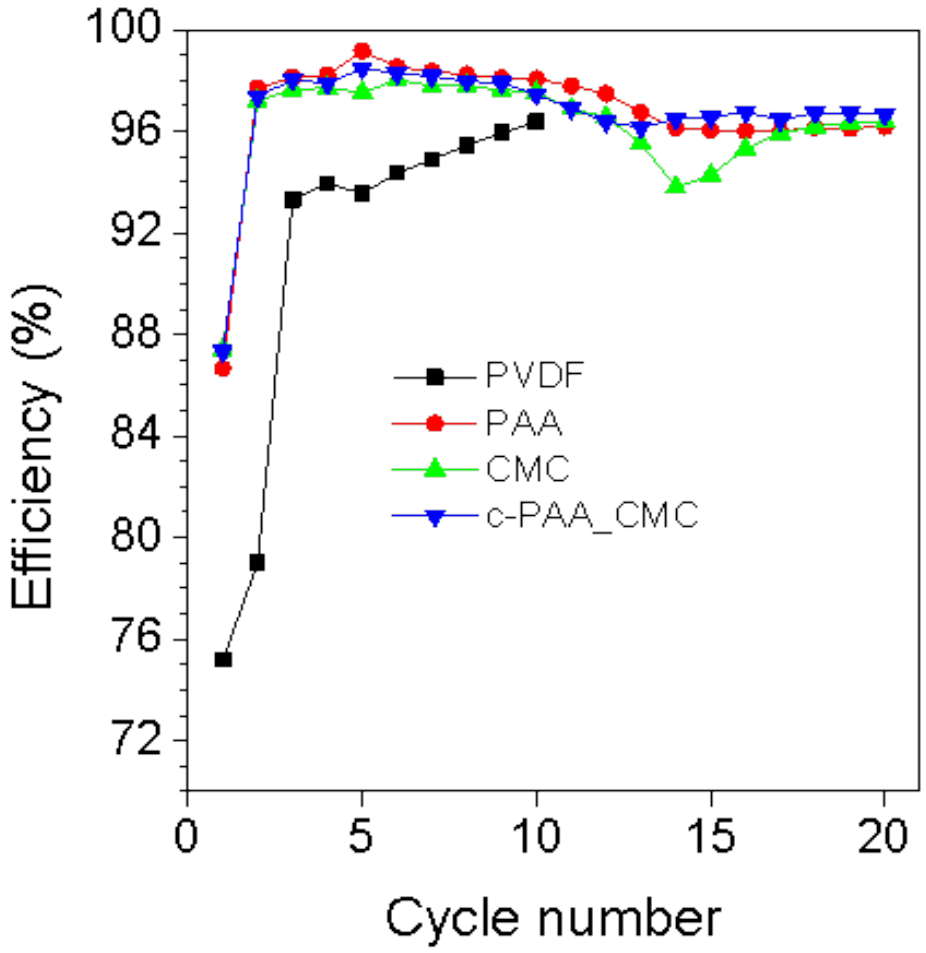

Figure 3-23: Plots of efficiency vs. cycle number for batteries with anode binders PVDF (black squares), PAA (red dots), CMC (green triangles), and CMC with PAA (blue triangles).

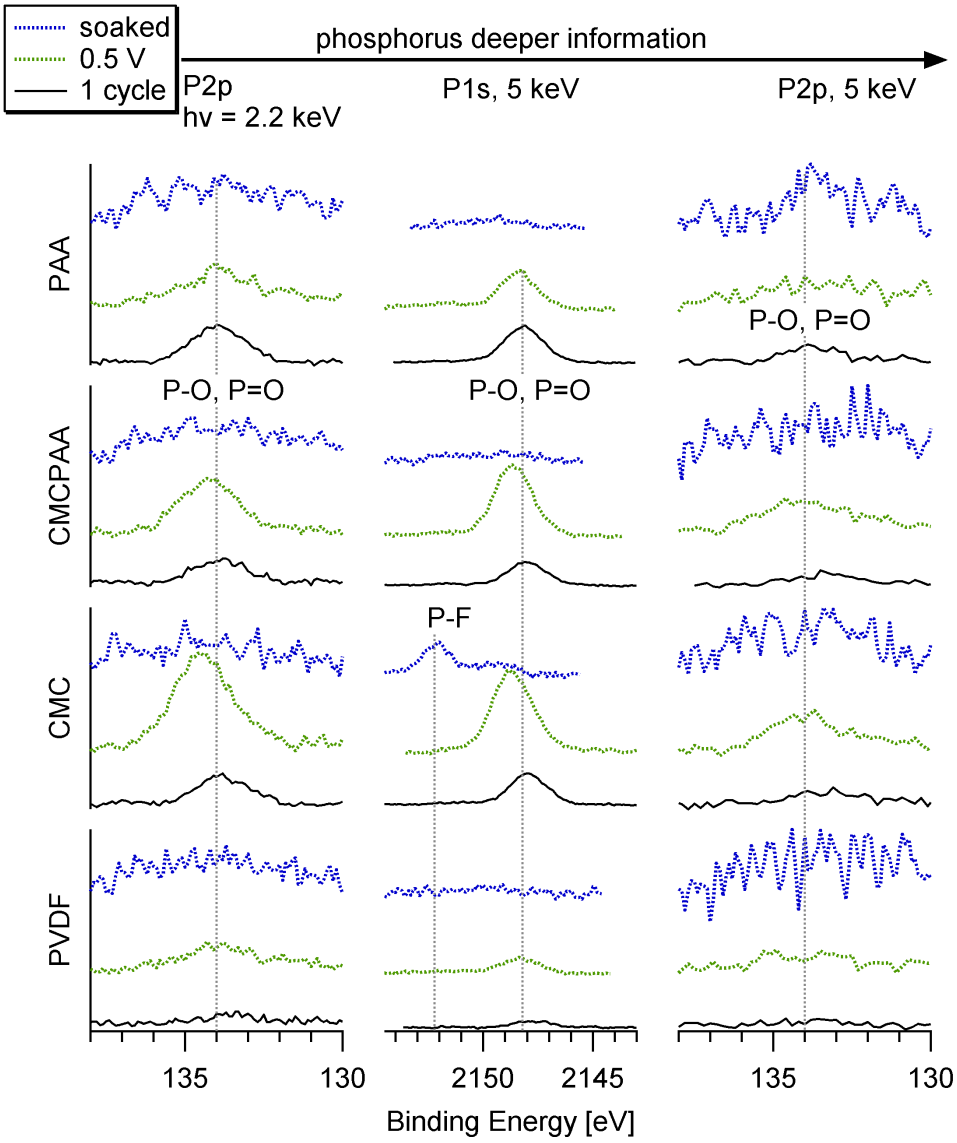

Figure 3-24: Phosphorus spectra for anodes: soaked (blue dots), half-cycle (green dots), and one cycle (black).

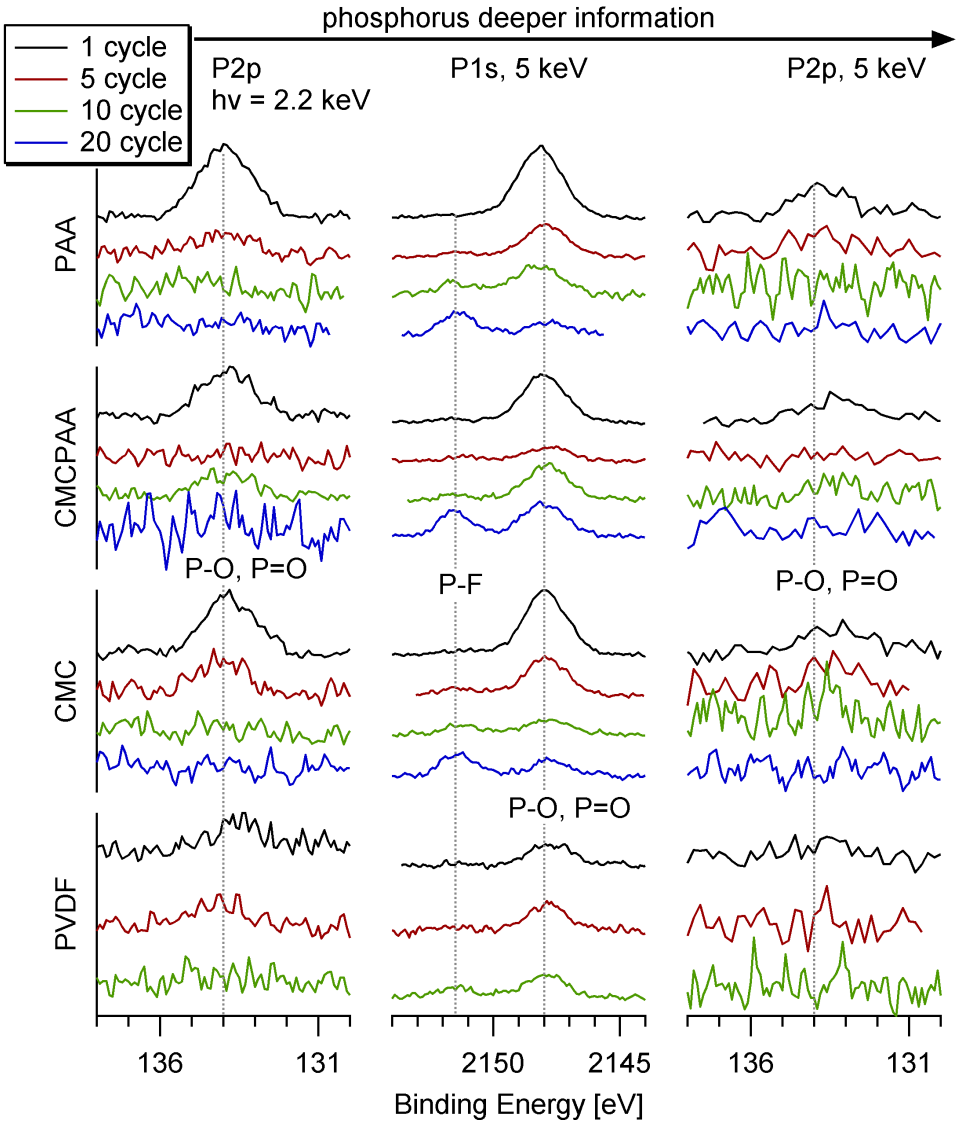

Figure 3-25: Phosphorus spectra for batteries cycled one (black), five (red), ten (green), and 20 (blue) times.

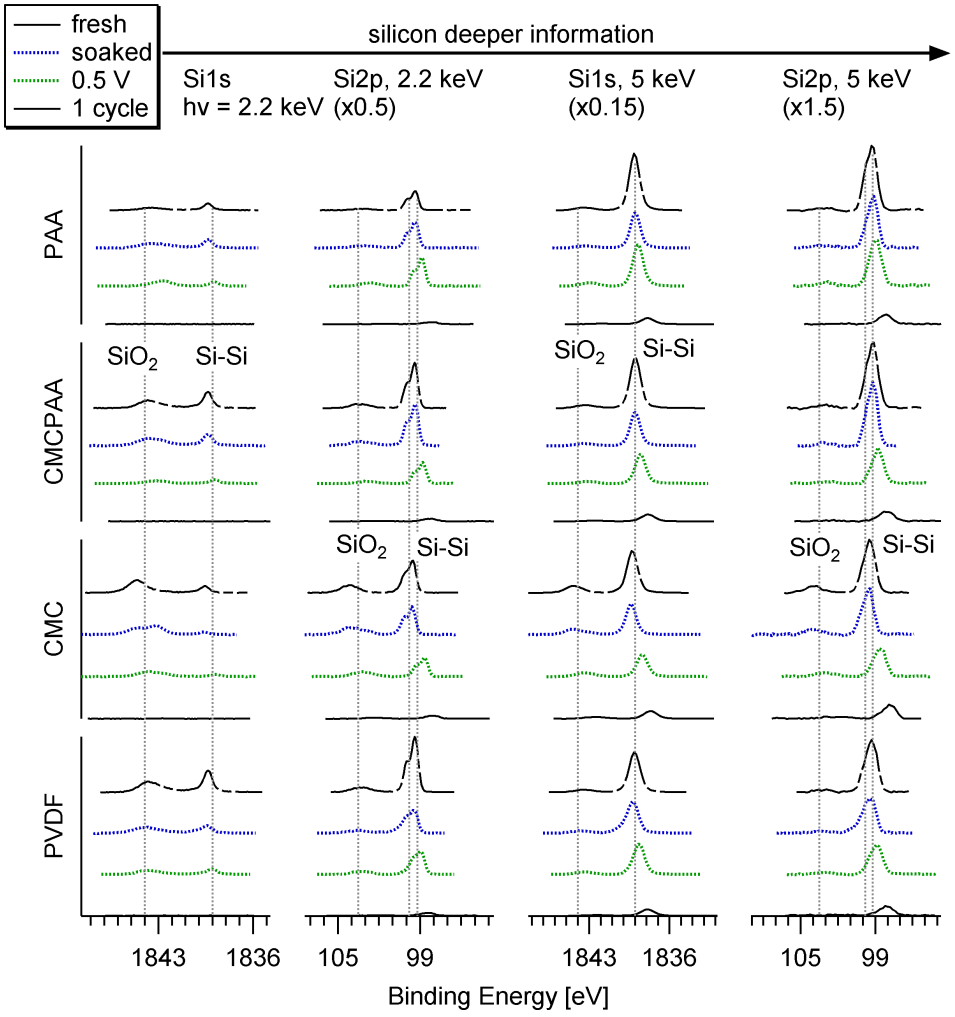

Figure 3-26: Silicon spectra for anodes: fresh (black, dot dash), soaked (blue dots), half-cycle (green dots), and one cycle (black).

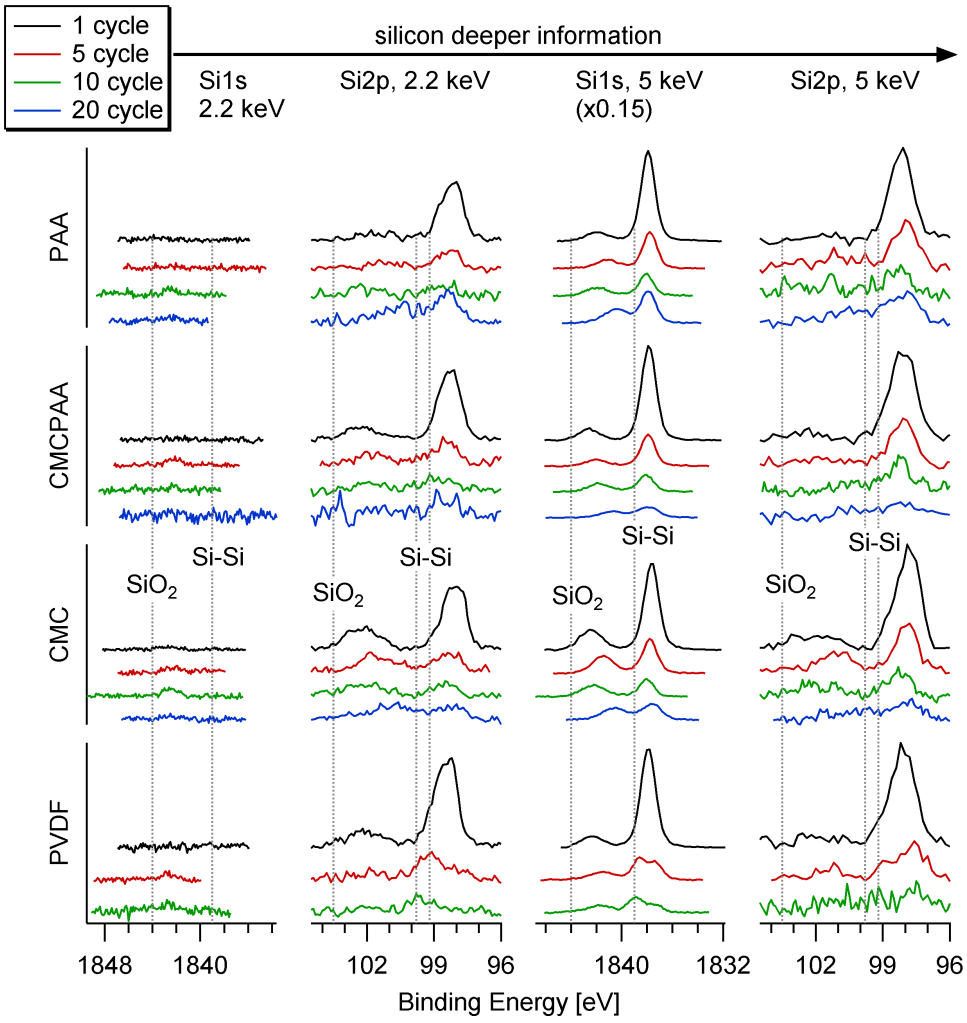

Figure 3-27: Silicon spectra for batteries cycled one (black), five (red), ten (green), and 20 (blue) times.

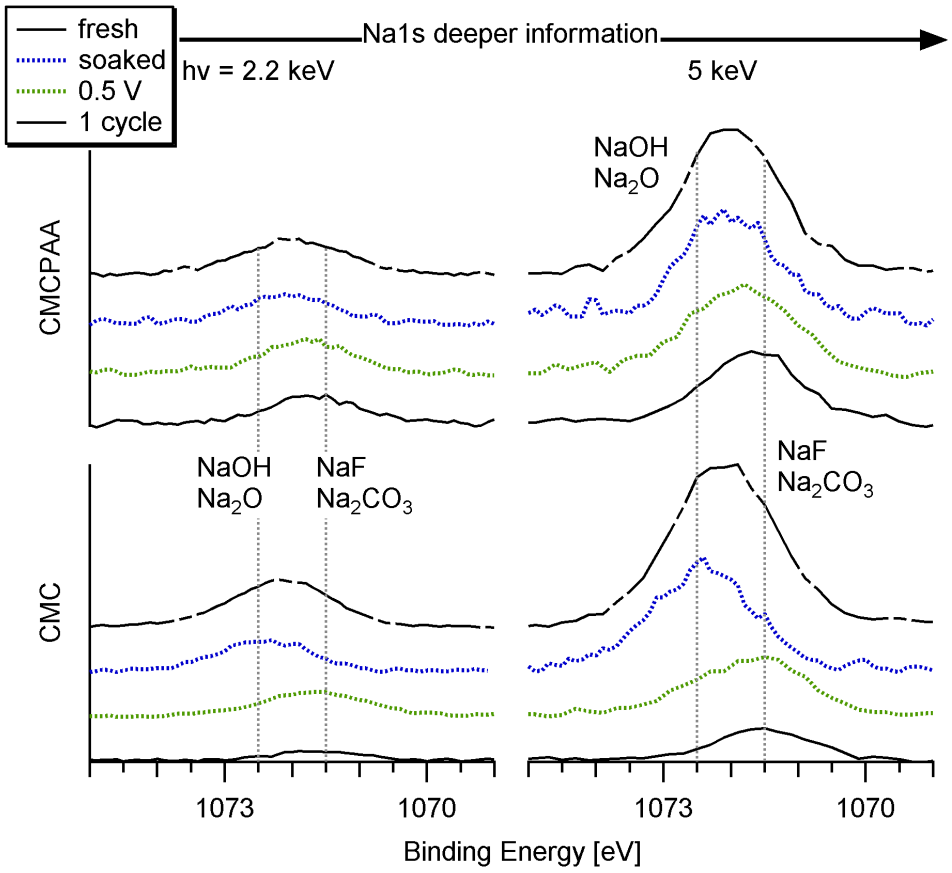

Figure 3-28: Na1s spectra for anodes: fresh (black, dot dash), soaked (blue dots), half-cycle (green dots), and one cycle (black).

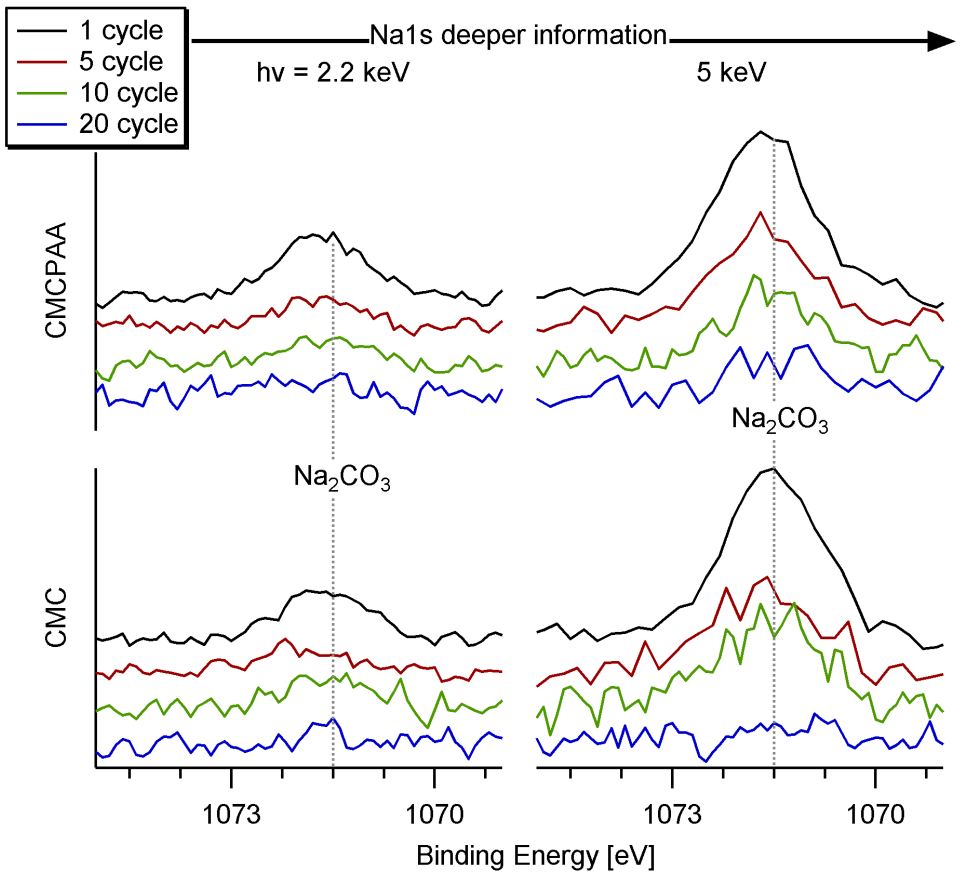

Figure 3-29: Na1s spectra for batteries cycled one (black), five (red), ten (green), and 20 (blue) times.

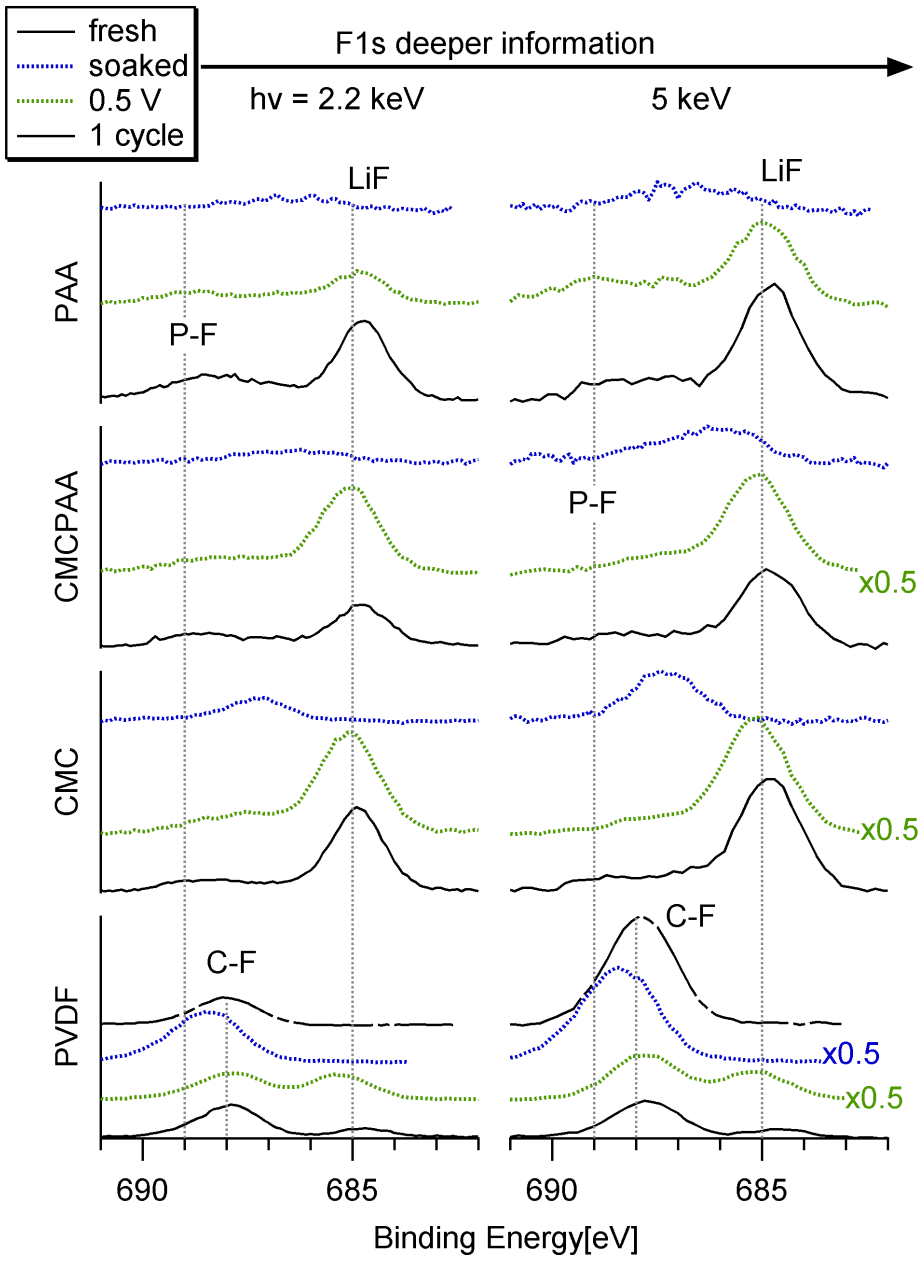

Figure 3-30: F 1s spectra for anodes: fresh (black, dot dash), soaked (blue dots), half-cycle (green dots), and one cycle (black).

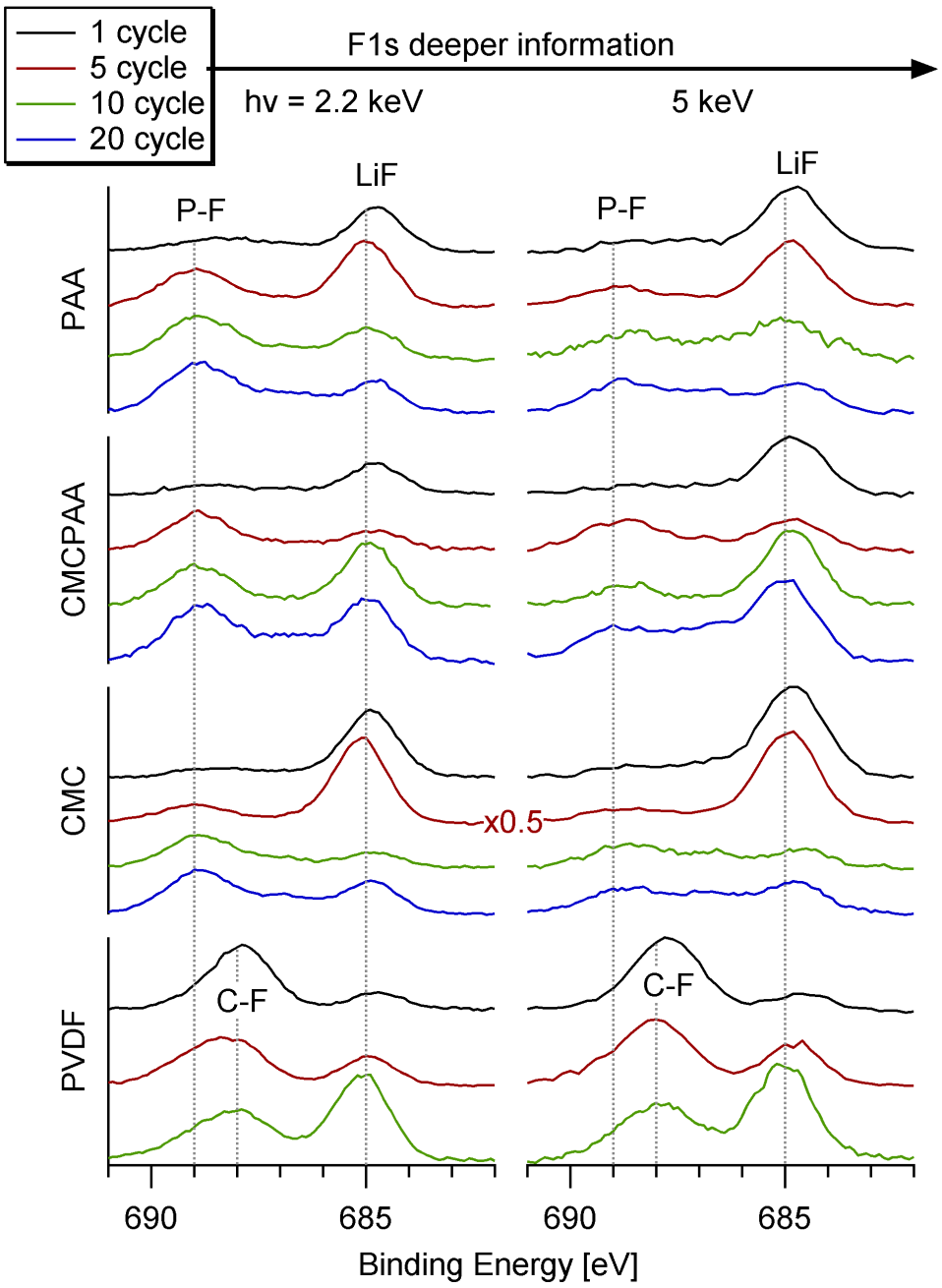

Figure 3-31: F 1s spectra for batteries cycled one (black), five (red), ten (green), and 20 (blue) times.

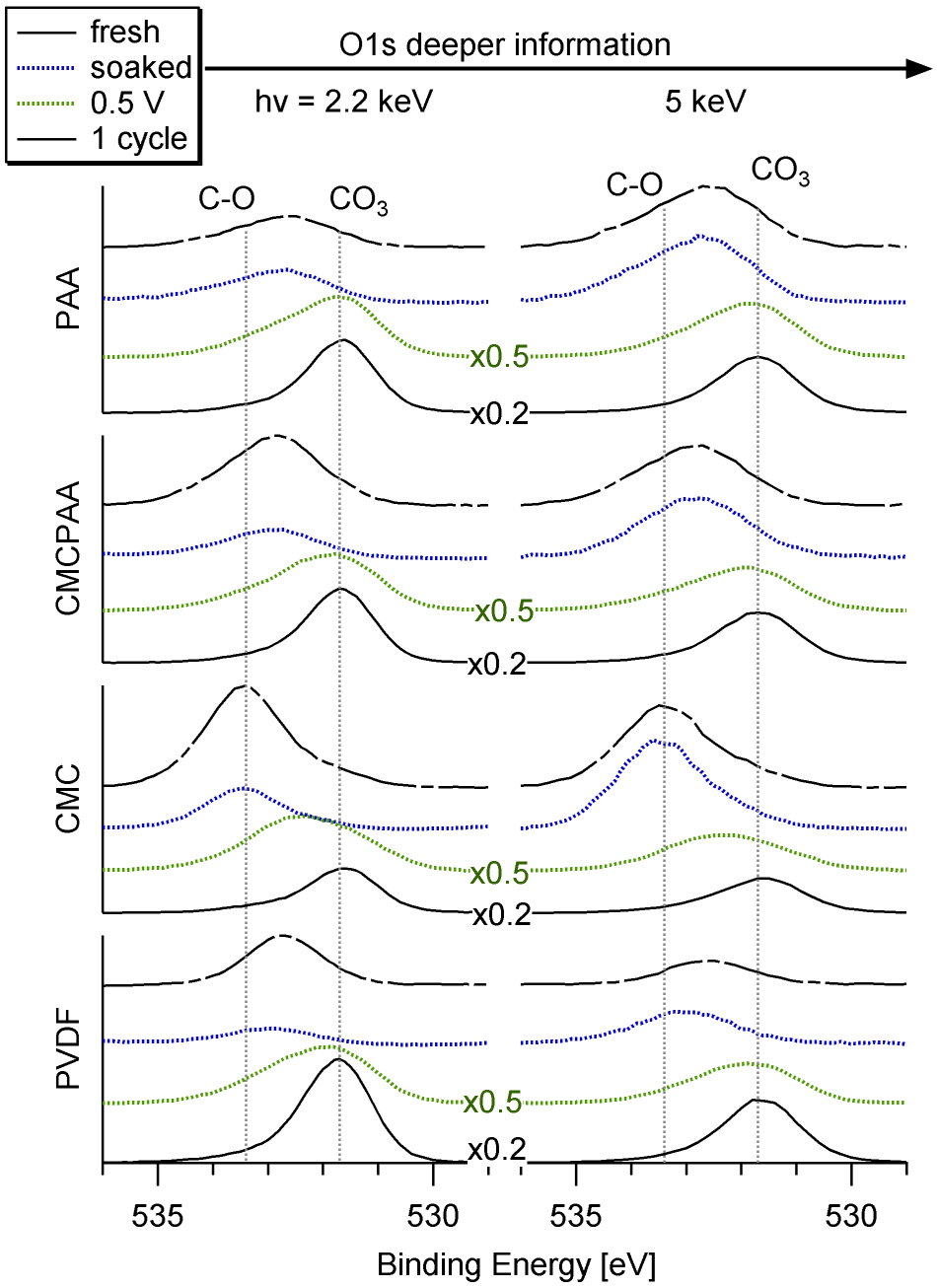

Figure 3-32: O 1s spectra for anodes: fresh (black, dot dash), soaked (blue dots), half-cycle (green dots), and one cycle (black).

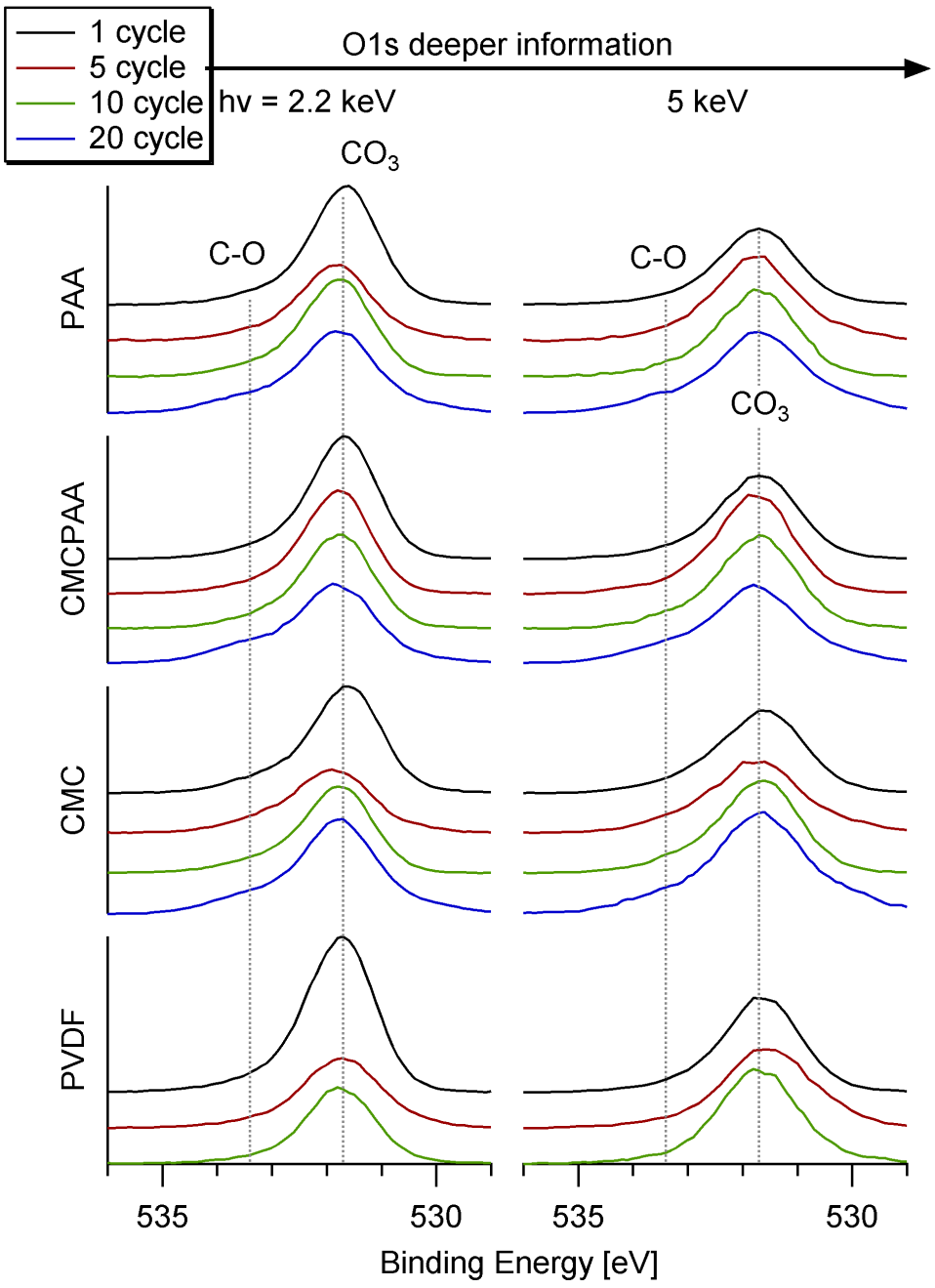

Figure 3-33: O 1s spectra for batteries cycled one (black), five (red), ten (green), and 20 (blue) times.

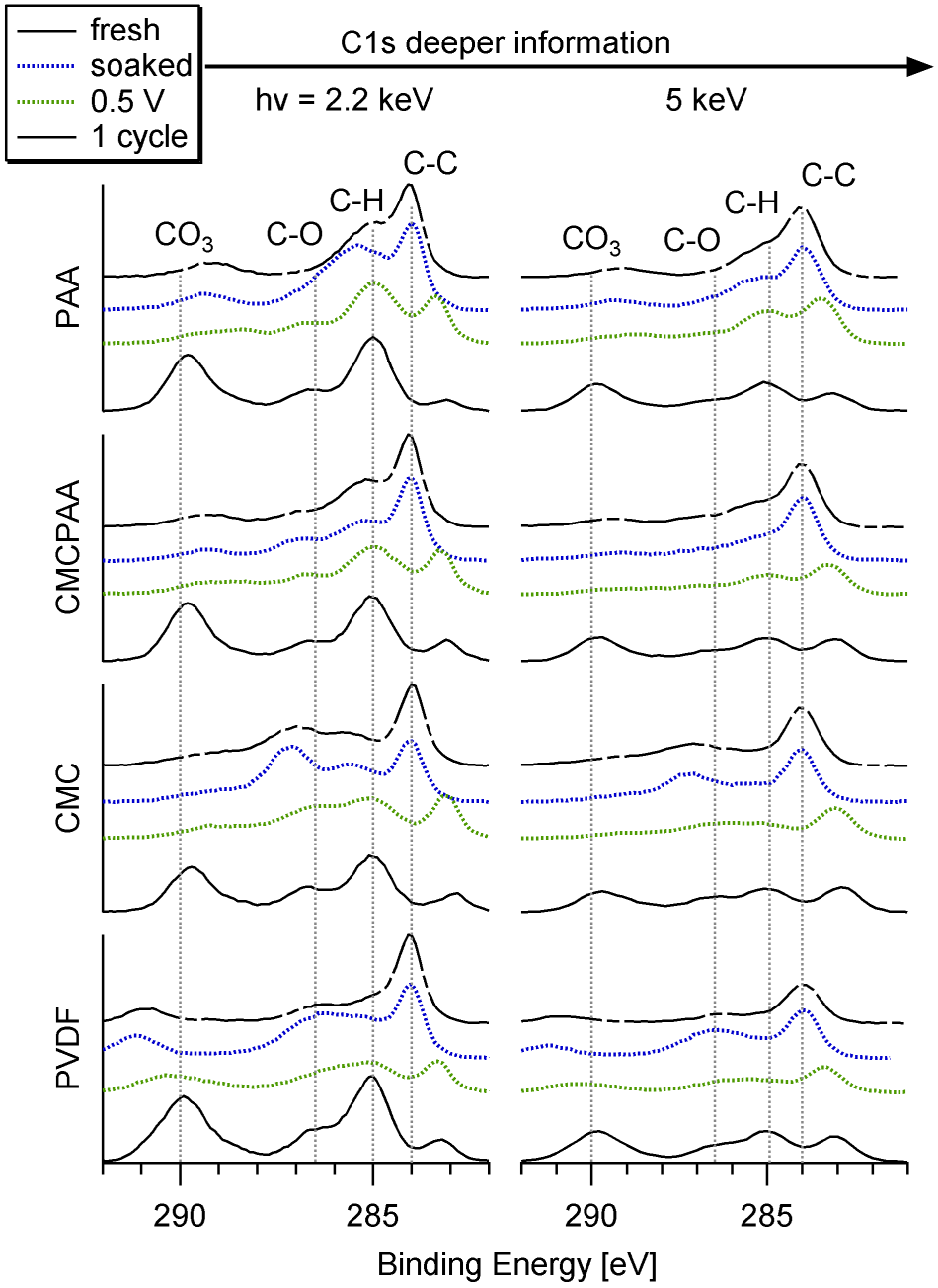

Figure 3-34: C 1s spectra for anodes: fresh (black, dot dash), soaked (blue dots), half-cycle (green dots), and one cycle (black).

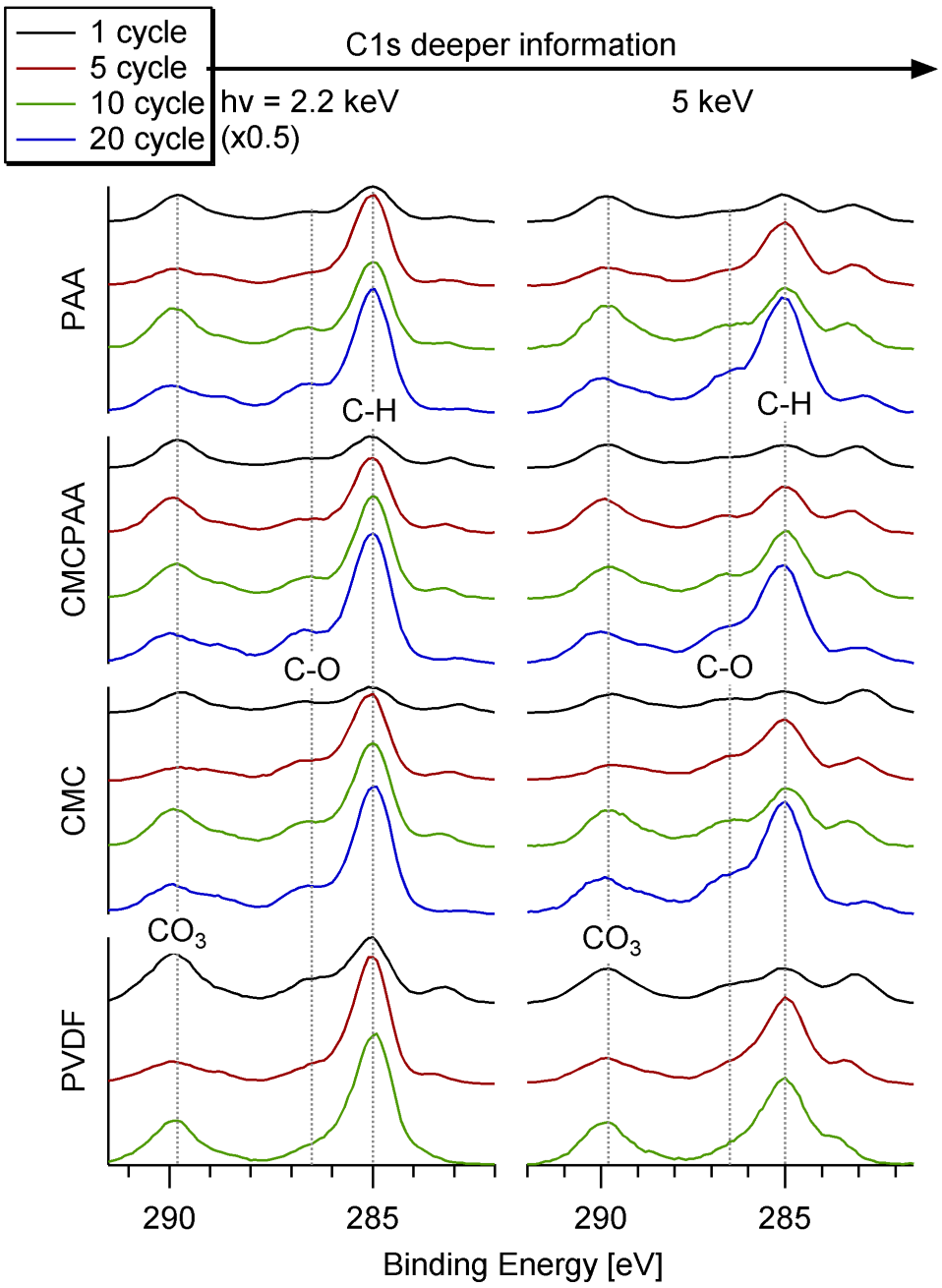

Figure 3-35: C 1s spectra for batteries cycled one (black), five (red), ten (green), and 20 (blue) times.

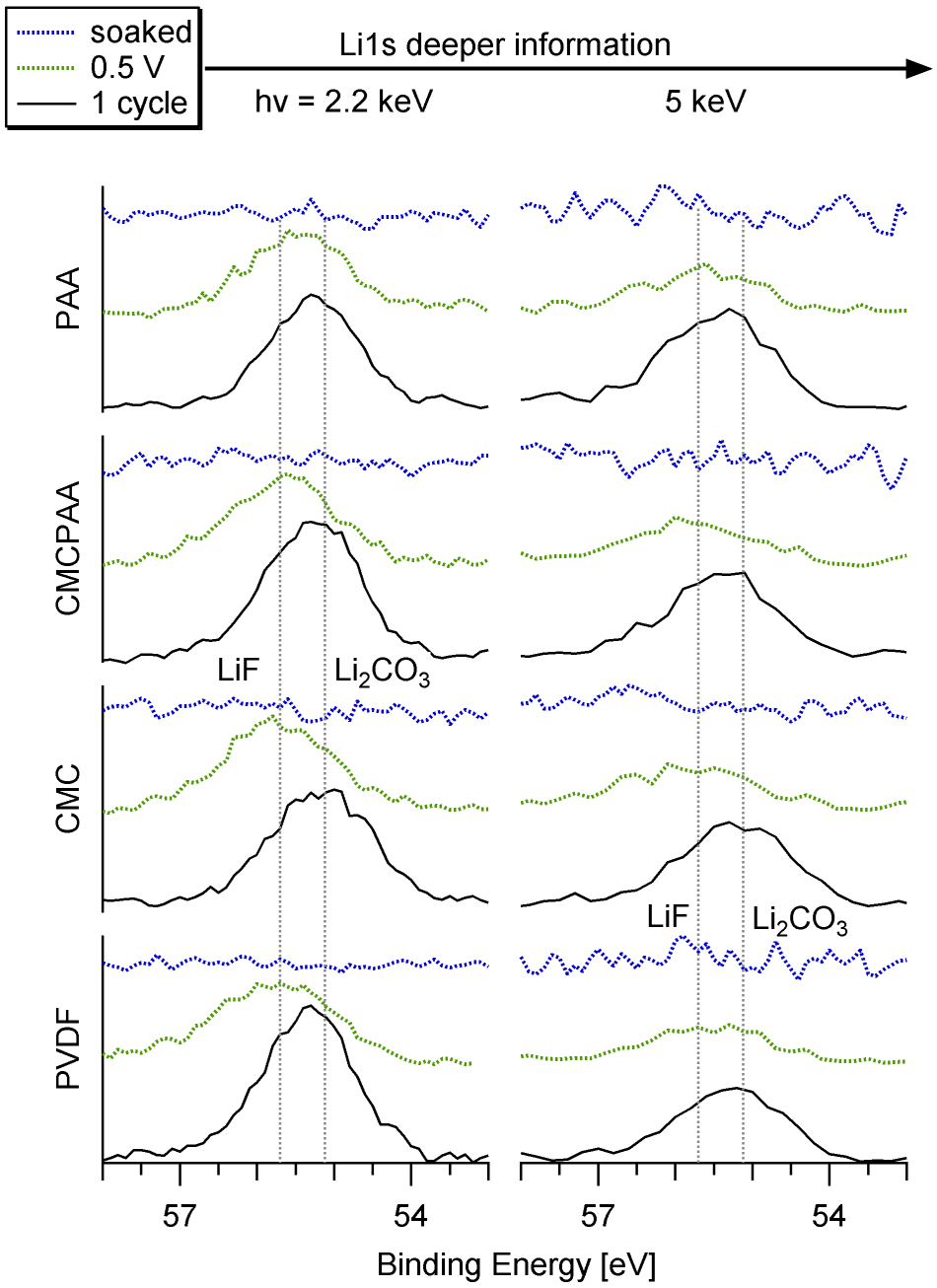

Figure 3-36: Li 1s spectra for anodes: soaked (blue dots), half-cycle (green dots), and one cycle (black).

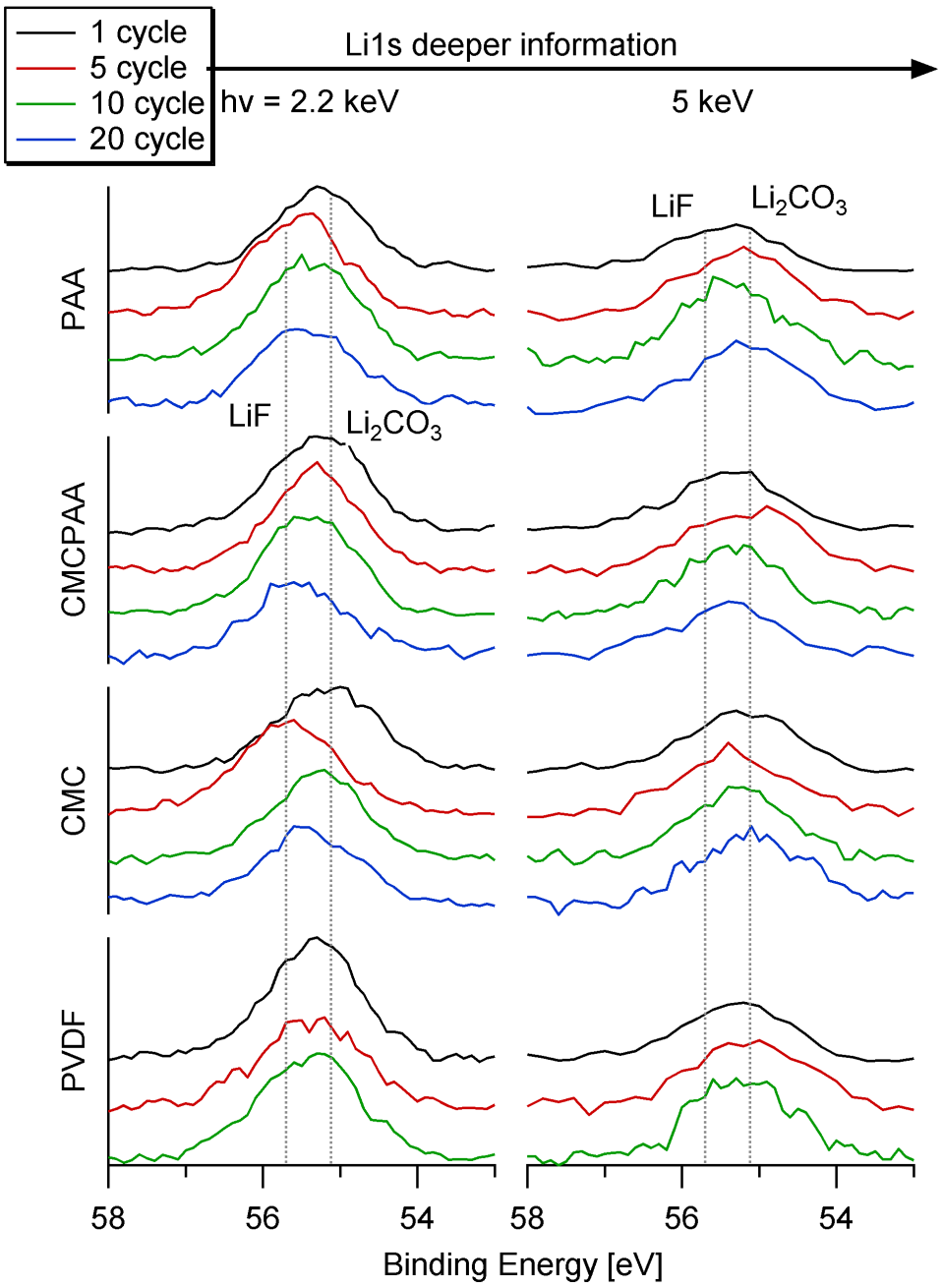

Figure 3-37: Li 1s spectra for batteries cycled one (black), five (red), ten (green), and 20 (blue) times.

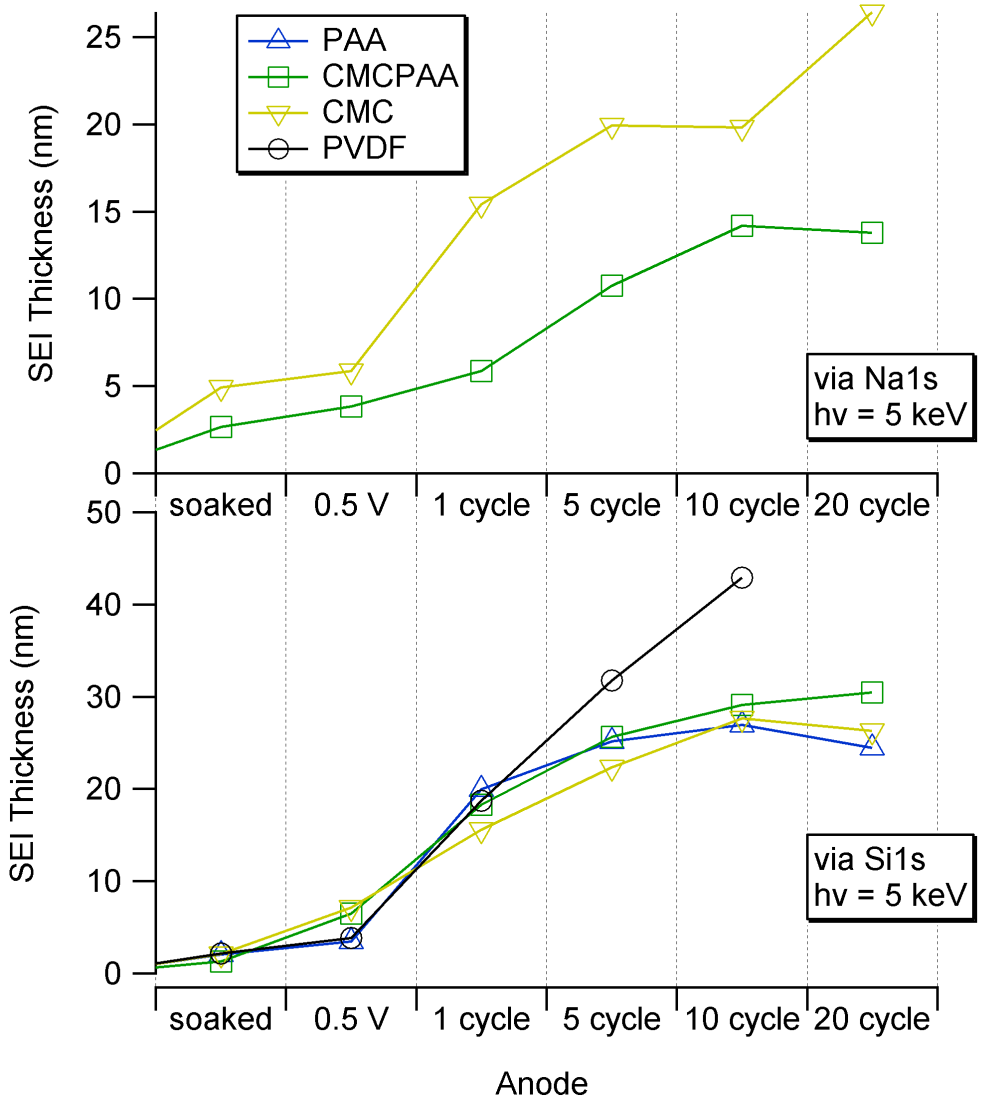

Figure 3-38: Estimates of the SEI thickness, derived from the Si 1s (upper pane) and Na1s (lower pane) signal at hv = 5 keV on anodes using PAA (blue, up triangle), CMCPAA (green, square), CMC (yellow, down triangle), and PVDF (black, circle) binder material.

3-9 Tables

Table 3-4: Atomic concentrations for anodes with PAA binder. Spectra collected at 2.2 keV photon energy.

PAA	P	Si	F	O	C	Li
energy (keV)	2.2	2.2	2.2	2.2	2.2	2.2
fresh		42.2%		41.1%	16.8%	
soaked	1.8%	15.8%	1.3%	17.6%	61.5%	1.9%
0.5 V	1.7%	11.3%	8.9%	20.6%	40.5%	17.0%
1 cycle	1.3%	1.5%	5.4%	34.8%	26.5%	30.5%
5 cycle	0.4%	0.7%	5.1%	28.1%	40.0%	25.7%
10 cycle	0.3%	0.5%	3.7%	34.8%	35.6%	25.2%
20 cycle	0.4%	1.4%	4.3%	29.2%	41.1%	23.5%

Table 3-5: Atomic concentrations for anodes with PAA binder. Spectra collected at 5 keV photon energy.

PAA	P	Si	F	O	C	Li
energy (keV)	5	5	5	5	5	5
fresh		17.9%		18.8%	63.3%	
soaked	1.6%	13.5%	0.8%	17.7%	59.4%	7.0%
0.5 V	2.5%	11.0%	6.4%	20.1%	47.6%	12.4%
1 cycle	1.0%	2.8%	6.7%	32.8%	26.9%	29.8%
5 cycle	0.6%	2.1%	4.4%	32.2%	35.9%	24.7%
10 cycle	0.2%	1.7%	3.1%	40.7%	37.7%	16.6%
20 cycle	0.4%	1.8%	3.2%	33.4%	38.1%	23.1%

Table 3-6: Atomic concentrations for anodes with CMC and PAA binder. Spectra collected at 2.2 keV photon energy.

CMCPAA	P	Si	F	O	C	Li	Na
energy (keV)	2.2	2.2	2.2	2.2	2.2	2.2	2.2
fresh		21.1%		20.7%	57.3%		0.9%
soaked	1.9%	20.2%	1.8%	19.8%	51.1%	4.4%	0.8%
0.5 V	2.1%	10.9%	7.7%	25.5%	36.9%	16.3%	0.5%
1 cycle	0.8%	2.0%	2.3%	37.3%	32.8%	24.5%	0.3%
5 cycle	0.2%	1.1%	3.1%	34.2%	34.9%	26.1%	0.3%
10 cycle	0.4%	0.8%	4.1%	30.9%	38.0%	25.7%	0.1%
20 cycle	0.3%	0.9%	5.9%	32.3%	44.0%	16.4%	0.2%

Table 3-7: Atomic concentrations for anodes with CMC and PAA binder. Spectra collected at 5 keV photon energy.

CMCPAA	P	Si	F	O	C	Li	Na
energy (keV)	5	5	5	5	5	5	5
fresh		18.0%		18.2%	62.5%		1.3%
soaked	2.6%	14.3%	1.4%	17.4%	56.3%	7.0%	0.9%
0.5 V	1.5%	10.6%	5.8%	22.1%	40.2%	18.9%	0.8%
1 cycle	0.5%	3.0%	1.9%	38.7%	31.4%	23.9%	0.6%
5 cycle	0.4%	1.9%	2.2%	37.6%	34.2%	23.5%	0.3%
10 cycle	0.4%	1.4%	4.3%	34.8%	37.0%	21.9%	0.2%
20 cycle	0.7%	1.3%	5.3%	33.2%	38.7%	20.5%	0.2%

Table 3-8: Atomic concentrations for anodes with CMC binder. Spectra collected at 2.2 keV photon energy.

CMC	P	Si	F	O	C	Li	Na
energy (keV)	2.2	2.2	2.2	2.2	2.2	2.2	2.2
fresh		18.2%		29.4%	50.2%		2.2%
soaked	1.2%	14.3%	3.0%	29.6%	46.3%	4.2%	1.4%
0.5 V	2.4%	8.5%	6.5%	31.2%	32.4%	17.9%	1.1%
1 cycle	0.9%	2.9%	3.0%	36.3%	30.1%	26.7%	0.3%
5 cycle	0.4%	1.4%	11.0%	24.8%	33.8%	28.3%	0.2%
10 cycle	0.3%	1.0%	3.1%	33.0%	39.0%	23.5%	0.2%
20 cycle	0.4%	1.2%	4.5%	29.4%	40.8%	23.5%	0.1%

Table 3-9: Atomic concentrations for anodes with CMC binder. Spectra collected at 5 keV photon energy.

CMC	P	Si	F	O	C	Li	Na
energy (keV)	5	5	5	5	5	5	5
fresh		16.3%		26.4%	54.5%		2.8%
soaked	2.2%	12.0%	1.9%	23.9%	47.8%	10.6%	1.6%
0.5 V	1.7%	9.1%	6.2%	29.1%	38.3%	14.2%	1.4%
1 cycle	1.1%	4.2%	2.9%	36.3%	32.4%	22.6%	0.5%
5 cycle	0.9%	2.6%	8.0%	30.0%	36.5%	21.8%	0.3%
10 cycle	0.9%	1.5%	2.3%	36.8%	35.8%	22.3%	0.3%
20 cycle	0.6%	1.4%	3.5%	34.0%	36.7%	23.6%	0.2%

Table 3-10: Atomic concentrations for anodes with PVDF binder. Spectra collected at 2.2 keV photon energy.

PVDF	P	Si	F	O	C	Li
energy (keV)	2.2	2.2	2.2	2.2	2.2	2.2
fresh		26.4%	12.0%	10.8%	50.8%	
soaked	1.7%	17.0%	16.7%	7.6%	55.3%	1.8%
0.5 V	1.8%	13.3%	9.6%	25.8%	34.2%	15.3%
1 cycle	0.3%	0.7%	2.3%	39.3%	28.0%	29.4%
5 cycle	0.3%	0.8%	6.1%	27.5%	39.2%	26.0%
10 cycle	0.5%	0.6%	8.3%	27.9%	36.1%	26.7%

Table 3-11: Atomic concentrations for anodes with PVDF binder. Spectra collected at 5 keV photon energy.

PVDF	P	Si	F	O	C	Li
energy (keV)	5	5	5	5	5	5
fresh		20.1%	14.2%	7.3%	58.3%	
soaked	1.7%	12.1%	17.0%	7.7%	56.2%	5.3%
0.5 V	1.5%	12.7%	10.5%	22.6%	40.3%	12.4%
1 cycle	0.3%	1.2%	2.5%	43.6%	26.2%	26.2%
5 cycle	0.3%	1.9%	5.4%	31.4%	35.0%	25.9%
10 cycle	0.4%	0.8%	5.8%	8.1%	56.4%	28.5%

APPENDICES

APPENDIX A: LabVIEW Virtual Instrument for experimental logging and I/O

1) Introduction

The experimental control for data input and output, as well as logging procedures for experimental parameters is accomplished through the use of a Virtual Instrument (VI) which was written in the LabVIEW development suite from National Instruments. This appendix will explain the construction and operation of the VI.

2) General Design

The development suite used to compose the VI is LabVIEW 2011, service pack one. The very basic principle of the IPES functionality of this VI was carried over from our previous system, in the form of a LabVIEW 8.6 VI. Upgrading the machine, software, and hardware required a complete rewriting of the VI due to incompatibilities in the code. Currently, the VI interfaces with the fast-pulse counting system and the potential scaler via a USB Data Acquisition Device (DAQ) from National Instruments (NI USB-6009), and with the Fluke 8808A 5.5 digit multimeter by a RS-232 to USB cable, both connected to the experimental control PC. Drivers for the DAQ and the Fluke meter were downloaded from the example VIs available in the LabVIEW Help web resource.

The LabVIEW VI consists of two main aspects. The front panel, which the user sees and may manipulate is accessible to the user through a shortcut on the PC desktop. The graphical programming is done on the Back Panel, or Block Diagram. The general user may not access the Block Diagram under current conditions because the master VI file is compiled to produce an executable file which is deployable to any

computer with similar hardware. This precaution prevents accidental deletions or alterations to the code and allows users without a LabVIEW license to use it.

A screenshot of the entire Block Diagram is shown in Figure A-39. Individual components are far too small to be helpful in this format and it is included only to help the reader place the individual sections displayed in the other figures within the context of the whole VI. The overall structure is in the form of an ordered sequence. The first pane of the sequence spans approximately the first half of the Block Diagram in Figure A-39 and contains two parts. First is a collection of the various shared variables defined on the Front Panel (far left frame, Figure A-41) available to all components of the VI, boxed in the left part of the first ordered sequence pane. Immediately to its right is a large case structure which is the second part of this first pane. The case structure is composed of six cases, one corresponding to each possible selection in the tabbed structure of the front panel.

Upon completion of an experiment event, the VI plays an alarm sound and suspends execution in an infinite loop in the second pane of the ordered sequence until the print safety is engaged, at which point execution proceeds to the third sequence pane where the data is written to an automatically named spreadsheet file and the information about that event is added to an automatically named log file for that day. Finally, the final pane of the ordered sequence updates the “last file written” variable in the lower left corner of the Front Panel to reflect the data just recorded and instructs the electron gun to sit at the lowest energy available. These are safety measures to help ensure no files are overwritten and that the GM detector is not being unnecessarily bombarded with photons when the experiment is in IPES mode.

The experimental event is determined by which tab of the tabbed structure is selected. Each tab, when selected, displays a different version of the Front Panel and engages a different part of its corresponding case structure on the back panel. Figure A-41, Figure A-44, Figure A-47, Figure A-50, Figure A-53, and Figure A-56 are screenshots of the Front Panel views when the user selects the Sputter, IPES, Work Function, LEED, Anneal, and e Gun Calibrator tabs, respectively. Figure A-42, Figure A-45, Figure A-48, Figure A-51, Figure A-54, and Figure A-57 are screenshots of the experimental control sections for each of the tab cases, and the logging sections for each are represented in Figure A-43, Figure A-46, Figure A-49, Figure A-52, Figure A-55. There is no experimental logging done for the electron gun calibrator function.

3) Specific Experimental Components

a. "Sputter" Tab

The sputter portion of the experiment controls the data acquisition, data logging, and experimental logging for the ion bombardment component of the experiment. There is no experimental control facet to this tab – it passively collects readings of current developed across the sample during the bombardment process at user-defined time increments. On the front panel shown in Figure A-41, the user enters the gas type, pressure, sample location parameters, and event index in the static left pane. In the tabbed structure, the user enters the total time for sputtering and the Sputter Step, in ms, to define how long the program waits to collect each reading of the current. Because of the way the Fluke interface and drivers work, this value should not be less than 200 ms in order to allow sufficient time for the meter to

provide a measurement within its sub-VI before requesting another reading. The Beam Voltage, Emission Current, and Focus variables are simply entered for logging purposes and do not often change from the default values.

Upon beginning the Sputter event, the user engages the beam voltage on the external sputter gun control. There is an approximate 8 second lag between execution and the beginning of the current record due to initialization of the various back panel components. Once logging begins, the current vs. time chart is updated every second to report the progress.

On the back panel, this section is controlled by the characteristic case ("Sputter", Default) and a timed loop within it. The VI determines the iteration limit for the timed loop from the total sputter time and the Sputter Step time via the calculation VIs in the lower left corner of Figure A-42 and passes this value into the timed loop where it triggers a stop condition when the iteration limit no longer exceeds the loop count. Just above the calculation sub-VIs is the initialization for the Fluke meter. Here the measurement type and parameters are defined, once per experimental event, and the task identifier is passed to the timed loop. Inside the timed loop, the Read Measurement VI (eyeglasses icon) is connected to this identifier and accepts one reading per loop iteration. The loop controls are defined by the user-inputted Sputter Step and the onboard kHz clock as shown in the upper left corner of the timed loop. Once the current reading is acquired, it is paired to the associated time value and added to the buffer feeding the front panel plot and appended to the 2D indexed data tunnel on the right side of the timed loop. Upon completion of the loop, the array is passed to a 2D variable called "Sputter Data 2D" shown on the right side of the index

tunnel. This variable is then available to the logging portion of the program in the next frames of the ordered sequence.

When the first frame of the ordered sequence (Figure A-39) is complete, as in all tabs of the tabbed structure, the sputter tab hangs up in an infinite loop until the user engages the print button at top left in the front panel (Figure A-41). This allows the user to double-check the input parameters for the experimental logging before writing the files. Once the print button is engaged, the penultimate frame of the ordered sequence executes and automatically logs the data and experiment information in separate files. As in the first frame, this is accomplished via a case structure that is determined by the tab selected on the front panel. Figure A-43 shows the logging frame of the ordered sequence and will be explained here in detail, though the other capabilities of this VI share many of the same features and will be less thoroughly treated hereafter.

The case structure is broken up with containers which have no real programmatic function except to help organize the constituent parts. The top left container in the figure provides a dialog to the user in which the user is asked to verify the filename for the data just recorded. The filename it suggests to the user is built in the two containers just below this on the block diagram. The one immediately below the dialog container builds the event index identifier and the container below that obtains the date from the computer and builds the file prefix in the format "year"."month"."date". The event index for sputtering appends ".sputter.0xx" to this, where "xx" is the user-defined index from the front panel. Once the user accepts the suggested name or corrects it to suit, the VI automatically completes the next steps and

logical choices: (top right container) create spreadsheet file with requested name and write the data saved from the first frame of the ordered sequence to it; (bottom left container) build tab-delimited experimental log information; and (bottom right container) create automatically named .txt file to hold experimental information if it does not already exist, read data in the log file and close it, append new information to old, then overwrite the log file and close it. There are multiple Build Text VIs in the lower left container because a single VI can only accept information from eight variables. They may effectively be daisy-chained to get around this restriction, using the output of one to inform the "first line" of the next.

Finally, the common final pane of the ordered sequence executes after the log and data files are saved. The electron gun is held at the lowest possible potential to avoid unnecessary avalanches in the detector and the selected filename updates the "Last File Written" field on the front panel to avoid confusion for inputting the next event index.

b. "IPES" Tab

Much of the machinery for the IPES tab is similar to that employed in the Sputter Tab. There are no additional variables defined in the tab-specific portion of the front panel (Figure A-44), and everything necessary to run the experiment is defined in the left frame. Variables not needed in the Sputter Tab include those labeled "Spectrum Control" (energy range, number of scans, step size, dwell time, and the current provided to the electron gun filament) and those labeled "Detector" (bias, linear position, temperature, amplification, pressure, and the date of the last gas change). There are two plots displayed in the tab. The upper plot displays the currently

collecting raw data, updated with every data point collected, and resets to a blank set of axes upon completion of each scan. The lower plot displays two traces corresponding to the raw data and to the sample current normalized data, both of which update at the end of each scan and reflect the sum of all collected scans up to that point.

The back panel for the IPES tab is somewhat more complicated than the Sputter Tab because there is an experimental control aspect and because the experiment iterates a user-defined number of times. The core of the back panel (Figure A-45) is a pair of nested for loops. The initialization for the counter, the potential ramp for the electron gun, and the Fluke meter are handled outside the loops, so they need only happen once for an experimental event. The four property nodes above the outer for loop define the energy axis range for the plots, to avoid unnecessary redrawing of the axes upon every data point acquisition. The outer for loop controls an individual scan. It takes as input, from the inner for loop, three 1D arrays of numbers corresponding to the energy, counts, and current readings for the user defined number of steps in the scan. Each time the inner loop completes its assignment, the outer loop adds each new array to the previous one and holds the sum in shift registers (at the bottom left and right of the outer for loop). At that time it also updates the lower plot on the front panel.

The operation of the inner loop is less straightforward because of the synchronization of the data I/O. We desire to read the current developed across the sample at some time within the user defined “Dwell (ms)”, which is analogous to the Sputter Step from the Sputter tab and defines how long the VI counts photons at each

individual energy step. Collecting counts and taking the current reading should happen simultaneously and both tasks should be complete when the requested dwell time has passed. This is accomplished through the use of a stacked sequence and an ordered sequence within its second frame. In the first frame (not shown in Figure A-45), the appropriate potential for the given energy step is calculated from the loop iteration and the parameters defined on the front panel and this value is sent to the external scaler for the electron gun through the DAQ. Once this is complete, the energy of the electron beam changes and the second frame of the stacked sequence (shown in Figure A-45) initiates. The current reading is requested from the Fluke meter as the counter is initiated in the first frame of an ordered sequence. In the second frame of the ordered sequence is a Wait VI which delays the execution of the sequence by the user defined dwell time. The final frame reads the counter and stops (resets) it. The counts and current are passed to the indexed array data tunnel on the right side of the for loop and also to the updating upper plot on the front panel. The user input energy range and energy step determine how many times the inner loop iterates before passing control back to the outer loop. As with the Sputter Tab, this frame of the tabbed case structure completes when all the requested data is collected and saved as a variable, here called "IPES array" which is available to subsequent portions of the program.

The print hold and logging procedures are largely the same as for the Sputter Tab. Different information is written to the data file and appended to the log file, and that portion of the code is reproduced in Figure A-46. Refer to section a for a more thorough explanation.

c. Work Function Tab

The part of the VI concerning work function measurements is essentially the same as the IPES experiment, except we do not collect the counts from the detector. The front panel in Figure A-47 looks like that of the IPES Tab with addition of a "Sample Bias" variable. This is only used for logging purposes and the two plots are again used to represent the currently collected and summed data. On the back panel (Figure A-48) the timed loop is employed due to the less complicated requirements of synchronization for this experiment. The further tabs available in the structure are not described in detail because they are not currently active data collection tabs and their functionalities are largely developed already in the above sections.

Figures

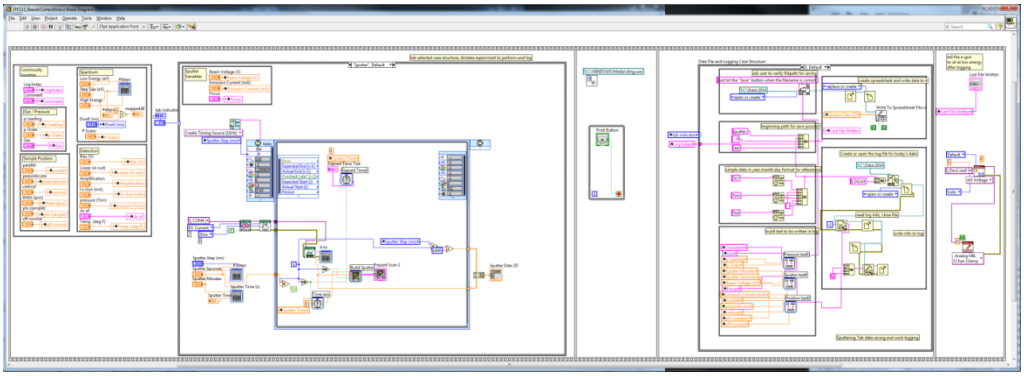

Figure A-39: Block Diagram (back panel) of whole VI

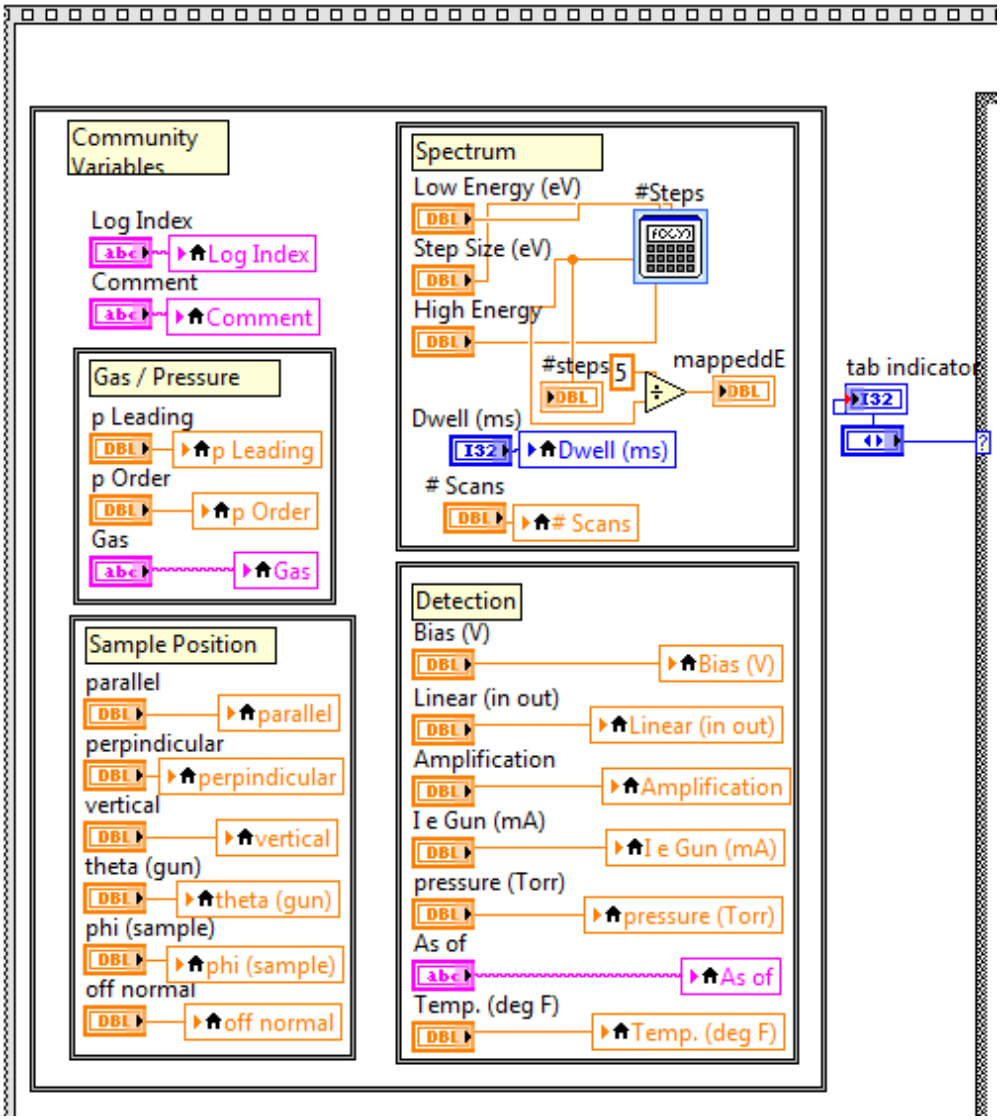

Figure A-40: Block Diagram selection for keeping user-defined experimental parameters

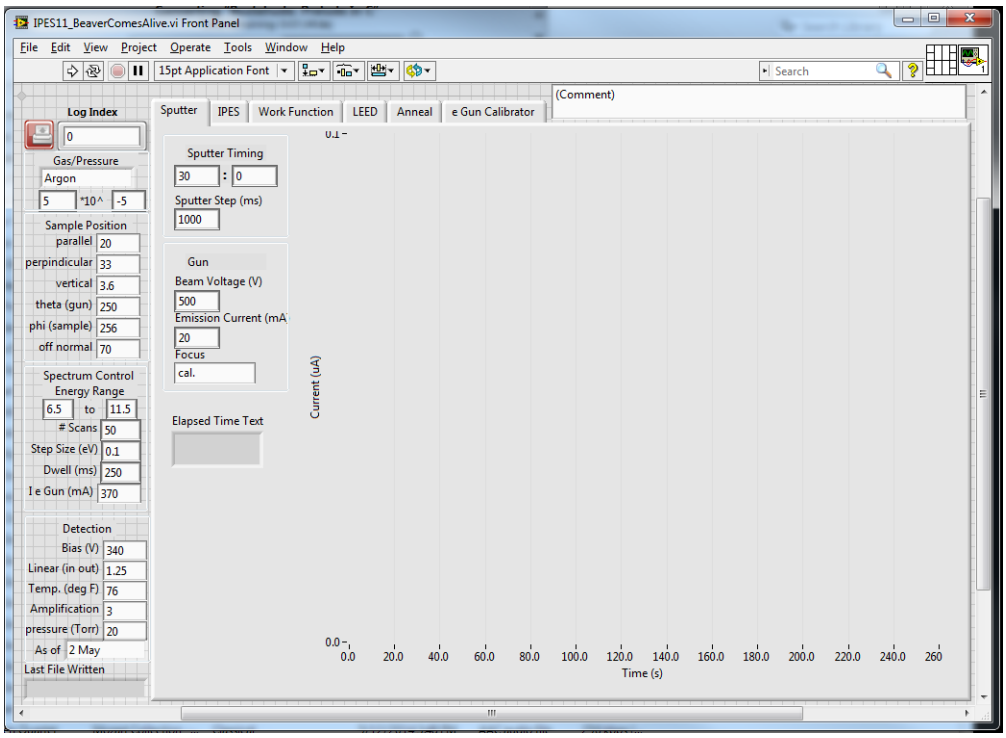

Figure A-41: Front Panel for "Sputter" tab

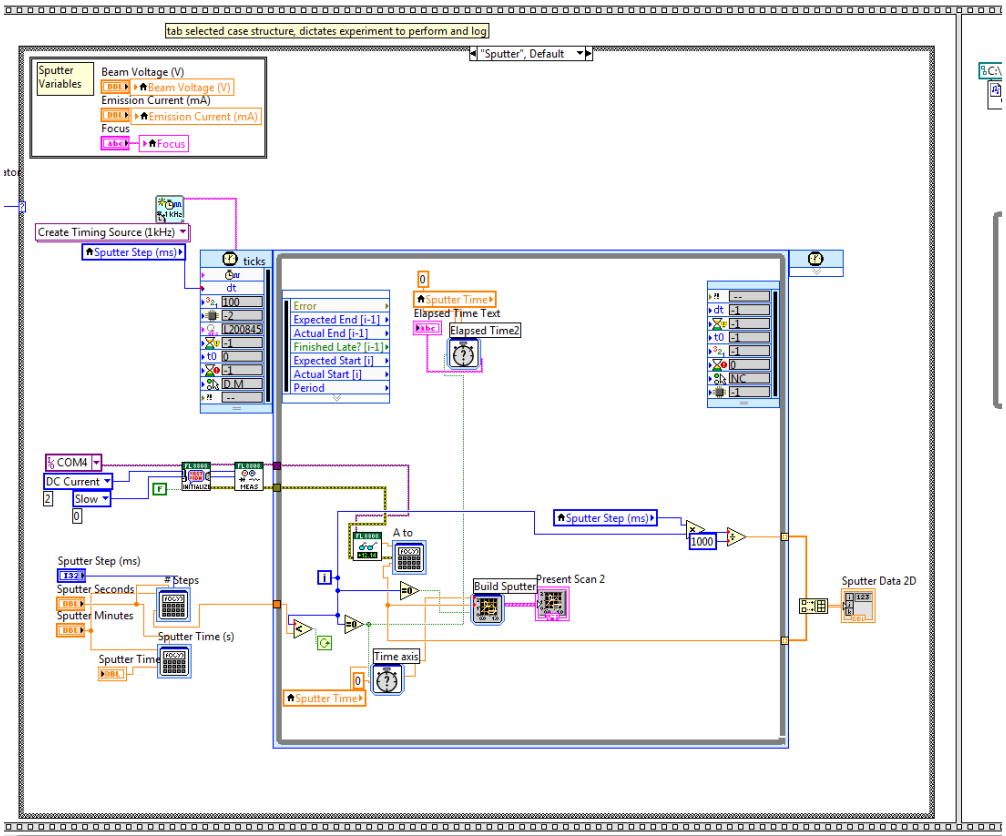

Figure A-42: Block Diagram for "Sputter" tab, experimental control section

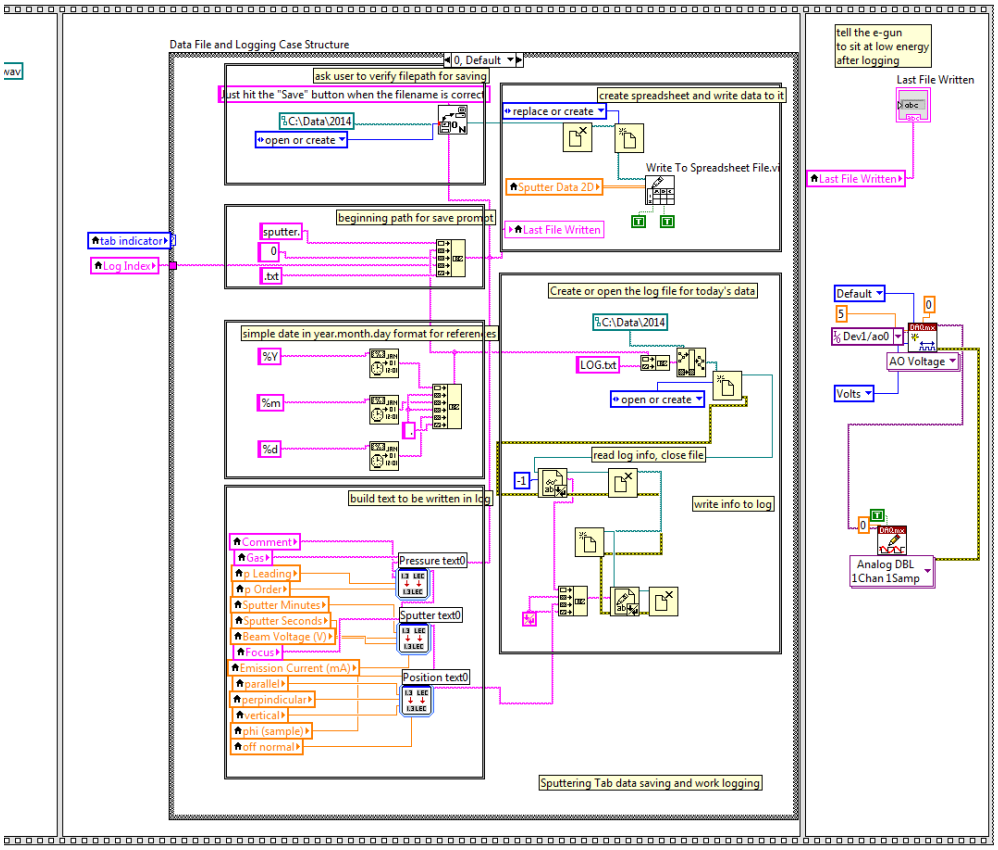

Figure A-43: Block Diagram for "Sputter" tab, experimental and data logging section

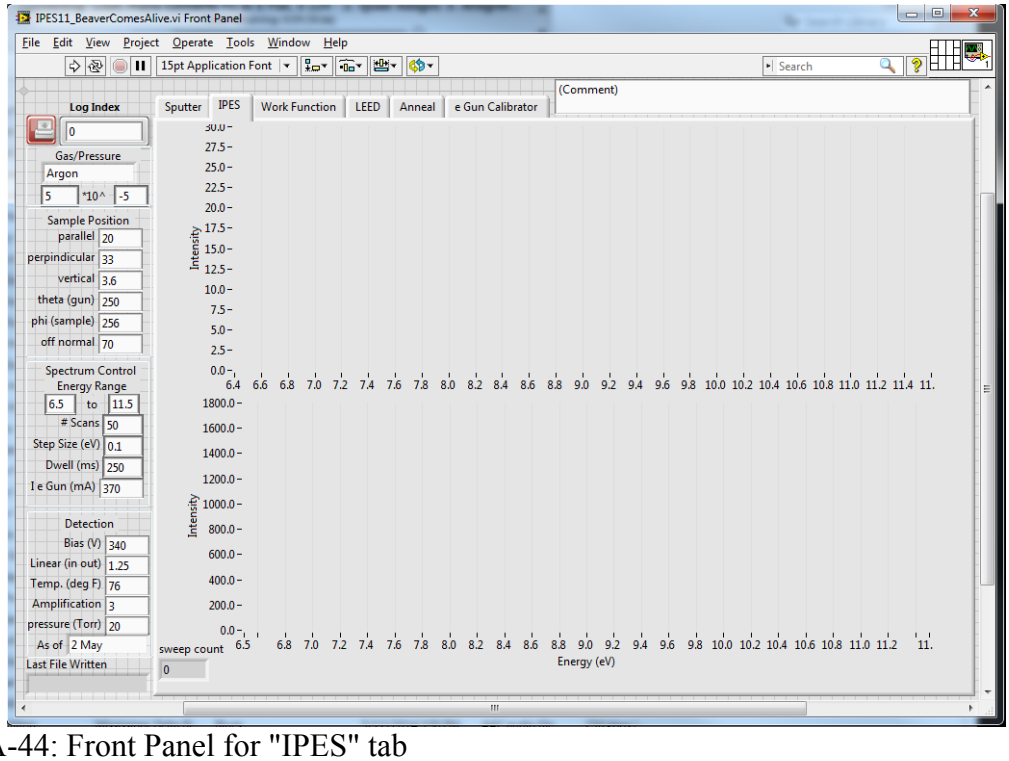

Figure A-44: Front Panel for "IPES" tab

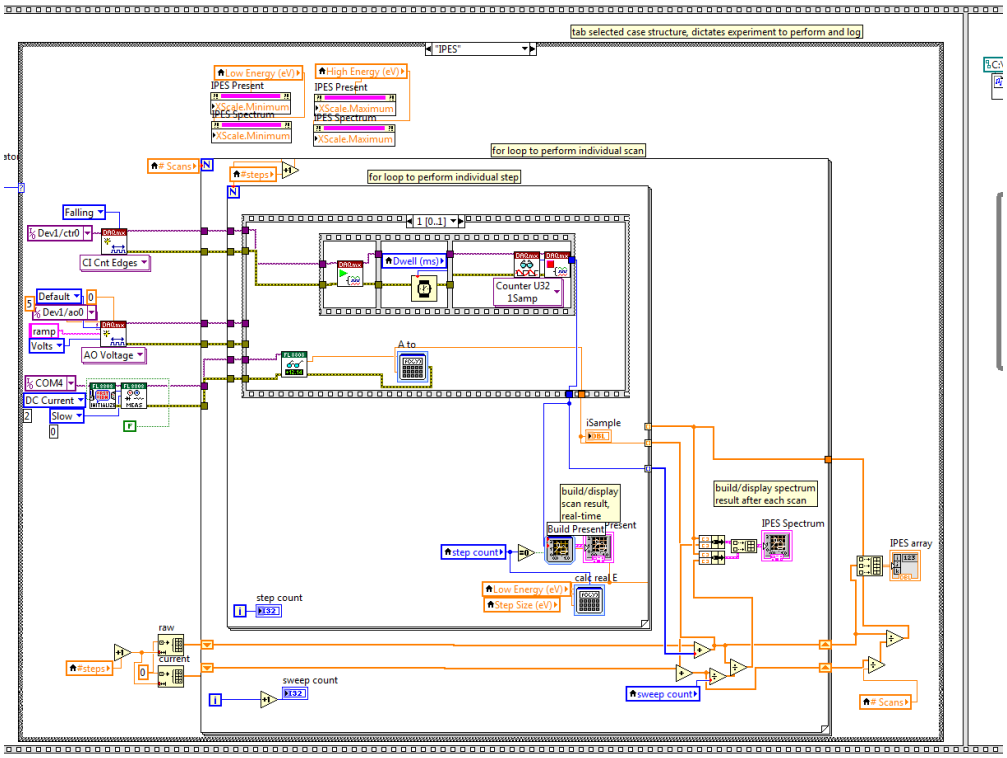

Figure A-45: Block Diagram for "IPES" tab, experimental control section

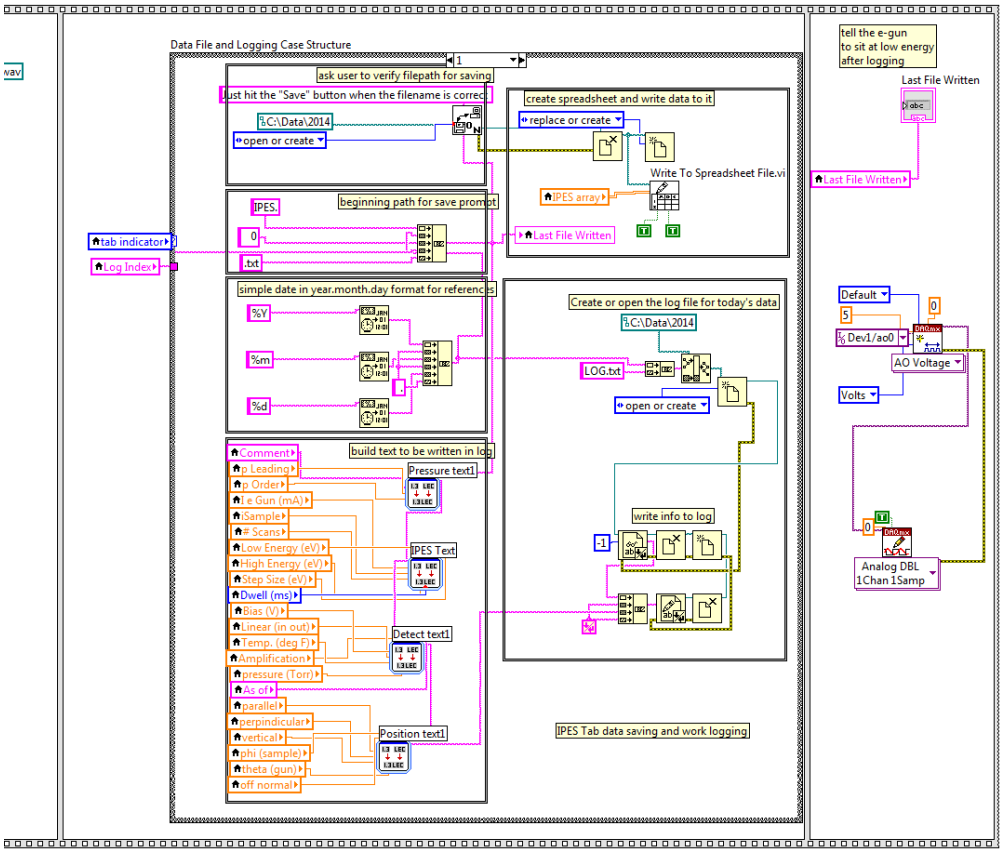

Figure A-46: Block Diagram for "IPES" tab, experimental and data logging section

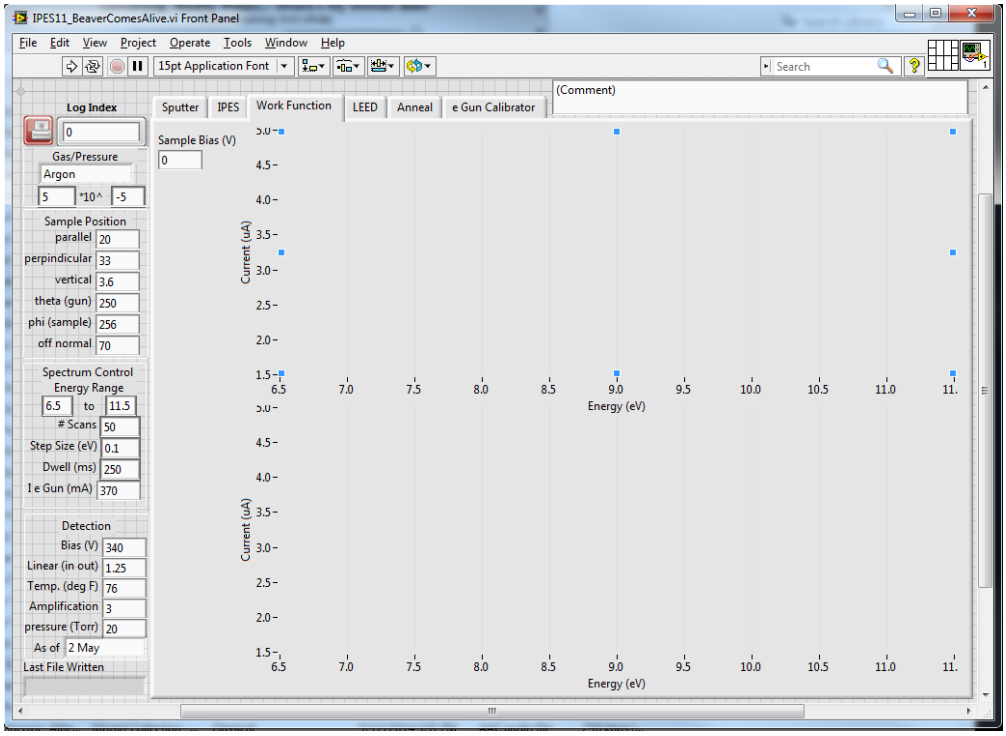

Figure A-47:Front Panel for "Work Function" tab

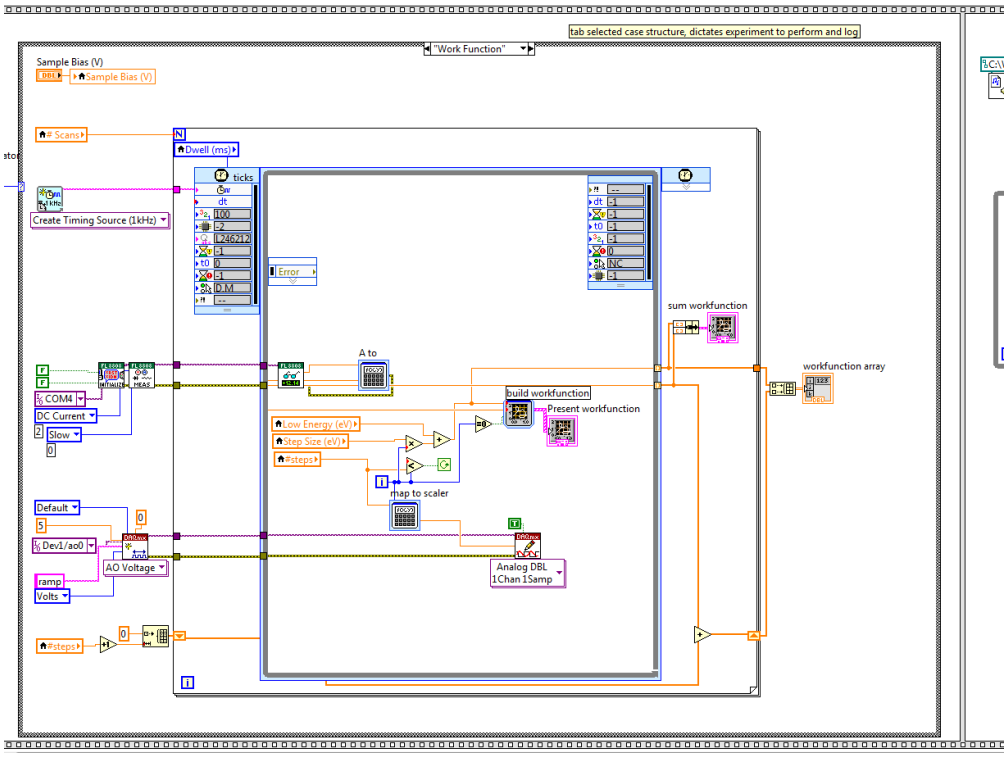

Figure A-48: Block Diagram for "Work Function" tab, experimental control section

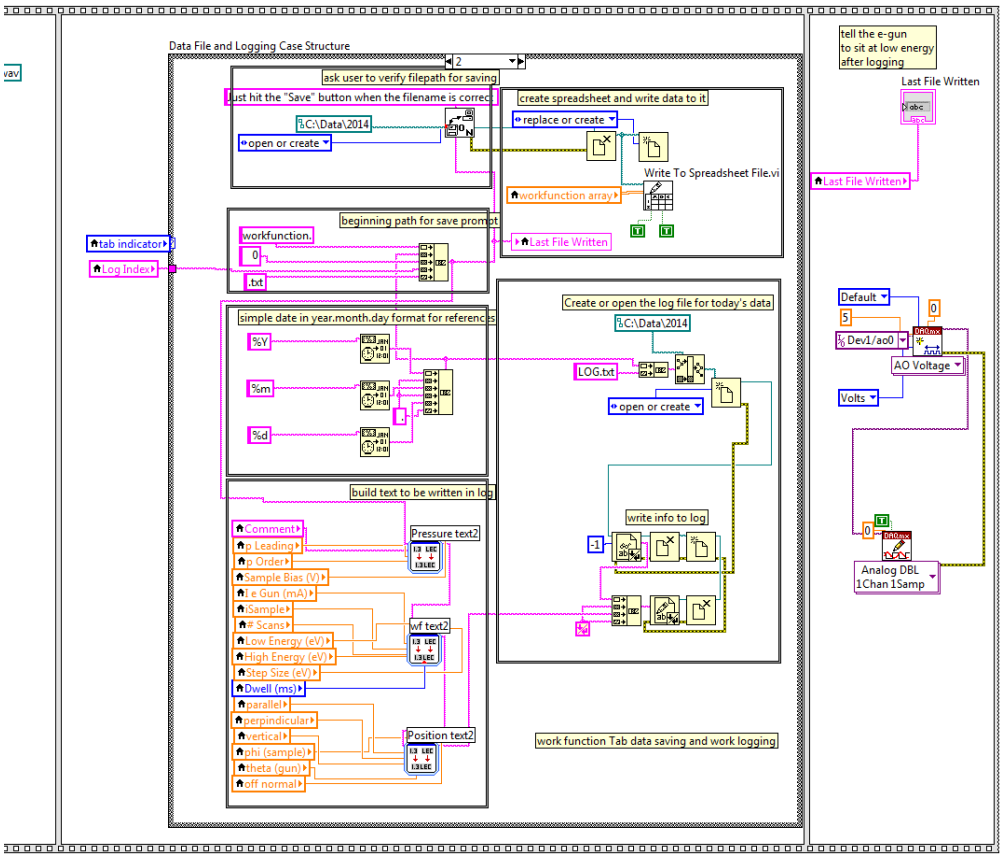

Figure A-49: Block Diagram for "Work Function" tab, experimental and data logging section

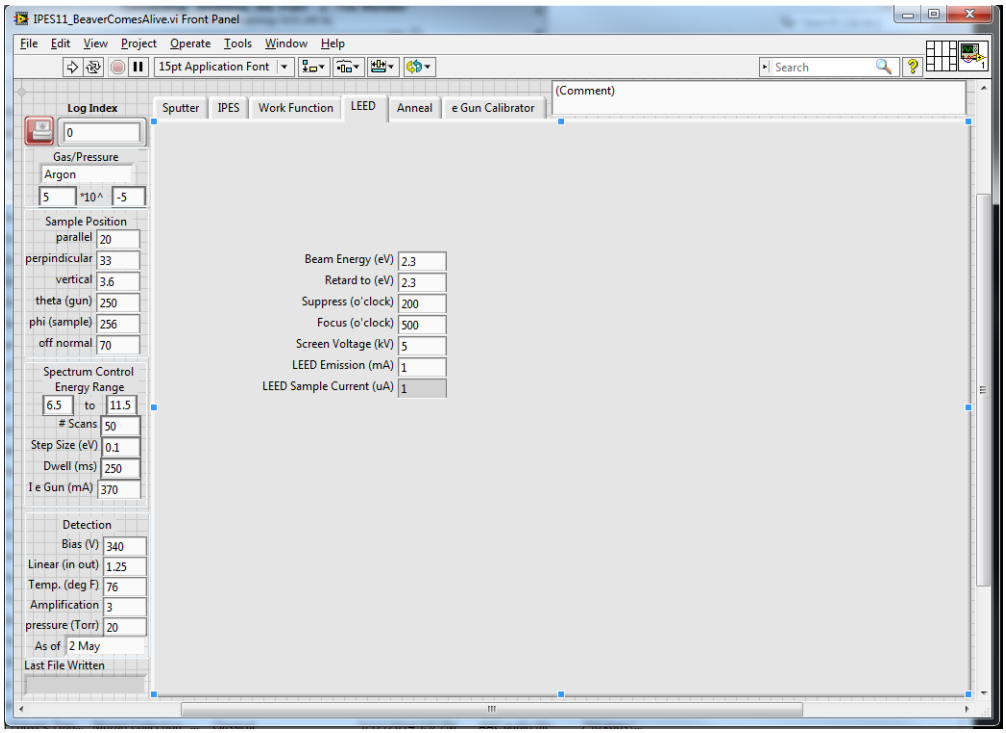

Figure A-50: Front Panel for "LEED" section

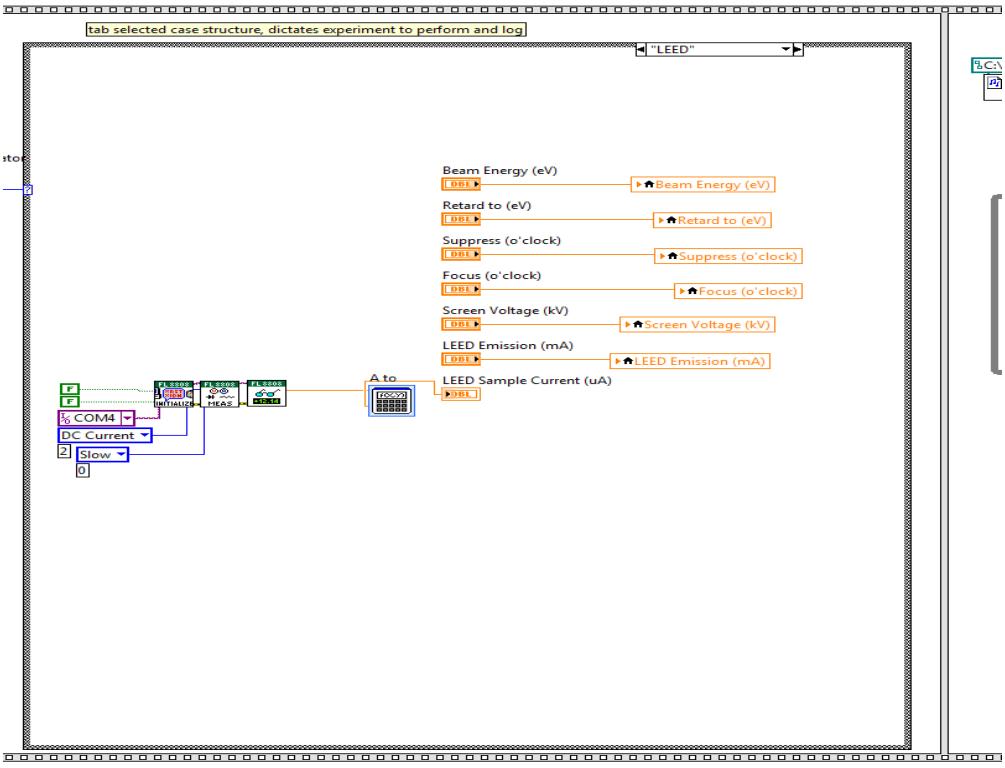

Figure A-51: Block Diagram for "LEED" tab, experimental control section

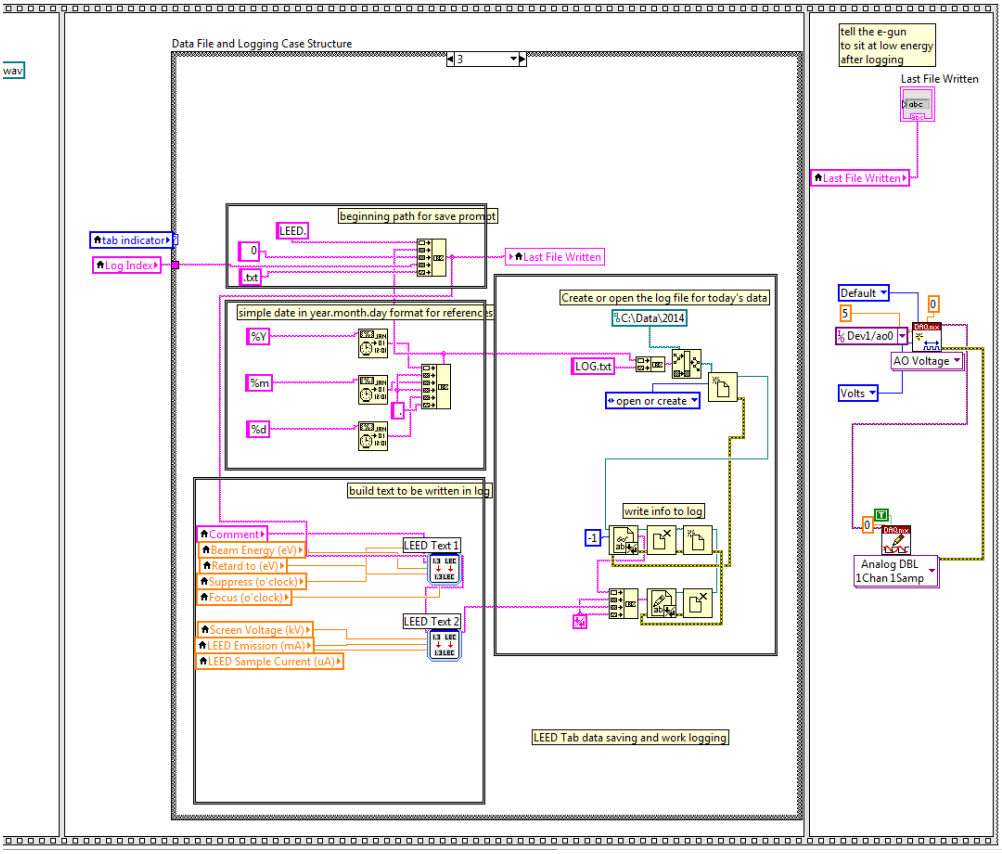

Figure A-52: Block Diagram for "LEED" tab, experimental and data logging section

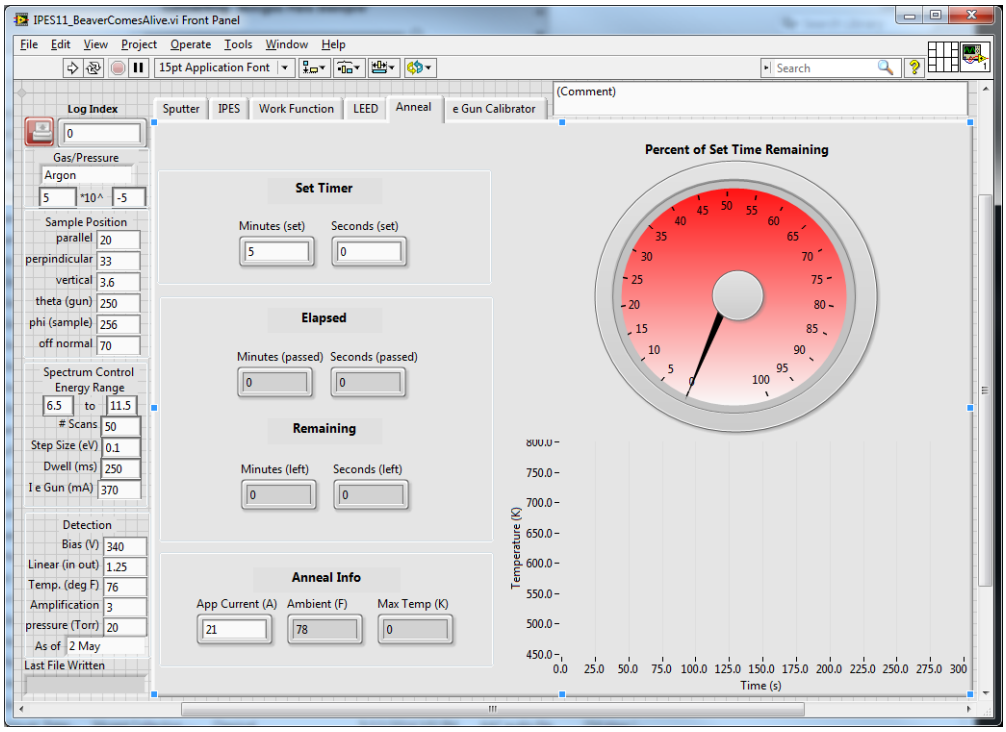

Figure A-53: Front Panel for "anneal" tab

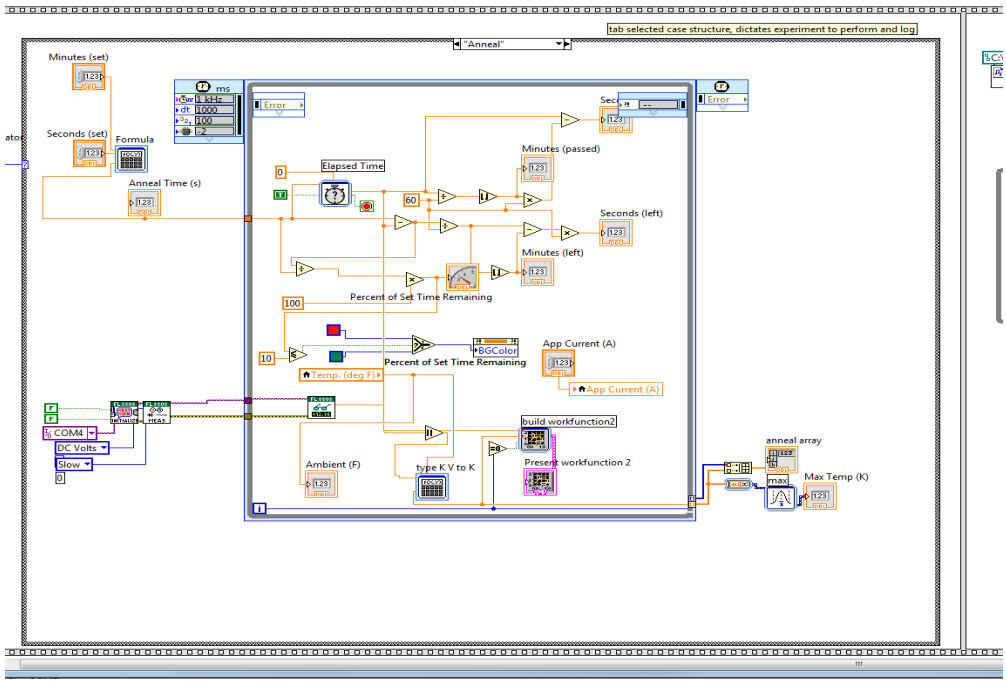

Figure A-54: Block Diagram for "Anneal" tab, experimental control section

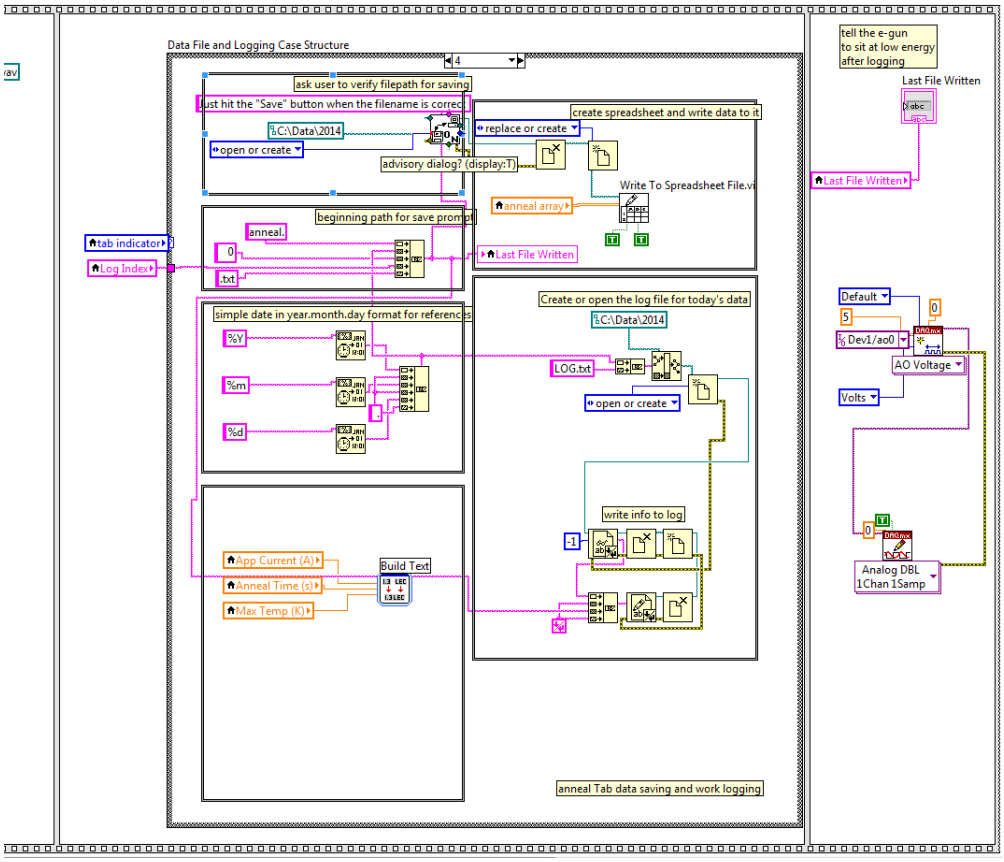

Figure A-55: Block Diagram for "Anneal" tab, experimental and data logging section

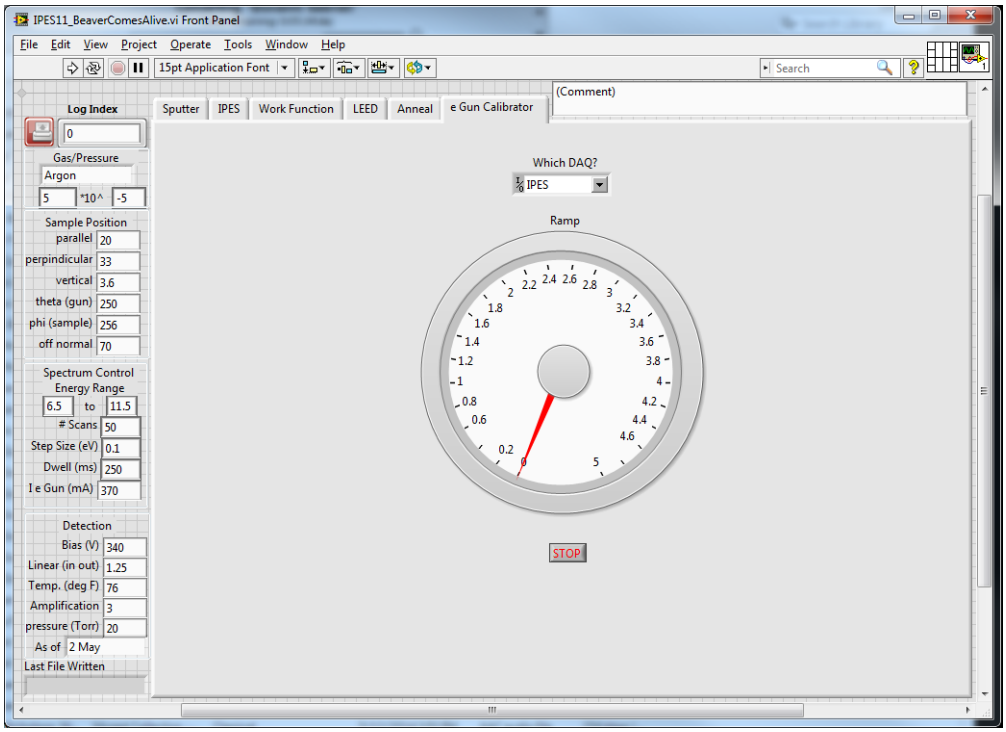

Figure A-56: Front Panel for "e Gun Calibrator" tab

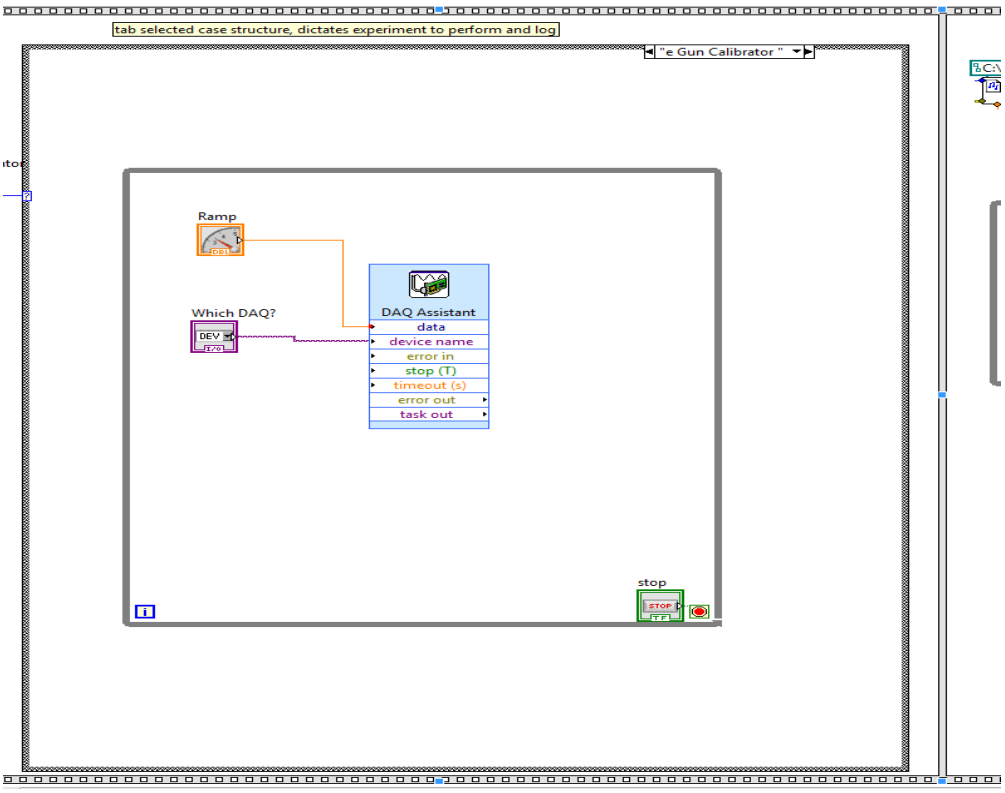

Figure A-57: Block Diagram for "e Gun Calibrator" tab, experimental control section

APPENDIX B: SPA-LEED Analysis Routine

This sample of Mathematica work handles the analysis of a set of LEED images for spot intensity profiles. Major components have brief introductions and the code is commented in-line as well for details. The more useful version of this is on file in the URI Surface Lab as a Mathematica notebook.

Previous versions are obsolete. Updates include implementation of nearest neighbor averaging to determine circular spot profile analysis instead of the old averaging around a square annulus, as well as the capability to iteratively find the centers of the diffraction spots. The latter permits automation of the analysis once the user points Mathematica to the image files to be analyzed and inputs the rough locations of the spots in the first image of the set. Should be a trivial task to update this to analyze IV curve data. All that ought to be required is to have it educate itself on predicting the next dot center to pass to itself as the center initial guess. For now it is not problematic that the program uses the previous location as the initial guess because the only movement of the spots is due to inconsistent sample placement, generally only a few pixels in any direction and well within the search capabilities of the re-centering algorithm.

```
Clear["Global`*"];(*clear the memory of any defined symbols*)
saveData = {};(*create an empty array to hold the analysis*)
```

Build the Spot Profile Analysis coordinate matrix
Output is a table with levels:
1) nearest neighbor set index, first row corresponds to center pixel, number of elements at this level is determined by the input radius.
2) NN set index, distance from center pixel (pixels), multiplicity of pixels at this distance, {pixel locations relative to the center}, unnormalized area gained by adding this set of NN pixels}

```
DefineAnalyzeDot[r_(*search radius*)] :=
 Block[{NNDistanceSample, NNDistancesR, NNDistancesNR, indexlist, roughlocs,
   locations, sortedlocationindices, sortedlocations, grumpy, scaledgrumpy,
   result},
  (*creates a table (2n+1 x 2n+1 crystal) each element of which is the \
squared distance in index space of the element from the argument (i,j)*)
    NNDistanceSample = Table[{a, b, (a)^2 + (b)^2}, {a, -r, r}, {b, -r, r}];
  (*creates a list in ascending order of the distances from center to each \
set of nearest neighbors, redundant*)
    NNDistancesR = Sort[Flatten[NNDistanceSample, 1], #1[[3]] < #2[[3]] &];
  (*delete redundant distances in the last list,
  output list of unique distances short to long*)
    NNDistancesNR =
   DeleteDuplicates[NNDistancesR, #1[[3]] == #2[[3]] &][[All, 3]];
  (*nearest neighbor set index, center is index 0*)
```

```
 indexlist = Table[c - 1, {c, Length[NNDistancesNR]}];
 (*indices for each distance*)
  locations =
 Table[Select[
    Flatten[NNDistanceSample, 1], #[[3]] == NNDistancesNR[[d]] &][[All,
   1 ;; 2]], {d, Length[NNDistancesNR]}];
 (*finds the shortest path between the points at each distance,
 which defines a non self-intersecting polygon,
 but the output is a list of indices for the ordering*)
  sortedlocationindices =
 Table[FindShortestTour[locations[[e]]][[2]], {e, Length[locations]}];
 (*use ordering indices from previous step to reorder the locations*)
  sortedlocations =
 Table[locations[[f, g]], {f, Length[sortedlocationindices]}, {g,
   sortedlocationindices[[f]]}];
 (*make an empty list to catch the output of the next step*)
  grumpy = Table[0, {h, Length[indexlist]}];
 (*create maps of new area only (white on black), make it black and white,
 total up white pixels, normalize to the size of the search dot,
 throw that value into grumpy*)
 For[
  aa = 2,(*start at the first set of nearest neighbors*)
    aa < Flatten[Position[NNDistancesNR, r^2]][[1]] +
   1,(*stop iterating once the NN set at distance equal to the radius of \
the search dot is included*)
  aa++,(*increment*)
    grumpy[[aa]] = Total[(*add all pixel values*)
    Abs[1 -
     ImageData[(*turn the map into an array*)
      Binarize[
       Graphics[{(*create the Graphics[] map,
          open first list*)
         {(*list 1, primitive 1:
          black background for image stack*)
          White,
          Rectangle[{-r, -r}, {r, r}]},
         {Black, Polygon[sortedlocations[[aa]]]
          }}(*new area*)
        ~Join~
         Table[{White, Polygon[sortedlocations[[i]]]}, {i, 1,
          aa - 1}](*old area*)
       (*could add code here similar to above to find vertices, delete anything inside,
       make a custom polygon so it's not building tens of polygons on top of one
nother*)
       ,
```

```
        ImageSize -> {1001,
          1001}(*make all maps same size*)
        ](*close Graphics[]*)
       , .5]
      ](*close ImageData*)
     ](*close Abs[]*)
    ,
    2](*Total[] at levelspec 2*)
  ];
 scaledgrumpy =
  grumpy/
   Total[
    Abs[
     1 -
      ImageData[
       Binarize[
        Graphics[{{White, Rectangle[{-r, -r}, {r, r}]}, {Black,
           Disk[{0, 0}, r]}}, ImageSize -> {1001, 1001}], .5]]], 2] //
   N;(*same tool kit,
 just figures out scaling factor to find area of new inclusion relative to \
the dot size in pixels®area line is % of search area*)

 scaledgrumpy[[1]] = 1/1001 // N;
 result = Prepend[
   Table[
    {indexlist[[n]], Sqrt[NNDistancesNR][[n]], Length[locations[[n]]],
     sortedlocations[[n]], scaledgrumpy[[n]]},
    {n, Flatten[Position[NNDistancesNR, r^2]][[1]]}], {{"search radius", r},
    "radius", "#Î", "pixel indices", "new area"}]
 ]
MakeTheDough = DefineAnalyzeDot[25];
Clear[aa];
Manipulate viewer for next set NN addition to area
(*tool to look at "Brillouin Zones" of the image.  Not true Brillouin Zones \
as they're not defined by Bragg planes - that wouldn't have meaning for \
pixels.*)
BZShower[set_] := Graphics[
 Table[{Line[
    Prepend[MakeTheDough[[Ri, 4]], MakeTheDough[[Ri, 4, -1]]]]}, {Ri, 2,
    set}]
 ~Join~
 {Polygon[MakeTheDough[[set, 4]]]}
 ~Join~
 Table[{Opacity[.1], White, Polygon[MakeTheDough[[2 ;; o, 4]]]}, {o, 2,
   set - 1, 1}]
 ]
```

```
BZShower[15](*unsuppress to view*);
Manipulate[{
 (*left pane*)
 Graphics[{
  Line[MakeTheDough[[2 ;;, 4]]],
  Rectangle[{MakeTheDough, w}, .0001],
  Disk[{q, w}, .0001],

  Table[
   Disk[{q, w}, .0001], {q, -MakeTheDough[[1, 1, 2]], zoom, 1}, {w, -zoom,
    zoom, 1}],
  Black, Polygon[MakeTheDough[[NN, 4]]],
  Opacity[.4], Polygon[MakeTheDough[[1 ;; NN - 1, 4]]]
  }, ImageSize -> {500, 500}],
 (*right pane*)
 Graphics[{
  Disk[{-zoom, zoom}, .0001],
  Disk[{zoom, -zoom}, .0001],
  Black, Polygon[MakeTheDough[[NN, 4]]],
  White, Polygon[MakeTheDough[[1 ;; NN - 1, 4]]]
  }, ImageSize -> {500, 500}],
 (*new area with placeholders*)
 Total[
  Abs[
   1 - ImageData[Binarize[
     Graphics[{
       Disk[{-zoom, zoom}, .0001],
       Disk[{zoom, -zoom}, .0001],
       Black, Polygon[MakeTheDough[[NN, 4]]],
       White, Polygon[MakeTheDough[[1 ;; NN - 1, 4]]]
       }, ImageSize -> {500, 500}],
     0.2]
    ]
   ],
  3] -
 (*subtract off placeholders*)
 Total[
  Abs[
   1 - ImageData[Binarize[
     Graphics[{
       Disk[{-zoom, zoom}, .0001],
       Disk[{zoom, -zoom}, .0001]
       }, ImageSize -> {500, 500}],
     0.2]
    ]
   ],
```

```
   3]
  }
 , {{NN, 5}, 1, Length[MakeTheDough], 1}, {{zoom, 5}, 1,
  Length[MakeTheDough - 1], 1}]
```

Define image set

Whole idea here is to load the set of images for the analysis so Mathematica will do all the work after you're done.

```
imgSetElems =
  10;(*this is the number of files to be analyzed, not including the radio \
correction images*)
```

For MAC

```
fileNames = {
   {"index", "symbol", "filepath"},
   {1, "img01",
    "/Users/benjaminyoung/Documents/BRAINPOWER/Physics/Surface Lab/Data \
Backup/2013/11 November/16 Nov - cold Ar sputter 1x7x2m w
LEED/i09.120.bmp"},
   {2, "img02",
    "/Users/benjaminyoung/Documents/BRAINPOWER/Physics/Surface Lab/Data \
Backup/2013/11 November/16 Nov - cold Ar sputter 1x7x2m w
LEED/i13.120.bmp"},
   {3, "img03",
    "/Users/benjaminyoung/Documents/BRAINPOWER/Physics/Surface Lab/Data \
Backup/2013/11 November/16 Nov - cold Ar sputter 1x7x2m w
LEED/i18.120.bmp"},
   {4, "img04",
    "/Users/benjaminyoung/Documents/BRAINPOWER/Physics/Surface Lab/Data \
Backup/2013/11 November/16 Nov - cold Ar sputter 1x7x2m w
LEED/i23.120.bmp"},
   {5, "img05",
    "/Users/benjaminyoung/Documents/BRAINPOWER/Physics/Surface Lab/Data \
Backup/2013/11 November/16 Nov - cold Ar sputter 1x7x2m w
LEED/i28.120.bmp"},
   {6, "img06",
    "/Users/benjaminyoung/Documents/BRAINPOWER/Physics/Surface Lab/Data \
Backup/2013/11 November/16 Nov - cold Ar sputter 1x7x2m w
LEED/i33.120.bmp"},
   {7, "img07",
    "/Users/benjaminyoung/Documents/BRAINPOWER/Physics/Surface Lab/Data \
Backup/2013/11 November/16 Nov - cold Ar sputter 1x7x2m w
LEED/i38.120.bmp"},
   {8, "img08",
    "/Users/benjaminyoung/Documents/BRAINPOWER/Physics/Surface Lab/Data \
Backup/2013/11 November/16 Nov - cold Ar sputter 1x7x2m w
LEED/i43.120.bmp"},
   {9, "img09",
```

```
   "/Users/benjaminyoung/Documents/BRAINPOWER/Physics/Surface Lab/Data \
Backup/2013/11 November/16 Nov - cold Ar sputter 1x7x2m w
LEED/i48.120.bmp"},
  {10, "img10",
   "/Users/benjaminyoung/Documents/BRAINPOWER/Physics/Surface Lab/Data \
Backup/2013/11 November/16 Nov - cold Ar sputter 1x7x2m w
LEED/i53.120.bmp"},
  {11, "img11",
   "/Users/byoung/Documents/Surface Lab/Data Backup/2013/06 \
June/04_June_Ne_1x6/i120-10.bmp"},
  {12, "img12",
   "/Users/byoung/Documents/Surface Lab/Data Backup/2013/06 \
June/04_June_Ne_1x6/i120-11.bmp"},
  {13, "img13",
   "/Users/byoung/Documents/Surface Lab/Data Backup/2013/06 \
June/04_June_Ne_1x6/i120-12.bmp"},
  {14, "img14",
   "/Users/byoung/Documents/Surface Lab/Data Backup/2013/06 \
June/04_June_Ne_1x6/i120-13.bmp"},
  {15, "img15",
   "/Users/byoung/Documents/Surface Lab/Data Backup/2013/06 \
June/04_June_Ne_1x6/i120-14.bmp"}
  };
darkFields = {
  {"index", "symbol", "filepath"},
  {1, "df01",
   "/Users/benjaminyoung/Documents/BRAINPOWER/Physics/Surface Lab/Data \
Backup/2013/11 November/16 Nov - cold Ar sputter 1x7x2m w LEED/i08.2.3.bmp"},
  {2, "df02",
   "/Users/benjaminyoung/Documents/BRAINPOWER/Physics/Surface Lab/Data \
Backup/2013/11 November/16 Nov - cold Ar sputter 1x7x2m w LEED/i12.2.3.bmp"},
  {3, "df03",
   "/Users/benjaminyoung/Documents/BRAINPOWER/Physics/Surface Lab/Data \
Backup/2013/11 November/16 Nov - cold Ar sputter 1x7x2m w LEED/i17.2.3.bmp"},
  {4, "df04",
   "/Users/benjaminyoung/Documents/BRAINPOWER/Physics/Surface Lab/Data \
Backup/2013/11 November/16 Nov - cold Ar sputter 1x7x2m w LEED/i22.2.3.bmp"},
  {5, "df05",
   "/Users/benjaminyoung/Documents/BRAINPOWER/Physics/Surface Lab/Data \
Backup/2013/11 November/16 Nov - cold Ar sputter 1x7x2m w LEED/i27.2.3.bmp"},
  {6, "df06",
   "/Users/benjaminyoung/Documents/BRAINPOWER/Physics/Surface Lab/Data \
Backup/2013/11 November/16 Nov - cold Ar sputter 1x7x2m w LEED/i32.2.3.bmp"},
  {7, "df07",
   "/Users/benjaminyoung/Documents/BRAINPOWER/Physics/Surface Lab/Data \
Backup/2013/11 November/16 Nov - cold Ar sputter 1x7x2m w LEED/i37.2.3.bmp"},
```

```
  {8, "df08",
   "/Users/benjaminyoung/Documents/BRAINPOWER/Physics/Surface Lab/Data \
Backup/2013/11 November/16 Nov - cold Ar sputter 1x7x2m w LEED/i42.2.3.bmp"},
  {9, "df09",
   "/Users/benjaminyoung/Documents/BRAINPOWER/Physics/Surface Lab/Data \
Backup/2013/11 November/16 Nov - cold Ar sputter 1x7x2m w LEED/i47.2.3.bmp"},
  {10, "df10",
   "/Users/benjaminyoung/Documents/BRAINPOWER/Physics/Surface Lab/Data \
Backup/2013/11 November/16 Nov - cold Ar sputter 1x7x2m w LEED/i52.2.3.bmp"},
  {11, "df11",
   "/Users/byoung/Documents/Surface Lab/Data Backup/LEED/2013/06 \
June/04_June_Ne_1x6/idf-10.bmp"},
  {12, "df12",
   "/Users/byoung/Documents/Surface Lab/Data Backup/LEED/2013/06 \
June/04_June_Ne_1x6/idf-11.bmp"},
  {13, "df13",
   "/Users/byoung/Documents/Surface Lab/Data Backup/LEED/2013/06 \
June/04_June_Ne_1x6/idf-12.bmp"},
  {14, "df14",
   "/Users/byoung/Documents/Surface Lab/Data Backup/LEED/2013/06 \
June/04_June_Ne_1x6/idf-13.bmp"},
  {15, "df15",
   "/Users/byoung/Documents/Surface Lab/Data Backup/LEED/2013/06 \
June/04_June_Ne_1x6/idf-14.bmp"}
 };
flatFields = {
  {"index", "symbol", "filepath"},
  {1, "ff01",
   "/Users/benjaminyoung/Documents/BRAINPOWER/Physics/Surface Lab/Data \
Backup/Pre Vostro220(2012) data/LEED/2013/05 \
May/15_sputter_anneal_Ar1x6/flatfield.bmp"},
  {2, "ff02",
   "/Users/benjaminyoung/Documents/BRAINPOWER/Physics/Surface Lab/Data \
Backup/Pre Vostro220(2012) data/LEED/2013/05 \
May/15_sputter_anneal_Ar1x6/flatfield.bmp"},
  {3, "ff03",
   "/Users/benjaminyoung/Documents/BRAINPOWER/Physics/Surface Lab/Data \
Backup/Pre Vostro220(2012) data/LEED/2013/05 \
May/15_sputter_anneal_Ar1x6/flatfield.bmp"},
  {4, "ff04",
   "/Users/benjaminyoung/Documents/BRAINPOWER/Physics/Surface Lab/Data \
Backup/Pre Vostro220(2012) data/LEED/2013/05 \
May/15_sputter_anneal_Ar1x6/flatfield.bmp"},
  {5, "ff05",
   "/Users/benjaminyoung/Documents/BRAINPOWER/Physics/Surface Lab/Data \
Backup/Pre Vostro220(2012) data/LEED/2013/05 \
```

```
May/15_sputter_anneal_Ar1x6/flatfield.bmp"},
  {6, "ff06",
   "/Users/benjaminyoung/Documents/BRAINPOWER/Physics/Surface Lab/Data \
Backup/Pre Vostro220(2012) data/LEED/2013/05 \
May/15_sputter_anneal_Ar1x6/flatfield.bmp"},
  {7, "ff07",
   "/Users/benjaminyoung/Documents/BRAINPOWER/Physics/Surface Lab/Data \
Backup/Pre Vostro220(2012) data/LEED/2013/05 \
May/15_sputter_anneal_Ar1x6/flatfield.bmp"},
  {8, "ff08",
   "/Users/benjaminyoung/Documents/BRAINPOWER/Physics/Surface Lab/Data \
Backup/Pre Vostro220(2012) data/LEED/2013/05 \
May/15_sputter_anneal_Ar1x6/flatfield.bmp"},
  {9, "ff09",
   "/Users/benjaminyoung/Documents/BRAINPOWER/Physics/Surface Lab/Data \
Backup/Pre Vostro220(2012) data/LEED/2013/05 \
May/15_sputter_anneal_Ar1x6/flatfield.bmp"},
  {10, "ff10",
   "/Users/benjaminyoung/Documents/BRAINPOWER/Physics/Surface Lab/Data \
Backup/Pre Vostro220(2012) data/LEED/2013/05 \
May/15_sputter_anneal_Ar1x6/flatfield.bmp"},
  {11, "ff11",
   "/Users/byoung/Documents/Surface Lab/Data Backup/LEED/2013/05 \
May/15_sputter_anneal_Ar1x6/flatfield.bmp"},
  {12, "ff12",
   "/Users/byoung/Documents/Surface Lab/Data Backup/LEED/2013/05 \
May/15_sputter_anneal_Ar1x6/flatfield.bmp"},
  {13, "ff13",
   "/Users/byoung/Documents/Surface Lab/Data Backup/LEED/2013/05 \
May/15_sputter_anneal_Ar1x6/flatfield.bmp"},
  {14, "ff14",
   "/Users/byoung/Documents/Surface Lab/Data Backup/LEED/2013/05 \
May/15_sputter_anneal_Ar1x6/flatfield.bmp"},
  {15, "ff15",
   "/Users/byoung/Documents/Surface Lab/Data Backup/LEED/2013/05 \
May/15_sputter_anneal_Ar1x6/flatfield.bmp"}
 };
For PC
(*fileNames="index"  "symbol"        "filepath"
1        "img01"         "C:\\Data\\LEED\\2013\\03 March\\4Mar - Ne 1x6 5m\\i2.1-
image.bmp"
2        "img02"         "C:\\Data\\LEED\\2013\\03 March\\4Mar - Ne 1x6 5m\\i3.1-
image.bmp"
3        "img03"         "C:\\Data\\LEED\\2013\\03 March\\4Mar - Ne 1x6 5m\\i4.1-
image.bmp"
4        "img04"         "C:\\Data\\LEED\\2013\\03 March\\4Mar - Ne 1x6 5m\\i5.1-
```

```
image.bmp"
5	"img05"	"C:\\Data\\LEED\\2013\\03 March\\4Mar - Ne 1x6 5m\\i6.1-
image.bmp"
6	"img06"	"C:\\Data\\LEED\\2013\\03 March\\4Mar - Ne 1x6 5m\\i7.1-
image.bmp"
7	"img07"	"C:\\Data\\LEED\\2013\\03 March\\4Mar - Ne 1x6 5m\\i1.1-
image.bmp"
8	"img08"	"C:\\Data\\LEED\\2013\\03 March\\4Mar - Ne 1x6 5m\\i8.1-
image.bmp"
9	"img09"	"C:\\Data\\LEED\\2013\\03 March\\4Mar - Ne 1x6 5m\\i1.1-
image.bmp"
10	"img10"	"C:\\Data\\LEED\\2013\\03 March\\4Mar - Ne 1x6 5m\\i1.1-
image.bmp"

;
darkFields="index"	"symbol"	"filepath"
1	"df01"	"C:\\Data\\LEED\\2013\\03 March\\4Mar - Ne 1x6 5m\\i2.0-df.bmp"
2	"df02"	"C:\\Data\\LEED\\2013\\03 March\\4Mar - Ne 1x6 5m\\i3.0-df.bmp"
3	"df03"	"C:\\Data\\LEED\\2013\\03 March\\4Mar - Ne 1x6 5m\\i4.0-df.bmp"
4	"df04"	"C:\\Data\\LEED\\2013\\03 March\\4Mar - Ne 1x6 5m\\i5.0-df.bmp"
5	"df05"	"C:\\Data\\LEED\\2013\\03 March\\4Mar - Ne 1x6 5m\\i6.0-df.bmp"
6	"df06"	"C:\\Data\\LEED\\2013\\03 March\\4Mar - Ne 1x6 5m\\i7.0-df.bmp"
7	"df07"	"C:\\Data\\LEED\\2013\\03 March\\4Mar - Ne 1x6 5m\\i1.0-df.bmp"
8	"df08"	"C:\\Data\\LEED\\2013\\03 March\\4Mar - Ne 1x6 5m\\i8.0-df.bmp"
9	"df09"	"C:\\Data\\LEED\\2013\\03 March\\4Mar - Ne 1x6 5m\\i10.0-df.bmp"
10	"df10"	"C:\\Data\\LEED\\2013\\03 March\\4Mar - Ne 1x6 5m\\i10.0-df.bmp"

;
flatFields="index"	"symbol"	"filepath"
1	"ff01"	"C:\\Data\\LEED\\2013\\03 March\\4Mar - Ne 1x6 5m\\flatfield.bmp"
2	"ff02"	"C:\\Data\\LEED\\2013\\03 March\\4Mar - Ne 1x6 5m\\flatfield.bmp"
3	"ff03"	"C:\\Data\\LEED\\2013\\03 March\\4Mar - Ne 1x6 5m\\flatfield.bmp"
4	"ff04"	"C:\\Data\\LEED\\2013\\03 March\\4Mar - Ne 1x6 5m\\flatfield.bmp"
5	"ff05"	"C:\\Data\\LEED\\2013\\03 March\\4Mar - Ne 1x6 5m\\flatfield.bmp"
6	"ff06"	"C:\\Data\\LEED\\2013\\03 March\\4Mar - Ne 1x6 5m\\flatfield.bmp"
7	"ff07"	"C:\\Data\\LEED\\2013\\03 March\\4Mar - Ne 1x6 5m\\flatfield.bmp"
8	"ff08"	"C:\\Data\\LEED\\2013\\03 March\\4Mar - Ne 1x6 5m\\flatfield.bmp"
9	"ff09"	"C:\\Data\\LEED\\2013\\03 March\\4Mar - Ne 1x6 5m\\flatfield.bmp"
10	"ff10"	"C:\\Data\\LEED\\2013\\03 March\\4Mar - Ne 1x6 5m\\flatfield.bmp"

;*)
Define a list of just file names, no headers or placeholders
namedFiles = fileNames[[2 ;; imgSetElems + 1]];
namedDarks = darkFields[[2 ;; imgSetElems + 1]];
namedFlats = flatFields[[2 ;; imgSetElems + 1]];
Load Image Set, Radio-correct
```

```
viewCorrector[n_] := Block[{dFielder, fFielder, rawImg, rcImg},
  dFielder = ImageData[Import[namedDarks[[n, 3]]]][[All, All, 1]];
  fFielder = ImageData[Import[namedFlats[[n, 3]]]][[All, All, 1]];
  rawImg = ImageData[Import[namedFiles[[n, 3]]]][[All, All, 1]];
  rcImg = Clip[(rawImg) - dFielder, {0, 2}];
  Image[rcImg]]
```

Define "eyeballed" spot centers

```
viewCorrector[1](*unsuppress to view*);
```

For the first image in the series, right click on the image above, select get indices, select each spot center left to right, top to bottom, then Ctrl+C, then paste into the eyeballedCenters symbol below. After the first image the thing takes care of itself and you don't need to repeat this procedure.

```
eyeballedCenters = {{240, 492}, {243, 641}, {242, 789}, {451, 342}, {450,
    494}, {454, 786}, {458, 938}, {660, 491}, {661, 637}, {666, 786}};
```

Build SPA-LEED

Build the spot center corrector

Well-defined dots, like in the picture of a clean surface, are only about 20 pixels wide to the point where the background stars to really fall, doing the analysis out to r=15 is generally more than enough in practice.

```
Maxxor[dot_, r_] := Block[{create, searchmax, getloc, report},
  create =
   Table[(*iterate over all possible dot centers in the inputted radius*)

    Total[(*add up the total dot intensity at each radius*)

      Table[(*iterate down the list of NN sets*)

       Total[(*add up the values of the pixels*)

         Extract[(*get the pixel values from the image that correspond to \
the NN sets*)
          dotImage,

          Map[(*reassign the NN info to refer specifically to the dot \
inputted*)
           {dot[[1]] + k, dot[[2]] + l} + # &,
           MakeTheDough[[j, 4]]
           ](*close Map[]*)
          ](*close Extract[]*)
         \
](*close Total[]*)/Length[MakeTheDough[[j, 4]]]*
        MakeTheDough[[j,
         5]],(*average and multiply by area gained in that NNset*)
        {j,
         3, Length[MakeTheDough]}](*close Table[]*)
      ](*close Total[]*)+
```

```
    Extract[dotImage,
     Map[{dot[[1]] + k, dot[[2]] + l} + # &,
      MakeTheDough[[2,
       4]]]],(*add the intensity of the dot center point*)
    {k, -r,
    r}, {l, -r, r}];(*close Table[], finish create symbol*)

  searchmax = Max[create];(*find the max intensity center point possibility*)

   getloc =
   Position[create,
    searchmax];(*find the location of the above line*)
  {searchmax,
   dot + {-r, -r} +
    getloc[[1,
     1 ;;
      2]] + {-1, -1}}](*report the intensity of the dot and the location in \
the real image, close Block[]*)
```

Correct the spot centers

This can be used for troubleshooting, but it calls the dotImage symbol, so you'll need to copy that from the final analysis sequence if you want to use this. In practice it is only necessary when the output calls into question the program's ability to properly track the dot between LEED events.

```
eyeballedCenters(*unsuppress to show result*);
For[bb = 1, bb < Length[eyeballedCenters] + 1, bb++,
 eyeballedCenters[[bb]] =
  Maxxor[eyeballedCenters[[bb]], 10][[
   2]]]; Clear[bb](*looks about the suggested dot center for the center of \
the maximum spot containing that location*)
(*looks like you don't need the \
full radius of the NN analysis to find the dot center.  play more with this \
later and on less well defined dots than clean*)
```

Generate SPA for each corrected spot

```
Displayor[dot_, r_] := Block[{create, insertcenter, normalize, intensity},
  create =
   Table[(*iterate down the list of NN sets*)

    Total[(*add up the values of the pixels*)

      Extract[(*get the pixel values from the image that correspond to the NN \
sets*)
       dotImage,
       Map[(*reassign the NN info to refer specifically to the dot inputted*)

             dot + # &,
        MakeTheDough[[m, 4]]
```

```
      ](*close Map[]*)
     ](*close Extract[]*)
    ](*close Total[]*)/
   Length[MakeTheDough[[m, 4]]],(*average dot in that NNset*)
  {m, 3,
   Length[MakeTheDough]}];(*close Table[]*)

 insertcenter =
  Prepend[create,
   Extract[dotImage, Map[dot + # &, MakeTheDough[[2, 4]]]][[
    1]]];(*insert the center pixel intensity*)

 normalize =
  insertcenter/insertcenter[[1]];(*scale the set to the center pixel*)

 intensity =
  insertcenter[[
     1]] p (1/
     2 (MakeTheDough[[3,
       2]]))^2(*center intensity times area of circle to half r1*)
   +
   Total[
    Table[
     insertcenter[[n + 1]](*annulus Subscript[r, i]
       intensity times annulus Subscript[r, n]±1/2Subscript[Dr, n±1]*)

      p ((MakeTheDough[[n + 2,
          2]] + (1/
           2 (MakeTheDough[[n + 3, 2]] -
             MakeTheDough[[n + 2, 2]])))^2 - (MakeTheDough[[n + 2,
          2]] - (1/
           2 (MakeTheDough[[n + 2, 2]] - MakeTheDough[[n + 1, 2]])))^2),
     {n, 1,
      Length[insertcenter] -
       3}](*close Table[]*)
    ](*close Total[]*)
   + (p \
(MakeTheDough[[-1,
        2]]^2 - (MakeTheDough[[-1,
          2]] - (1/
           2 (MakeTheDough[[-1, 2]] -
             MakeTheDough[[-2,
              2]])))^2)) insertcenter[[-1]](*last half annulus as defined \
in the Table[] immediately above*)
   -
   p MakeTheDough[[-1,
```

```
    2]]^2 insertcenter[[-1]];(*assume background level has been reached at \
periphery of analysis spot size and subtract intensity equal to that times \
the size of the disk defined by the analysis spot*)

  Append[Table[{MakeTheDough[[o + 1, 2]], insertcenter[[o]],
    insertcenter[[o]]/insertcenter[[1]],
    insertcenter[[o]]/insertcenter[[-1]]}, {o, 1,
    Length[MakeTheDough] - 1}], {intensity}](*report*)
  ](*close Block[]*)
```

Lean, Mean, No Foolin'

Don't change anything unless you've already done so in the constituent parts above, and don't run it unless you've already gone through the constituent parts above for the first image of the set to ensure everything is on the up and up.

```
AnalysisBlock =
  For[cc = 1,
   cc < imgSetElems + 1,
   cc++,
   Clear[dotImage, spaTable];
   dotImage = Clip[
    (ImageData[
       Import[
        namedFiles[[cc, 3]]
        ](*close Import[image]*)
       ](*close ImageData[image]*)[[All,
      All, 1]](*discard extraneous channels*)-
     ImageData[
      Import[
       namedDarks[[cc, 3]]
       ](*close Import[darkfield]*)
      ](*close ImageData[
     darkfield]*)[[All, All, 1]](*discard extraneous channels*))(**
    ImageData[
    Import[
    namedFlats[[cc,3]]
    ](*close Import[flatfield]*)
    ](*close ImageData[flatfield]*)[[All,
    All,1]](*discard extraneous channels*)*),
    {0, 2}];(*apply and close Clip[]*)

   For[dd = 1, dd < Length[eyeballedCenters] + 1, dd++,
    eyeballedCenters[[dd]] = Maxxor[eyeballedCenters[[dd]], 15][[2]]];
   Clear[dd];
   spaTable =
    Table[Displayor[eyeballedCenters[[p]], 25], {p, Length[eyeballedCenters]}];
   AppendTo[saveData, spaTable];
   ];(*runs the analysis over the rest of the images in the list*)
```

```
Clear[cc];(*housekeeping*)
Manipulate viewer for SPA of individual dots
The analysis of even a single image produces a lot of data.  More data than can fit on two screens with a reasonably sized typeface.  This will allow the user to view the analysis for all events of a single dot, and to discriminate what range of events to include in the visualization.  It also displays the total intensity of the spot as a function of event index and offers a few choices for massaging the data (raw, backgrounds...).  Be sure to delete the output before running a new set of images through the system.  The output of Manipulate[] is dynamic, so you will likely get a mess of error messages as soon as you clear the memory.
Manipulate[
 Row[{
  ListPlot[(*for displaying the dot analysis and defining set*)

   saveData[[iEvent ;; fEvent, dIndex,
    1 ;; Position[(saveData[[1, 1, 1 ;; -2]])^2, radiusLimit^2][[1, 1]], {1,
     1 + rawNorm}]],
   PlotRange -> All,
   Frame -> True,
   AxesOrigin -> {0, 0},
   FrameLabel -> {"Radius (pixels from center)",
     Which[rawNorm == 1, "Raw Intensity", rawNorm == 2,
      "Intensity (relative to central pixel)", rawNorm == 3,
      "Intensity (relative to background)"], "SPA-LEED: Spot Profiles"},
   ImageSize -> {500, 300},
   Epilog ->
    Inset[
     Panel[
      Grid[
       MapIndexed[{Graphics[{ColorData[1, First@#2], Thick,
            Line[{{0, 0}, {1, 0}}]}, AspectRatio -> .1,
           ImageSize -> 20], #1} &, Table[i - 1, {i, iEvent, fEvent}]]]],
     Offset[{-2, -2}, Scaled[{1, 1}]], {Right, Top}]
   ](*close ListPlot[]*),
  ListLinePlot[(*for displaying the set analysis*)
   Table[
    {i - 1,
     saveData[[i, dIndex, -1]][[1]]/
      Which[
       rawNorm == 1, 1,
       rawNorm == 2, saveData[[i, dIndex, 1, 2]],
       rawNorm == 3,
       saveData[[i, dIndex,
        Position[(saveData[[1, 1, 1 ;; -2]])^2, radiusLimit^2][[1, 1]], 2]]
       ]
```

```
    }, {i, iEvent, fEvent}],
   PlotRange -> All,
   Frame -> True,
   AxesOrigin -> {0, 0},
   FrameLabel -> {"Event Index",
     Which[rawNorm == 1, "Raw Intensity", rawNorm == 2,
      "Intensity (relative to central pixel)", rawNorm == 3,
      "Intensity (relative to background)"],
     "SPA-LEED: Total Spot Intensity"}, ImageSize -> {500, 300}
   ]
  }](*close the Column*),
 {{iEvent, 1, "Initial Event Index"}, 1, Length[saveData], 1},
 {{fEvent, 3, "Final Event Index"}, 1, Length[saveData], 1},
 {{rawNorm, 1, "now viewing"}, {1 -> "raw intensity",
  2 -> "normalized to center", 3 -> "normalized to background level"},
  Setter},
 {{dIndex, Length[saveData[[1]]], "Dot Index"}, 1, Length[saveData[[1]]],
  1},
 {{radiusLimit, saveData[[1, 1, -2, 1]], "Max Radius"}, 1,
  saveData[[1, 1, -2, 1]], 1}
 ](*unsuppress to view*);
```

These next two lines repackage the data into a form that will lay the results off into an excel file: One sheet per analyzed image, top row is pixel radii, subsequent rows correspond to dots analyzed.

```
justTheGun =
  Table[Insert[saveData[[n, All, 1 ;; -2, 2]], saveData[[1, 1, All, 1]],
    1], {n, Length[saveData]}];
Export["SPA-LEED.xlsx", justTheGun]
"SPA-LEED.xlsx"
```

And these next two lines repackage the data into a form that will lay the results off into another excel file: Only one sheet, columns are intensities of analyzed dot, rows correspond to the event index (ie, all the intensities for the (0,1) spot might be in column 3 with the clean intensity at the top).

```
intnums =
  Transpose[
   Table[Flatten[saveData[[All, n, -1]]], {n, Length[saveData[[1]]]}]];
Export["16novintegrations.xlsx", intnums]
```

APPENDIX C: Mathematica Simulation of Ion Bombardment

This sample Mathematica work develops the ion bombardment simulation. Appropriate output sections have been incorporated into the body of the dissertation and are suppressed here. The more useful version of this is on file in the URI Surface Lab as a Mathematica notebook.

Develop and create the map of nearest neighbors
This is the standard map that, when executed in the creation subsection, creates a table. First levelspec is nearest neighbor set (first element at levelspec 1 is a header), second level is a list of: {set index, distance from center element, multiplicity of elements at this distance, {location(s) of element(s)}}

```
Clear["Global`*"]
defineAnalyzeDot[r_(*search radius*)] :=
 Block[{NNDistanceSample, NNDistancesR, NNDistancesNR, indexlist, roughlocs,
   locations, sortedlocationindices, sortedlocations, grumpy, scaledgrumpy,
   result},
  (*creates a table (2n+1 x 2n+1 crystal) each element of which is the \
squared distance in index space of the element from the argument (i,j),
  addition of the 1/Sqrt[2]
  factor maps index space to real space with scaling of lattice parameter, a=
  3.52Þ *)

  NNDistanceSample =
   Table[{a, b, (1/Sqrt[2] a)^2 + (b)^2}, {a, -r, r}, {b, -r, r}];
  (*creates a list in ascending order of the distances from center to each \
set of nearest neighbors, redundant*)

  NNDistancesR = Sort[Flatten[NNDistanceSample, 1], #1[[3]] < #2[[3]] &];
  (*delete redundant distances in the last list,
  output list of unique distances short to long*)

  NNDistancesNR =
   DeleteDuplicates[NNDistancesR, #1[[3]] == #2[[3]] &][[All, 3]];
  (*nearest neighbor set index, center is index 0*)

  indexlist = Table[c - 1, {c, Length[NNDistancesNR]}];
  (*indices for each distance*)

  locations =
   Table[Select[
     Flatten[NNDistanceSample, 1], #[[3]] == NNDistancesNR[[d]] &][[All,
    1 ;; 2]], {d, Length[NNDistancesNR]}];
  (*finds the shortest path between the points at each distance,
  which defines a non self-intersecting polygon,
```

```
 but the output is a list of indices for the ordering*)

 sortedlocationindices =
  Table[FindShortestTour[locations[[e]]][[2]], {e, Length[locations]}];
 (*use ordering indices from previous step to reorder the locations*)

 sortedlocations =
  Table[locations[[f, g]], {f, Length[sortedlocationindices]}, {g,
    sortedlocationindices[[f]]}];
 (*package output*)
 result = Prepend[
   Table[
    {indexlist[[h]], Sqrt[NNDistancesNR][[h]], Length[locations[[h]]],
     sortedlocations[[h]]},
    {h, Flatten[Position[NNDistancesNR, r^2]][[1]]}], {{"search radius", r},
    "radius", "#Î", "pixel indices"}]
 ]
makeTheDough = defineAnalyzeDot[30];
Develop sputtering efficiency
Calculate the focus factor (MAC)
The focus factor is the fraction of the sputtering target that's actually contained in the
nickel surface.  This is hard coded because it ought not change unless the sample
holder has been replaced.
focusFactor =
 Block[{sNumbers, shNumbers, rSample, cSample, limitList, focusFactors,
   massFocusFactors},
  sNumbers =(* turns the image into numbers *)
   ImageData[
    Import[
     "/Users/benjaminyoung/Documents/BRAINPOWER/Physics/Surface \
Lab/Library/Photos and Diagrams/photos/sample holder/sample without holder in \
silhouette (BW).bmp"]];
  shNumbers =(* turns the image into numbers *)
   ImageData[
    Import[
     "/Users/benjaminyoung/Documents/BRAINPOWER/Physics/Surface \
Lab/Library/Photos and Diagrams/photos/sample holder/sample with holder in \
silhouette (BW).bmp"]];
  rSample = (498 -
     282);(*compute the height of the sample holder (unit sh above)*)

  cSample = rSample/2 + 282;(*compute the center of sample holder*)

  limitList =
   Clip[Round[Table[cSample - (a rSample), {a, {1, 1.5, 2}}]], {1,
     282}];(*figure out target height for each focus*)
```

```
  focusFactors =
   Total[sNumbers, 2]/Table[Total[shNumbers[[i ;;]], 2] // N, {i, limitList}];
  massFocusFactors =
   Join[focusFactors(*39.948/58.70*), focusFactors(*20.179/
    58.70*)]];(*ratios*)(*unsuppress to show *)
```

Calculate the focus factor (PC)

The focus factor is the fraction of the sputtering target that's actually contained in the nickel surface. This is hard coded because it ought not change unless the sample holder has been replaced.

```
focusFactor =
 Block[{sNumbers, shNumbers, rSample, cSample, limitList, focusFactors,
   massFocusFactors},
  sNumbers =(* turns the image into numbers *)
   ImageData[
    Import[
     "E:\\BRAINPOWER\\Physics\\Surface Lab\\Library\\Photos and \
Diagrams\\photos\\sample holder\\sample without holder in silhouette \
(BW).bmp"]];
  shNumbers =(* turns the image into numbers *)
   ImageData[
    Import[
     "E:\\BRAINPOWER\\Physics\\Surface Lab\\Library\\Photos and \
Diagrams\\photos\\sample holder\\sample with holder in silhouette \
(BW).bmp"]];
  rSample = (498 -
     282);(*compute the height of the sample holder (unit sh above)*)

  cSample = rSample/2 + 282;(*compute the center of sample holder*)

  limitList =
   Clip[Round[Table[cSample - (a rSample), {a, {1, 1.5, 2}}]], {1,
     282}];(*figure out target height for each focus*)

  focusFactors =
   Total[sNumbers, 2]/Table[Total[shNumbers[[i ;;]], 2] // N, {i, limitList}];
  massFocusFactors = Join[
    focusFactors(*39.948/
    58.70 this is the mass ratio which appears not appropriate to include*),
     focusFactors(*20.179/58.70*)
    ]](*ratios*)(*unsuppress to show *);
```

Log of sputtering parameters

The sample current developed during sputtering falls away from the initial maximum in an exponential fashion, nicely described by the relation:

I(t) = Subscript[C, 0] + Subscript[C, 1] E^(-Subscript[C, 2] t)

We keep a running tab of the fit coefficients, calculated with the Igor Pro software package, below.
Argon

```
ArParms = {{"argon", , , , , , ,}, {"row", "Angle", "Beam Energy", "focus",
    "focus factor", "coef0", "coef1", "coef2"},
   {3, 90, "5x5", 500, "CCW", focusFactor[[1]], 8.1268, 3.7162, 0.0014306},
   {4, 90, "5x5", 500, "cal", focusFactor[[2]], 5.7644, 2.95, 0.0011771},
   {5, 90, "5x5", 1000, "CCW", focusFactor[[1]], 1, 2, 3},
   {6, 90, "5x5", 1000, "cal", focusFactor[[2]], 1, 2, 3},
   {7, 90, "1x5", 500, "CCW", focusFactor[[1]], 1, 2, 3},
   {8, 90, "1x5", 500, "cal", focusFactor[[2]], 1.542, 2.1317, 0.0014872},
   {9, 90, "1x5", 1000, "CCW", focusFactor[[1]], 1, 2, 3},
   {10, 90, "1x5", 1000, "cal", focusFactor[[2]], 1, 2, 3},
   {11, 90, "5x6", 500, "CCW", focusFactor[[1]], 1, 2, 3},
   {12, 90, "5x6", 500, "cal", focusFactor[[2]], 0.71481, 0.6078, 0.0014218},
   {13, 90, "5x6", 1000, "CCW", focusFactor[[1]], 1, 2, 3},
   {14, 90, "5x6", 1000, "cal", focusFactor[[2]], 1, 2, 3},
   {15, 90, "1x6", 500, "CCW", focusFactor[[1]], 1, 2, 3},
   {16, 90, "1x6", 500, "cal", focusFactor[[2]], 0.14874, 0.083713, 0.0018791},
   {17, 90, "1x6", 1000, "CCW", focusFactor[[1]], 1, 2, 3},
   {18, 90, "1x6", 1000, "cal", focusFactor[[2]], 1, 2, 3},
   {19, 80, "5x5", 500, "CCW", focusFactor[[1]], 8.1583, 4.7609, 0.0012659},
   {20, 80, "5x5", 500, "cal", focusFactor[[2]], 5.7644, 2.95, 0.0011771},
   {21, 80, "5x5", 1000, "CCW", focusFactor[[1]], 1, 2, 3},
   {22, 80, "5x5", 1000, "cal", focusFactor[[2]], 1, 2, 3},
   {23, 80, "1x5", 500, "CCW", focusFactor[[1]], 1, 2, 3},
   {24, 80, "1x5", 500, "cal", focusFactor[[2]], 1, 2, 3},
   {25, 80, "1x5", 1000, "CCW", focusFactor[[1]], 1, 2, 3},
   {26, 80, "1x5", 1000, "cal", focusFactor[[2]], 1, 2, 3},
   {27, 80, "5x6", 500, "CCW", focusFactor[[1]], 1, 2, 3},
   {28, 80, "5x6", 500, "cal", focusFactor[[2]], 1, 2, 3},
   {29, 80, "5x6", 1000, "CCW", focusFactor[[1]], 1, 2, 3},
   {30, 80, "5x6", 1000, "cal", focusFactor[[2]], 1, 2, 3},
   {31, 80, "1x6", 500, "CCW", focusFactor[[1]], 1, 2, 3},
   {32, 80, "1x6", 500, "cal", focusFactor[[2]], 1, 2, 3},
   {33, 80, "1x6", 1000, "CCW", focusFactor[[1]], 1, 2, 3},
   {34, 80, "1x6", 1000, "cal", focusFactor[[2]], 1, 2, 3},
   {35, 70, "5x5", 500, "CCW", focusFactor[[1]], 7.933, 0.83, 0.0014173},
   {36, 70, "5x5", 500, "cal", focusFactor[[2]], 5.7644, 2.95, 0.0011771},
   {37, 70, "5x5", 1000, "CCW", focusFactor[[1]], 1, 2, 3},
   {38, 70, "5x5", 1000, "cal", focusFactor[[2]], 1, 2, 3},
   {39, 70, "1x5", 500, "CCW", focusFactor[[1]], 1, 2, 3},
   {40, 70, "1x5", 500, "cal", focusFactor[[2]], 1, 2, 3},
   {41, 70, "1x5", 1000, "CCW", focusFactor[[1]], 1, 2, 3},
   {42, 70, "1x5", 1000, "cal", focusFactor[[2]], 1, 2, 3},
```

```
  {43, 70, "5x6", 500, "CCW", focusFactor[[1]], 1, 2, 3},
  {44, 70, "5x6", 500, "cal", focusFactor[[2]], 1, 2, 3},
  {45, 70, "5x6", 1000, "CCW", focusFactor[[1]], 1, 2, 3},
  {46, 70, "5x6", 1000, "cal", focusFactor[[2]], 1, 2, 3},
  {47, 70, "1x6", 500, "CCW", focusFactor[[1]], 1, 2, 3},
  {48, 70, "1x6", 500, "cal", focusFactor[[2]], 1, 2, 3},
  {49, 70, "1x6", 1000, "CCW", focusFactor[[1]], 1, 2, 3},
  {50, 70, "1x6", 1000, "cal", focusFactor[[2]], 1, 2, 3},
  {51, 20, "1x7", 500, "cal", focusFactor[[2]], 0.0422615, 0.0109332,
   1/194.164},
  {52, 20, "1x7", 1000, "CCW", focusFactor[[1]], 1, 2, 3},
  {53, 20, "1x7", 1000, "cal", focusFactor[[2]], 1, 2, 3},
  {54, 20, "2x7", 500, "cal", focusFactor[[2]], 0.0400502, 0.00805818,
   1/158.889},
  {55, 20, "2x7", 1000, "CCW", focusFactor[[1]], 1, 2, 3},
  {56, 20, "2x7", 1000, "cal", focusFactor[[2]], 1, 2, 3}
  };
Neon
NeParms = {{"neon", , , , , , ,}, {"row", "Angle", "pressure", "Beam Energy",
   "focus", "focus factor", "coef0", "coef1", "coef2"},
  {3, 90, "5x5", 500, "CCW", focusFactor[[4]], 1, 2, 3},
  {4, 90, "5x5", 500, "cal", focusFactor[[5]], 1, 2, 3},
  {5, 90, "5x5", 1000, "CCW", focusFactor[[4]], 13.237, 9.8398, 0.0017931},
  {6, 90, "5x5", 1000, "cal", focusFactor[[5]], 9.1182, 7.719, 0.0028427},
  {7, 90, "1x5", 500, "CCW", focusFactor[[4]], 1, 2, 3},
  {8, 90, "1x5", 500, "cal", focusFactor[[5]], 1, 2, 3},
  {9, 90, "1x5", 1000, "CCW", focusFactor[[4]], 1, 2, 3},
  {10, 90, "1x5", 1000, "cal", focusFactor[[5]], 2.3956, 3.5922, 0.0022396},
  {11, 90, "5x6", 500, "CCW", focusFactor[[4]], 1, 2, 3},
  {12, 90, "5x6", 500, "cal", focusFactor[[5]], 1, 2, 3},
  {13, 90, "5x6", 1000, "CCW", focusFactor[[4]], 1.2733, 0.73985,
   0.0034349},
  {14, 90, "5x6", 1000, "cal", focusFactor[[5]], 1.1493, 0.78256, 0.002184},
  {15, 90, "1x6", 500, "CCW", focusFactor[[4]], 1, 2, 3},
  {16, 90, "1x6", 500, "cal", focusFactor[[5]], 0.17677, 0.10626,
   0.0015169},
  {17, 90, "1x6", 1000, "CCW", focusFactor[[4]], 0.24888, 0.13044, 0.0023371},
  {18, 90, "1x6", 1000, "cal", focusFactor[[5]], 1, 2, 3},
  {19, 80, "5x5", 500, "CCW", focusFactor[[4]], 1, 2, 3},
  {20, 80, "5x5", 500, "cal", focusFactor[[5]], 1, 2, 3},
  {21, 80, "5x5", 1000, "CCW", focusFactor[[4]], 1, 2, 3},
  {22, 80, "5x5", 1000, "cal", focusFactor[[5]], 1, 2, 3},
  {23, 80, "1x5", 500, "CCW", focusFactor[[4]], 1, 2, 3},
  {24, 80, "1x5", 500, "cal", focusFactor[[5]], 1, 2, 3},
  {25, 80, "1x5", 1000, "CCW", focusFactor[[4]], 1, 2, 3},
  {26, 80, "1x5", 1000, "cal", focusFactor[[5]], 1, 2, 3},
```

```
  {27, 80, "5x6", 500, "CCW", focusFactor[[4]], 1, 2, 3},
  {28, 80, "5x6", 500, "cal", focusFactor[[5]], 1, 2, 3},
  {29, 80, "5x6", 1000, "CCW", focusFactor[[4]], 1, 2, 3},
  {30, 80, "5x6", 1000, "cal", focusFactor[[5]], 1, 2, 3},
  {31, 80, "1x6", 500, "CCW", focusFactor[[4]], 1, 2, 3},
  {32, 80, "1x6", 500, "cal", focusFactor[[5]], 1, 2, 3},
  {33, 80, "1x6", 1000, "CCW", focusFactor[[4]], 0.24049, 0.075196,
  0.0019235},
  {34, 80, "1x6", 1000, "cal", focusFactor[[5]], 1, 2, 3},
  {35, 70, "5x5", 500, "CCW", focusFactor[[4]], 1, 2, 3},
  {36, 70, "5x5", 500, "cal", focusFactor[[5]], 1, 2, 3},
  {37, 70, "5x5", 1000, "CCW", focusFactor[[4]], 1, 2, 3},
  {38, 70, "5x5", 1000, "cal", focusFactor[[5]], 1, 2, 3},
  {39, 70, "1x5", 500, "CCW", focusFactor[[4]], 1, 2, 3},
  {40, 70, "1x5", 500, "cal", focusFactor[[5]], 1, 2, 3},
  {41, 70, "1x5", 1000, "CCW", focusFactor[[4]], 1, 2, 3},
  {42, 70, "1x5", 1000, "cal", focusFactor[[5]], 1, 2, 3},
  {43, 70, "5x6", 500, "CCW", focusFactor[[4]], 1, 2, 3},
  {44, 70, "5x6", 500, "cal", focusFactor[[5]], 1, 2, 3},
  {45, 70, "5x6", 1000, "CCW", focusFactor[[4]], 1, 2, 3},
  {46, 70, "5x6", 1000, "cal", focusFactor[[5]], 1, 2, 3},
  {47, 70, "1x6", 500, "CCW", focusFactor[[4]], 1, 2, 3},
  {48, 70, "1x6", 500, "cal", focusFactor[[5]], 1, 2, 3},
  {49, 70, "1x6", 1000, "CCW", focusFactor[[4]], 1, 2, 3},
  {50, 70, "1x6", 1000, "cal", focusFactor[[5]], 1, 2, 3},
  };
```

Define the "ML removed" function

The sputter efficiency is not constant. Early sputtering generates a higher current on the sample and we should like to account for this as we develop machinery to model the damage in increments. Integrate the current fit function over some time range, scale it by the focus factor since not all ions contributing to the current strike the crystal, and divide by approximate number of atoms in the crystal surface to estimate the sputter yield as colliding ions per surface unit cell. This is essentially the number of monolayers removed for the time range. We'll use it to determine the number of collisions later, so it must apply to a crystal of arbitrary size.

```
iExpPerS[t0_, t1_, spurameter_] := spurameter[[-4]]*ëô
òSubsuperscriptBox[ôÙê, ôt0ê,
   ôt1ê]ôô(ôô(ô(spurameter[ô[êô-3êô]ê] +
        spurameter[ô[êô-2êô]ê]*Exp[ô-\ spurameter[ô[êô-1êô]ê]ê*T*
òFractionBox[ô300ê, ô348ê]])ê*\
òSuperscriptBox[ô10ê, ô-6ê] (*fit\ function*) )ê/ô(1.602176565*
òSuperscriptBox[ô10ê, ô-19ê] (*e*) )êê/ô(
òFractionBox[ôô1êô\ ê
òSuperscriptBox[ô10ê, ô-2ê]ô (*dim1*) êê, ôô1êô (*scale1*) êô3.520êô\ ê
òSuperscriptBox[ô10ê, ô-10ê]ô (*a*) êê]
òFractionBox[ôô1êô\ ê
```

```
òSuperscriptBox[ô10ê, ô-2ê]ô (*dim2*) êê, ô
òFractionBox[ô1ê,
SqrtBox[ô2ê]]ô (*scale2*) êô3.520êô\ ê
òSuperscriptBox[ô10ê, ô-10ê]ô (*a*) êê])ê)ê âTêê
```

Develop an increment of sputtering

This symbol will later be called to damage the sample. It takes as input the size of the simulated crystal, the times of the increment, the line in our sputtering log corresponding to the sputtering parameters used, and the sputtering yield (assumed 1). It outputs a square array of dimension 'size', the elements of which are

```
theNeedle[size_, t0_, t1_, spurameter_, q_] := Block[{newcrystal, ncollisions},
  newcrystal = ConstantArray[0, {size, size}];
  ncollisions = (size - 1)*(size - 2)*iExpPerS[t0, t1, spurameter];
  For[(*1*)
   aa = 0,(*define iterator*)

   aa < ncollisions,(*limit iterator, one iteration per shot*)

   aa++,(*increment*)
   shoot = {};
   shoot1 =
    Append[shoot,
     RandomInteger[{2, size - 1}, 2]](*primary collision index*);
   shoot2 =
    RandomSample[{Sqrt[2], Sqrt[2], 1,
      1(*weights*)} ->(*choices*)
        {{shoot1[[1, 1]] - 1,
      shoot1[[1, 2]]}(*up*), {shoot1[[1, 1]] + 1,
      shoot1[[1, 2]]}(*down*), {shoot1[[1, 1]],
      shoot1[[1, 2]] - 1}(*left*), {shoot1[[1, 1]],
      shoot1[[1, 2]] + 1}(*right*)},
                RandomChoice[{q - 1, q,
     q + 1}](*this many neighboring locations*)](*close RandomSample[]*);
   shoot3 = shoot1~Join~shoot2;
         For[(*2*)
         bb = 1,(*define iterator*)

   bb < Length[shoot3] + 1,(*limit iterator*)

   bb++,(*increment*)

   newcrystal[[shoot3[[bb, 1]], shoot3[[bb, 2]]]] =
    newcrystal[[shoot3[[bb, 1]], shoot3[[bb, 2]]]] +
     1(*set each index in shoot to 1 in the crystal map*)](*close For[2]*);
  Clear[shoot, shoot1, shoot2, shoot3, bb]];(*close For[1]*)
 Clear[aa];
 newcrystal](*close Block[]*);
```

```
Develop the analysis
ACDC[size_, time_, dt_, spurameter_, q_, maxR_] :=
 Block[{resultCorral, theTimeList},
  resultCorral = {makeTheDough[[2 ;;, 2]]};
  theTimeList = Table[i dt, {i, 0, 1 + IntegerPart[time/dt]}];
  (*this loop iterates over the sputtering increments,
  throws a list of multiplicities out for virgin sites sitting at the center \
of each distance in the nearest neighbors list*)

  For[(*1*)
       cc = 1; theLightCrystal = ConstantArray[0, {size, size}],
       cc < Length[theTimeList],
       cc++,
       theLightCrystal =
    theLightCrystal +
     theNeedle[size, theTimeList[[cc]], theTimeList[[cc + 1]], spurameter, q];
       theDarkCrystal = ArrayPad[theLightCrystal, 1, 1];
       Clear[virginFinder];
       virginFinder = Block[{Heskett, Nightingale, McCorkle},
     Heskett = theDarkCrystal[[maxR ;; -maxR, maxR ;; -maxR]];
     Nightingale = Position[Heskett, 0];
     McCorkle =
      Table[{maxR - 1, maxR - 1} + Nightingale[[m]], {m,
        Length[Nightingale]}]];
   (*this loop iterates over virgin sites found on the crystal after each \
sputtering increment*)
       For[(*2*)
            dd = 1,
            dd < Length[virginFinder] + 1,
            dd++,
            dot = virginFinder[[dd]];
    (*this loop iterates over the possible distances in the nearest neighbor \
list, breaking out when it finds a sputtered atom and returning the previous \
distance as the island radius*)
            For[(*3*)
                 ee = 2,
                 ee < 310(*Length[
     makeTheDough]+1*)(*my sims show running further than row 310 (~
     20 atom radius) is unnecessary*),
                 ee++,
                 Clear[ring];
                 ring = Total[

      Extract[(*get the pixel values from the image that correspond to the \
NN sets*)
                 theDarkCrystal,
```

```
      Map[(*reassign the NN info to refer specifically to the dot inputted*)
\
                        dot + # &,
                        makeTheDough[[ee, 4]]
                        ](*close Map[]*)
                        ](*close Extract[]*)
                        \
](*close Total[]*);
                        If[ring > 0, Break[]](*kick out of the search loop when a non-
    zero element is found*);
                        ](*close For[3]*);
                AppendTo[
                        virginFinder[[dd]],
                        makeTheDough[[ee - 1, 2]]
                        ](*close AppendTo[]*);
                ](*close For[2]*);
  neckTies = AppendTo[resultCorral,
    {Length[virginFinder]}
    ~Join~
    Table[
        Count[virginFinder[[All, 3]], j]
     , {j, makeTheDough[[3 ;;, 2]]}
        ](*close Table[]*)
        ](*close AppendTo[]*);
  ](*close For[1]*);
 contracts = neckTies;
 contracts[[2 ;;, 2 ;;]] =
  Table[
   Total[neckTies[[i, j ;;]]], {i, 2, Length[neckTies]}, {j, 2,
    Length[neckTies[[1]]]}];
 contracts = Insert[contracts, Table[1, {k, Length[contracts[[1]]]}], 2];
 PrependTo[contracts[[1]], {"t", "mL"}];
 PrependTo[contracts[[2]], {0, 0}];
 For[
  ff = 3,
  ff < Length[contracts] + 1,
  ff++,
  PrependTo[
   contracts[[ff]], {dt (ff - 2),
    q iExpPerS[0, dt (ff - 2), spurameter]}]];
 highVoltage = contracts;
 highVoltage[[3 ;;, 2 ;;]] =
  Table[
   contracts[[k, l]]/(size - (2 maxR))^2(*(contracts[[1,l]]))^2 contracts[[
    k,2]]*)// N, {k, 3, Length[contracts]}, {l, 2,
```

```
    Length[contracts[[1]]]}];
  ](*close Block[]*);
```
Wheelhouse
Execute everything up to this point. Then use this to generate the data for analysis
```
ACDC[200(*size*), 120(*total sputter time*), 12(*dt (individual sputter \
length)*),
 ArParms[[51]](*sputtering parameters*), 1(*q*), 6(*max search radius*)]
results200$120$12$ArParms51$1$6 = highVoltage;
Clear[theLightCrystal, theDarkCrystal, virginFinder, cc, dd, ee, ring, \
contracts, neckTies, highVoltage]
ACDC[200(*size*), 1200(*total sputter time*), 180(*dt (individual sputter \
length)*),
 ArParms[[51]](*sputtering parameters*), 1(*q*), 6(*max search radius*)]
results200$1200$180$ArParms51$1$6 = highVoltage;
ACDC[200(*size*), 1200(*total sputter time*), 180(*dt (individual sputter \
length)*),
 ArParms[[51]](*sputtering parameters*), 1(*q*), 6(*max search radius*)]
results200$1200$180$ArParms51$1$6 = highVoltage;
ACDC[1000(*size*), 900(*total sputter time*), 90(*dt (individual sputter \
length)*),
 ArParms[[51]](*sputtering parameters*), 1(*q*), 20(*max search radius*)]
results1000$900$90$ArParms51$1$20 = highVoltage;
ACDC[200(*size*), 900(*total sputter time*), 150(*dt (individual sputter \
length)*),
 ArParms[[51]](*sputtering parameters*), 1(*q*), 20(*max search radius*)]
```
Recordkeeping for results
With everything else constant, simulation time goes like
number of sputter increments affects sim time by direct proportion (
Tsim[Subscript[dt, 2] = 2 Subscript[dt, 1]] = 1/2 Tsim[Subscript[dt, 1]])
theta appears to have no observable effect so far
sim time seems to go proportionally to the product of time increments and crystal size
(Tsim[Subscript[size, 2] = 2 Subscript[size, 1], t/dt] =
 t/dt Subscript[size, 2]^2/Subscript[size, 1]^2 Tsim[Subscript[size, 1]]
(expand the next lines via the arrows at right when opened in Mathematica, they're suppressed for the dissertation appendix format to keep the length manageable)
1 by 6 Argon 500 cal
1 by 6 Neon 500 cal
2 by 7 Argon 500 cal
Display
Tick Marks
This generates the tick marks for axes in the plots. You can tweak it if you know what you're doing. Otherwise, leave it off!
```
makeTicks[output_] := Block[{},
  TicksML = Table[{n - 1, output[[n, 1, 2]]}, {n, 2, Length[output], 2}];(*
  generates the monolayer Xaxis *)
```

```
 TicksTime =
  Table[{n - 1, output[[n, 1, 1]]/60}, {n, 2, Length[output], 2}];(*
 generates the sputter time Xaxis *)
 TicksY = Table[.2 i, {i, 0, 5}];(*
 generates the Yaxis *)

 TicksR =
  Table[{n - 1, output[[1, n]]}, {n, 2, Length[output[[1]]],
    3}];(*generates R axis (for 3D ListPlot*)]
3D surface plot - dimensions {sputter time, radius,
ëôòSubsuperscriptBox[ôfê, ôqê, ôNê]ê}

d3Plot[output_] := ListPlot3D[
 Flatten[Table[
                  {m - 1, output[[1, n]], output[[m, n]]},
                  {n, 2, Length[output[[1]]]},
                  {m, 2, Length[output]}
                  ], 1],
 PlotRange -> {0, 1},
 AxesLabel -> {"sputtering (min)", "radius",
   "ëôòSubsuperscriptBox[ôfê, ôqê, ôNê]ê"},
 Ticks -> {TicksTime, TicksR, TicksY},
 ColorFunction -> "BrownCyanTones"
         ]
2D plot - dimensions {sputter time, f}, one trace per radius
d2PlotPrimary[output_, rmin_, rmax_] := ListPlot[
 Table[
  Tooltip[
   Partition[
    Riffle[
     Transpose[output[[2 ;; -2]]][[1, All, 2]](*x axis*),
     Transpose[output[[2 ;; -2]]][[
      i]](*y axis*)
     ](*close Riffle[]*)
    ,
    2](*close Partition*)
   ,
   output[[1, i + 1]]](*Close Tooltip]*)
  , {i,
   Position[output[[1]]^2, rmin^2][[1, 1]] - 1,
   Position[output[[1]]^2, rmax^2][[1, 1]] - 1}](*close Table*),
 (*above this comment is function, below it is form*)
 Joined -> True,
 Frame -> True,
 PlotMarkers -> {"x"},
 PlotStyle -> Thick,
```

```
  PlotStyle -> Directive[Opacity[.2]],
  PlotRange -> All,
  FrameLabel -> {"Sputtering (ML equivalent removed)", "Intensity",
    "Summary - argon"},
  FrameStyle -> Directive[Larger],
  Epilog -> {
    Inset[
     Panel[
      Grid[
       MapIndexed[
        {Graphics[
          {ColorData[1, First@#2], Thick, Line[{{0, 0}, {1, 0}}]},
          AspectRatio -> .1, ImageSize -> 20](*Close Graphics[]*), #1}
        &, Table[Round[Sqrt[2] p output[[1, i]]^2, 0.01] // N,
        {i, Position[output[[1]]^2, rmin^2][[1, 1]] - 1,
         Position[output[[1]]^2, rmax^2][[1, 1]] -
          1}](*Close Table[]*)
       ](*close MapIndexed[]*)
      \
](*Close Grid[]*)
     ](*Close Panel[]*),
    Offset[{-2, -55}, Scaled[{1, 1}]],
    {Right, Top}](*Close Inset[]*),
   Inset[
    Panel[
     Text["Monte Carlo\ntrace   cells"]
     ](*Close Panel[]*),
    Offset[{-2, -2}, Scaled[{1, 1}]],
    {Right, Top}](*Close Inset[]*),
   Inset[
    Panel[
     Grid[
      {{Graphics[{RGBColor[0, 0.501961(*0.3*), 0], Thick, Dashed,
         Line[{{0, 0}, {1, 0}}]}, AspectRatio -> .1, ImageSize -> 20],
        Text["Å   LEED"]}}]],
    Offset[{-100, -2}, Scaled[{1, 1}]], {Right, Top}](*,
   Inset[
   Panel[
   Grid[
   {{Graphics[{Red,Thick,Dashed,Line[{{0,0},{1,0}}]},AspectRatio®.1,
   ImageSize®20],Text["Ä    IPES"]}}]],Offset[{-100,-40},Scaled[{1,
   1}]],{Right,Top}]*)
   }](*Close ListPlot[]*)
d2PlotSecondary[output_, rmin_, rmax_] := ListPlot[
  Table[
   Tooltip[
```

```
   Partition[
    Riffle[
     Transpose[output[[2 ;; -2]]][[1, All, 2]](*x axis*),
     Transpose[output[[2 ;; -2]]][[
      i]](*y axis*)
     ](*close Riffle[]*)
    ,
    2](*close Partition*)
   ,
   output[[1, i + 1]]](*Close Tooltip]*)
  , {i,
   Position[output[[1]]^2, rmin^2][[1, 1]] - 1,
   Position[output[[1]]^2, rmax^2][[1, 1]] - 1}](*close Table*),
 Joined -> True,
 Frame -> True,
 FrameStyle -> Directive[Larger],
 PlotStyle -> Dashed,
 PlotRange -> All,
 FrameLabel -> {"Sputtering (ML equivalent)", "Intensity",
   "Monte Carlo Simulation"},
 ImageSize -> {1000, 650}
 ]
```

The Final Countdown

These lines just display the results of the simulation. Output is suppressed for this format and included, where appropriate, in the body of the dissertation.

```
finishHim[output_] :=
 For[z = 0, z < 1, z++, makeTicks[output]; Print[d3Plot[output]];
  Print[d2PlotPrimary[output];];]
finishHim[results200$120$12$ArParms51$1$6]
oldone = d2PlotPrimary[results200$120$12$ArParms51$1$6, 1, 6]
```

BIBLIOGRAPHY

T. Allmers, M. Donath, J. Braun, J. Minar and H. Ebert, "d- and sp- like surface states on fcc Co(001) with distinct sensitivity to surface roughness," *Physical Review B*, vol. 84, p. 245426, 2011.

N. Ashcroft and N. Mermin, *Solid State Physics*, Philadelphia: W.B. Saunders College, 1976.

J. Bellina and H. Farnsworth, "Ion Bombardment Induced Surface Damage in Tungsten and Molybdenum Single Crystals," *Journal of Vacuum Science and Technology*, vol. 9, no. 2, pp. 616-619, 1972.

A. Bendounan, H. Cercellier, Y. Fagot-Revurat, B. Kierren, V. Yurov and D. Malterre, "Confinement of Shockley states in ultrathin films of Ag on Cu(111)," *Thin Solid Films*, vol. 428, no. 1-2, pp. 119-122, 2003.

R. Benedek and M. M. Thackeray, "Lithium Reactions with Intermetallic-Compound Electrodes," *Journal of Power Sources*, vol. 110, pp. 406-411, 2002.

A. Biermanns, A. Hanisch, J. Grenzer, T. Metzger and U. Pietsch, "Tuning the shape and damage in ion-beam induced ripples on silicon," *Physica Status Solidi (a)*, vol. 208, no. 11, pp. 2608-2611, 2011.

N. Biswas, J. Gurganus and V. Misra, "Work function tuning of nickel silicide by co-sputtering nickel and silicon," *Applied Physics Letters*, vol. 87, p. 171908, 2005.

E. Boschung, T. Pillo, J. Hayoz, L. Patthey, P. Aebi and L. Schlapbach, "Hydrogen-induced changes in the surface states/resonances of Ni(100)," *Journal of Electron Spectroscopy and Related Phenomena*, Vols. 101-103, pp. 349-353, 1999.

M. Budke, V. Renken, H. Liebl, G. Rangelov and M. Donath, "Inverse photoemission with energy resolution better than 200 meV," *Review of Scientific Instruments*, vol. 78, p. 083903, 2007.

C. L. Campion, W. Li and B. L. Lucht, "Thermal Decomposition of $LiPF_6$- Based Electrolytes for Lithium-Ion Batteries," *Journal of the Electrochemical Society*, vol. 152, no. 12, pp. A2327-A2334, 2005.

C. Chan, H. Peng, G. Liu, K. Mcilwrath, X. Zhang, R. Huggins and Y. Cui, "High-performance lithium battery anodes using silicon nanowires," *Nature Nanotechnology*, vol. 3, no. 1, pp. 31-35, 2008.

W. Chan and E. Chason, "Making waves: Kinetic processes controlling surface evolution during low energy ion sputtering," *AIP Journal of Applied Physics*, vol. 101, p. 121301, 2007.

N. S. Choi, K. H. Yew, K. Y. Lee, M. Sung, H. Kim and S. S. Kim, "Effect of Fluoroethylene Carbonate Additive on Interfacial Properties of Silicon Thin-Film Electrode," *Journal of Power Sources*, vol. 161, pp. 1254-1259, 2006.

M. J. Chon, V. A. Sethuraman, A. McCormick, V. Srinivasan and P. R. Guduru, "Real-Time Measurement of Stress and Damage Evolution During Initial Lithiation of Crystalline Silicon," *Physical Review Letters*, vol. 107, p. 045503, 2011.

S. Dalavi, P. Guduru and B. L. Lucht, "Performance Enhancing Electrolyte Additives for Lithium Ion Batteries with Silicon Anodes," *Journal of the Electrochemical Society*, vol. 159, pp. A642-A646, 2012.

N. Ding, J. Xu, Y. Yao, G. Wegner, I. Lieberwirth and C. Chen, "Improvement of cyclability of Si as anode for Li-ion batteries," *Journal of Power Sources,* vol. 192, no. 2, pp. 644-651, 2009.

K. Edström, M. Herstedt and D. P. Abraham, "A new look at the solid electrolyte interphase on graphite anodes in Li-ion batteries," *Journal of Power Sources*, vol. 153, no. 2, pp. 380-384, 2006.

R. Elazari, G. Salitra, G. Gershinsky, A. Garsuch, A. Panchenko and D. Aurbach, "Li Ion Cells Comprising Lithiated Columnar Silicon Film Anodes, TiS_2 Cathodes and Fluoroethyene Carbonate (FEC) as a Critically Important Component," *Journal of the Electrochemical Society*, vol. 159, pp. A1440-A1445, 2012.

P. Erdman and E. Zipf, "Low Voltage, High Current Electron Gun," *Review of Scientific Instruments*, vol. 53, pp. 225-227, 1982.

V. Etacheri, O. Haik, Y. Goffer, G. A. Roberts, I. C. Stefan, R. Fasching and D. Aurbach, "Effect of Fluoroethylene Carbonate (FEC) on the Performance and Surface Chemistry of Si-Nanowire Li-Ion Battery Anodes," *Langmuir*, vol. 2011, pp. 965-976, 2011.

P. Gartland and B. Slagsvold, "Transitions conserving parallel momentum in photoemission from the (111) face of copper," *Physical Review B*, vol. 21, p. 4047, 1975.

A. Goldmann, V. Dose and G. Borstel, "Empty electronic states at the (100), (110), and (111) surfaces of nickel, copper, and silver," *Physical Review B*, vol. 32, no. 4, pp. 1971-1980, 1985.

A. Goldmann, M. Donath, W. Altmann and V. Dose, "Momentum-resolved inverse photoemission study of nickel surfaces," *Physical Review B*, vol. 32, no. 2, pp. 837-850, 1985.

M. Gorgoi, S. Svensson, F. Schafers, W. Braun, and W. Eberhardt, "Hard X-ray high kinetic energy photoelectron spectroscopy at the KMC-1 beamline at BESSY," *European Physical Journal-Special Topics*, vol. 169, pp. 221-225, 2009.

D. Heskett, D. DePietro, G. Sabatino and M. Tammaro, "Ion bombardment-induced changes in the electronic structure of Cu(110) investigated with inverse photoemission and computer simulations," *Surface Science*, vol. 513, pp. 405-411, 2002.

S. H. Kang, D. P. Abraham, A. Xiao and B. L. Lucht, "Investigating the Solid Electrolyte Interphase Using Binder-Free Graphite Electrodes," *Journal of Power Sources*, vol. 175, pp. 526-532, 2008.

P. Lane, G. Isted and R. Cole, "Effect of surface defects and adsorbates on the optical anisotropy of Cu(110)," *Physical Review B*, vol. 82, p. 075416, 2010.

B. Lestriez, S. Bahri, I. Sandu, L. Roue and D. Guyomard, "On the binding mechanism of CMC in Si negative electrodes for Li-ion batteries," *Electrochemistry Communications,* vol. 9, pp. 2801-2806, 2007.

J. Li, W. Schneider, R. Berndt, O. Bryant and S. Crampin, "Surface-State Lifetime Measured by Scanning Tunneling Microscopy," *Physical Review Letters*, vol. 81, no. 20, pp. 4464-4467, 1998.

S. Y. Li, X. L. Xu, X. M. Shi, B. C. Li, Y. Y. Zhao, H. M. Zhang, Y. L. Li, W. Zhao, X. L. Cui and L. P. Mao, "Composition Analysis of the Solid Electrolyte Interphase Film on Carbon Electrode of Lithium-Ion Battery Based on Lithium Difluoro (Oxalate) Borate and Sulfolane," *Journal of Power Sources*, vol. 217, pp. 503-508, 2012.

A. Magasinski, B. Zdyrko, I. Kovalenko, B. Hertzberg, R. Burtovyy, C. Huebner, T. Fuller, I. Luzinov and G. Yushin, "Toward Efficient Binders for Li-Ion Battery Si-Based Anodes: Polyacrylic Acid," *ACS Applied Materials and Interfaces,* vol. 2, no. 11, pp. 3004-3010, 2010.

S. Malmgren, K. Ciosek, M. Hahlin, T. Gustafsson, M. Gorgoi, H. Rensmo and K. Edström, "Comparing anode and cathode electrode/electrolyte interface composition and morphology using soft and hard x-ray photoelectron spectroscopy," *Electrochimica Acta,* vol. 97, pp. 23-32, 2013.

T. Michely and G. Comsa, "Temperature dependence of the sputtering morphology of Pt(111)," *Surface Science*, vol. 256, no. 3, pp. 217-226, 1991.

T. Michely and G. Comsa, "The scanning tunneling microscope as a means for the investigation of ion bombardment effects on metal surfaces," *Nuclear Instruments and Methods in Physics Research Section B: Beam Interactions with Materials and Atoms*, vol. 82, no. 2, pp. 207-219, 1993.

K. Morgenstern, K. Braun and K. Rieder, "Surface-State Depopulation on Small Ag(111) Terraces," *Physical Review Letters*, vol. 89, no. 22, p. 226801, 2002.

H. Nakai, T. Kubota, A. Kita and A. Kawashima, "Investigation of the Solid Electrolyte Interphase Formed by Fluoroethylene Carbonate on Si Electrodes," *Journal of the Electrochemical Society*, vol. 158, pp. A798-A801, 2011.

M. Nie, D. P. Abraham, Y. Chen, A. Bose and B. L. Lucht, "Silicon Solid Electrolyte Interphase (SEI) of Lithium Ion Battery Characterized by Microscopy and Spectroscopy," *Journal of Physical Chemistry C*, vol. 117, pp. 13403-13412, 2013.

M. N. Obrovac and I. Christensen, "Structural Changes in Silicon Anodes During Lithium Insertion/Extraction," *Electrochemical Solid State Letters*, vol. 7, pp. A93-A96, 2004.

X. Ou, R. Kögler, X. Wei, A. Mücklich, X. Wang, W. Skorupa and S. Facsko, "Fabrication of horizontal silicon nanowire arrays on insulator by ion irradiation," *AIP Advances*, vol. 1, p. 042174, 2011.

L. R. Painter, E. T. Arakawa, M. W. Williams and J. C. Ashley, "Optical Properties of Polyethylene: Measurement and Applications," *Radiation Reseach*, vol. 83, no. 1, pp. 1-18, 1980.

B. Philippe, R. Dedryvère, M. Gorgoi, H. Rensmo, D. Gonbeau and K. Edström, "Role of the $LiPF_6$ Salt for the Long-Term Stability of Silicon Electrodes in Li-Ion Batteries − a Photoelectron Spectroscopy Study," *Chemistry of Materials*, vol. 25, pp. 394-404, 2013.

B. Philippe, R. Dedryvère, J. Allouche, F. Lindgren, M. Gorgoi, H. Rensmo, D. Gonbeau and K. Edström, "Nanosilicon Electrodes for Lithium-Ion Batteries: Interfacial Mechanisms Studied by Hard and Soft X-Ray Photoelectron Spectroscopy," *Chemistry of Materials*, vol. 24, pp. 1107-1115, 2012.

S. Pons, P. Mallet, L. Magaud and J. Veuillen, "Investigation of the Ni(111) Shockley-like surface state using confinement to artificial nanostructures," *Europhysics Letters*, vol. 61, no. 3, pp. 375-381, 2003.

Y. R. Ren, J. N. Ding, N. Y. Yuan, S. Y. Jia, M. Z. Qu and Z. L. Yu, "Preparation and Characterization of Silicon Monoxide/Graphite/Carbon Nanotubes Composite

as Anode for Lithium-Ion Batteries," *Journal of Solid State Electrochemistry*, vol. 16, pp. 1453-1460, 2012.

O. Rodríguez de la Fuente, M. González-Barrio, V. Navarro, B. Pabón, I. Palacio and A. Mascareque, "Surface defects and their influence on surface properties," *Journal of Physics: Condensed Matter,* vol. 25, no. 48, p. 484008, 2013.

R. Roucka, J. Jiruse and T. Sikola, "Spot intensity processing in LEED images," *Vacuum*, vol. 65, pp. 121-126, 2002.

C. Ruggiero, M. Badal, T. Choi, D. Gohlke, D. Stroud and J. Gupta, "Emergence of surface states in nanoscale Cu_2N islands," *Physical Review B*, vol. 83, p. 245430, 2011.

J. H. Scofield, "Theoretical Photoionization Cross Sections From 1 to 1500 keV," Lawrence Livermore Laboratory, Livermore, 1973.

H. C. Shin and M. Liu, "Copper Foam Structures with Highly Porous Nanostructured Walls," *Chemistry of Materials*, vol. 16, pp. 5460-5464, 2004.

D. A. Shirley, "High Resolution X-Ray Photoemission Spectrum of the Valence Bands of Gold," *Physical Review B*, vol. 5, pp. 4709-4714, 1972.

C. Su, D. Tang and D. Heskett, "Two-dimensional unoccupied electronic band structure of clean Cu(110) and (1x2) Na/Cu(110)," *Surface Science*, vol. 310, pp. 45-51, 1994.

D. Tang and D. Heskett, "Unoccupied electronic structure of Na/Ni(111)," *Physical Review B*, vol. 47, no. 16, pp. 695-699, 1993.

S. Tanuma, C.J. Powell, and D.R. Penn, “Calculations of electron inelastic mean free paths. IX. Data for 41 elemental solids over the 50 eV to 30 keV range,” *Surface and Interface Analysis*, vol. 43, pp. 689-713, 2011.

M. Vasylyev, A. Blaschuk, N. Mashovets and N. Vilkova, "LEED study of Ni(100) and (111) surface damage caused by Ar+ ion bombardment with low energy and small doses," *Vacuum*, vol. 57, pp. 71-80, 2000.

Q. Wei, K. Li, J. Lian and L. Wang, "Angular dependence of sputtering yield of amorphous and polycrystalline materials," *Journal of Physics D: Applied Physics*, vol. 41, p. 172002, 2008.

C. Weiland, R. Browning, B. A. Karlin, D. A. Fischer and J. C. Woicik, "Note: Alignment/focus dependent core-line sensitivity for quantitative chemical analysis in hard x-ray photoelectron spectroscopy using a hemispherical electron analyzer," *Review of Scientific Instruments*, vol. 84, p. 036106, 2013.

C. Weiland, A. K. Rumaiz, P. Lysaght, B. Karlin, J. C. Woicik and D. Fischer, "NIST high throughput variable kinetic energy hard X-ray photoelectron spectroscopy facility," *Journal of Electron Spectroscopy and Related Phenomena*, vol. 190, pp. 193-200, 2013.

H. Wu and Y. Cui, "Designing Nanostructured Si Anodes for High Energy Lithium Ion Batteries," *Nano Today*, vol. 7, pp. 414-429, 2012.

A. Xiao, L. Yang, B. L. Lucht, S. H. Kang and D. P. Abraham, "Examining the Solid Electrolyte Interphase on Binder-Free Graphite Electrodes," *Journal of the Electrochemical Society*, vol. 156, pp. A318-A327, 2009.

K. Xu, "Nonaqueous Liquid Electrolytes for Lithium-Based Rechargeable Batteries," *Chemical Reviews*, vol. 104, pp. 4303-4318, 2004.

J. Yang, M. Winter and J. Besenhard, "Small particle size multiphase Li-alloy anodes for lithium-ion batteries," *Solid State Ionics*, vol. 90, pp. 281-287, 1996.

B. Young, D. Heskett, M. Nie, C. Nguyen, B. Lucht and J. Woicik, "Hard X-Ray Photoelectron Spectroscopy (HAXPES) Investigation of the Silicon Solid Electrolyte Interphase (SEI) in Lithium-Ion Batteries," to be published.

S. Yu, B. Bahrim, B. Makarenko and J. Rabalais, "Local effect of Na adsorption on Cu(111)," *Surface Science*, vol. 606, pp. 1700-1704, 2012.

O. Zeybek, A. Davarpanah and S. Barrett, "Electronic surface states of Cu(110) surface," *Surface Science*, vol. 600, pp. 5176-5181, 2006.

W. Zhang, "A review of the electrochemical performance of alloy anodes for lithium ion batteries," *Journal of Power Sources*, vol. 196, pp. 13-24, 2011